Computational study of inductively coupled plasma mass spectroscopy (ICP-MS)

Proefschrift voorgelegd tot het behalen van
de graad van doctor in de Wetenschappen aan
de Universiteit Antwerpen te verdedigen door

Maryam Aghaei

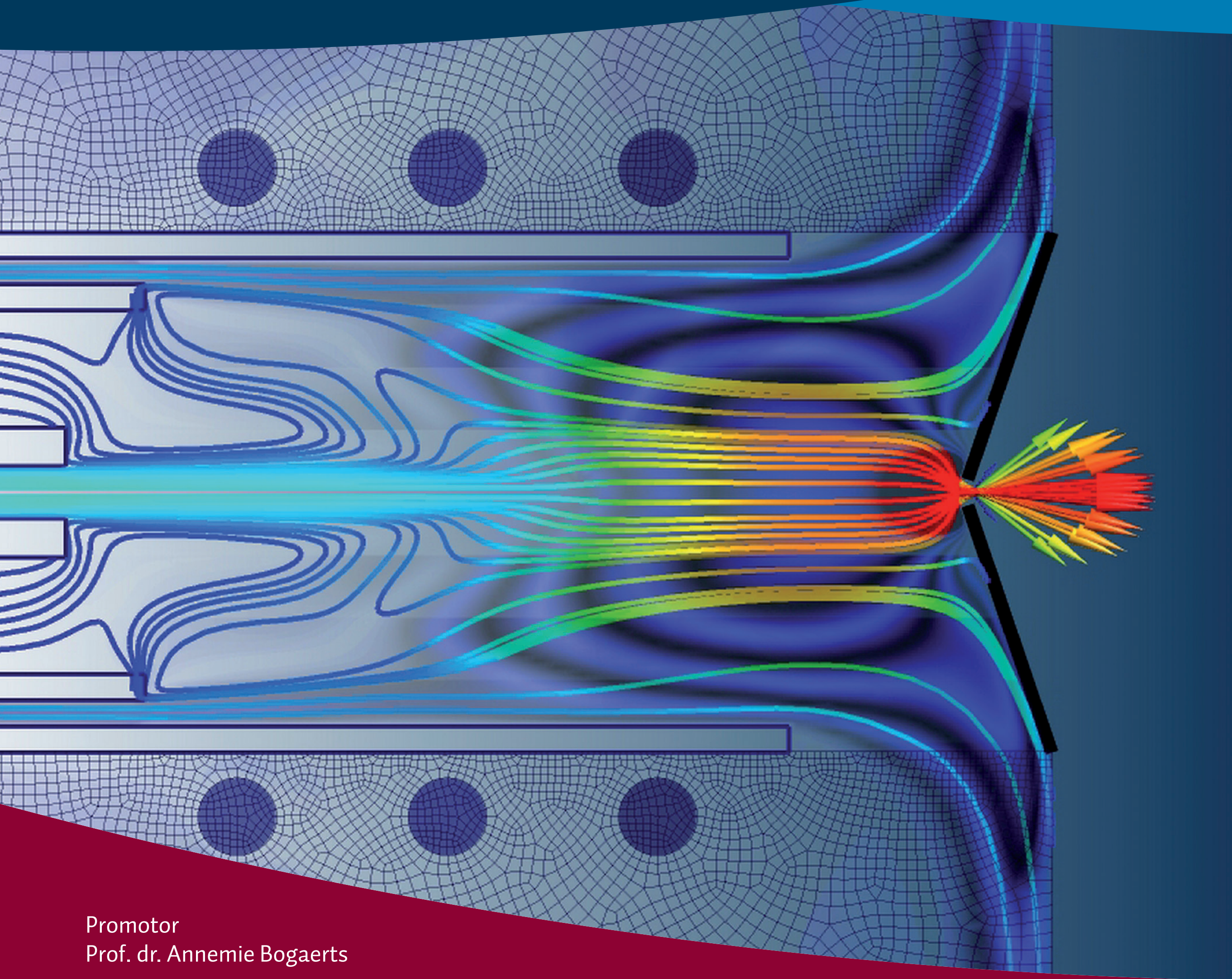

Promotor
Prof. dr. Annemie Bogaerts

Faculteit Wetenschappen
Departement Fysica - Chemie
Antwerpen 2014

Universiteit
Antwerpen

Faculteit Wetenschappen

Departement Fysica

Computational study of inductively coupled plasma mass spectroscopy (ICP-MS)

Proefschrift voorgelegd tot het behalen van de graad van Doctor in de Wetenschappen aan de Universiteit Antwerpen te verdedigen door

Maryam Aghaei

Promotor: Prof. Dr. Annemie Bogaerts

Department Chemie, Antwerpen, 2014

Members of Doctoral Jury:

- Prof. Dr. José Broekaert
- Prof. Dr. Vittorio Colombo
- Prof. Dr. Detlef Günther
- Prof. Koen Janssens
- Prof. Bart Partoens
- Prof. Dirk Lamoen

Cover design: Anita Muys, Photo: Maryam Aghaei

Faculty of Science, Department of Chemistry and Physics, Universiteit Antwerpen, Antwerpen, 2014

ISBN 9789057284472
D/2014/12.293/9

https://www.uantwerp.be/en/rg/plasmant

Contents

Acknowledgment

I revel in writing this section because it fills my mind with goodwill, kindness, and lovely moments.

I had just arrived from the airport and had an interview appointment near the campus. It was the first time I was meeting professor Annemie Bogaerts: a cheerful strong-minded woman with incredible energy. Just meeting her, two points were clarified for me that day: that I'll have to be strong and disciplined, and that I can trust in her commitment and support. I decided to learn from her, and now after years, more items have been added to the list: to be efficient and fast at the same time; to have a full schedule, yet smile and be patient; to be a decisive manager while being a compassionate adviser. These are the qualities I acknowledge and regard my success indebted to them. In addition, I'm grateful to her for giving me the opportunity to participate in many conferences, various scholar visits, and for helping me in building my professional network. Dear Annemie, thank you! It was a bliss to be your student.

Dr. Helmut Lindner has been a real teacher, colleague, and friend to me; a person who has always impressed me by his vast knowledge and, at the same time, humbleness. Working with him was so delightful, and the scientific dialogues I had with him have always been helpful for me. Undoubtedly, because of the great ICP model he has developed which was used as a basis for my research, his contribution to the success of this work is indisputable. I'm grateful for all the moments he spent on teaching me. I also thank him for recommending me to visit Prof. Niemax' Lab at the very beginning of my work. This made me have a better understanding of ICP since it was my first introduction to the experimental part of my research topic. Moreover, it's an honor for me to be friend with such a respectable person. Vielen Dank Dr. Lindner!

I have learned from an outstanding physicist, Prof. Kay Niemax, and would like to thank him for his support. Whenever I see him in Antwerp, Dortmund, or in a conference around the world, I totally feel his fatherly kindness. It is a pleasure for me to know him and have the chance to receive his advice. During my visit at his lab, I learned how a physicists group should work and I love the style of scientific discussions in his group. I thank Dr. Sebastian Groh for the time he spent to teach me how to work with the instrument, and appreciate the amicable time we spent together during my visit.

I also would like to thank Prof. Gary Hieftje for his hospitality in Bloomington, Indiana. He and his group members were so kind to me and it was a great opportunity to have discussion with them as experts. I got acquainted with different experimental setups there.

I had a wonderful time in Zürich at Prof. Detlef Günther's lab. His special character helped me to believe in myself. I like his style of managing a scientific group: very precise and very friendly. I thank him and his group's hospitality. Beside valuable scientific discussions, talking especially with Olga and Luca reminded me of my old friendships in Tehran.

During my study, I have received very important advices from Prof. Sam Houk whom I'd like to thank. It was a heart-warming moment to see the person who has made the first article in the field shows interest in my work. It was a great encouragement for me to work more and better. I am also grateful to Prof. Akbar Montaser for his guidance. It is my honor to meet him and have his counsels for my career and life. Akbar jaan, Sepaasgozaaram.

Here, I would like to thank Prof. Hassan Tavassoli, my master studies' supervisor who strengthened research motivation in me. His personality always stays an example for me.

Working in PLASMANT group gave me the chance to know and become friend with many nice people. I would like to thank them all for the wonderful time we had together. I am thankful to Luc not only for his technical support, but also for answering all my questions about Belgian culture. He is the source of most of my general information about the country. And, I should confess that he has detailed geographical information about the whole planet earth! (I have not checked further yet!)

I would like to thank Nelly and Ingrid for all their helps. Besides the academic administrative helps, I remember the days Nelly even translated the documents from Dutch to English for me. And an especial thank to her for "Fridays lively mood" she brought to me: when she was gathering her beautiful flowers and plants close to the sink to water them. Sometimes very small things could make a person smile.

Living abroad is a good experience but not an easy one. I am grateful to find dear friends here in Antwerp such as Helmut, Fabiana, Monika, Peter, Violeta, Justin, Mahsa, Steluta, Shuxia, David, Wouter, Hajar, Sonia, Reinier, Tomas, Samira, Jeff, Narjes, Mozhgan, Natalia, Antonin, Amin, Heshmat, Mujahid, Maryam, Nasrin, Andrei, Umed, Pieter-Jan, Maksud, Emillie, Mais, Anna and others who made my living experience in Antwerp such a great one! Friends from different parts of the world, who shared the happiness with me and I could learn from our differences.

There are some people whose presence gives a special meaning to someone's life. I would like to thank Saeid, Zeinab, Zahra, Somayeh, and Ghazaleh for giving me the chance of experiencing love. And, I am deeply grateful to Elham whose friendship always gives me the peace and happiness and helps me to improve my personality.

I especially thank Saeid for his love, support and respect. It is my dream to have, one day, a character like his. س. پ. عزیز، مرا تو بی سببی نیستی

Finally, I would like to express my deepest respect and utmost gratitude to my parents, who have always been there for me and have supported me my entire life. And many thanks to my lovely brother and sister talking to whom was the best thing during my stay abroad, in times when I needed to be home and I was far away.

مامان، بابا، رسول و مینای عزیزم، دوستتان دارم.

PART I: Introduction

Chapter 1:

General background

In this chapter, we will first give some general information about different plasma sources, and inductively coupled plasmas (ICPs) in particular. We will also discuss the different applications of ICPs. We will mainly focus on inductively coupled plasma mass spectrometry (ICP-MS) and its instrumentation and applications. Moreover, a review on fundamental studies on ICP (-MS) will be presented, and finally, we will explain the aim of this PhD thesis.

1.1. Plasma sources

Plasma typically refers to the fourth state of matter. It is a gas in which a certain portion of the species is ionized; hence it contains ions and electrons, besides neutral species (i.e., atoms and/or molecules and/or radicals). From a macroscopic point of view, plasma is electrically neutral. However, it contains free charge carriers and is electrically conductive. A plasma can be created by applying energy to a gas [1] in order to reorganize the electronic structure of the species (atoms, molecules) and to produce excited species and ions. This energy can be thermal, or carried by either an electric current or electromagnetic radiation. The inductively coupled plasma (ICP) described in this PhD work is generated from electrical energy. The electric field transmits energy to the electrons present in the gas/plasma (which are the most mobile charged species). This electric energy is then transmitted to the neutral species by collisions. These collisions [2] follow probabilistic laws and can be divided in:

- **Elastic collisions**: they do not change the internal energy of the species, but some kinetic energy will be exchanged.
- **Inelastic collisions**: when the energy is high enough, the collisions modify the electronic structure of the neutral species. This results in the creation of excited species or ions if the collisions are energetic enough.

Most of the excited species have a very short lifetime and they decay back to the ground state (or another, lower lying level) by photon emission. Some excited species are, however, metastable, i.e., they have a longer lifetime because their decay by emission of radiation is hampered as there are no allowed transitions departing from the respective state. So it means that decay can only take place by energy transfer through collisions [3].

Depending on the type of energy supply and the amount of energy transferred to the plasma, the properties of the plasma change, which is reflected among others in the electron density or temperature. These two parameters distinguish plasmas into different categories, presented in Figure 1.1. The ICP source studied in this PhD work is indicated by a red frame.

Based on the (presence or absence of) thermodynamic equilibrium between the various plasma species, a distinction can be made between equilibrium, local thermodynamic equilibrium (LTE) and non-local thermodynamic equilibrium (non-LTE) plasmas. In an equilibrium plasma, the gas species are nearly fully ionized with the same temperature and the plasma temperature is extremely high, as is the case in astrophysical plasmas (such as the sun) [4]. In an LTE plasma, only a small fraction of the gas molecules is ionized. The electrons and heavy particles approximately have the same temperature and show local electrical neutrality. The plasma temperature is still typically several thousand degrees, and therefore, this type of plasma is also called a thermal plasma. In a non-LTE plasma, on the other hand, the electron temperature is still typically several thousand degrees but the temperature of the heavy particles (i.e., neutral molecules, ions) is rather low. Hence, the gas itself is at ambient temperature, so we call this a cold plasma.

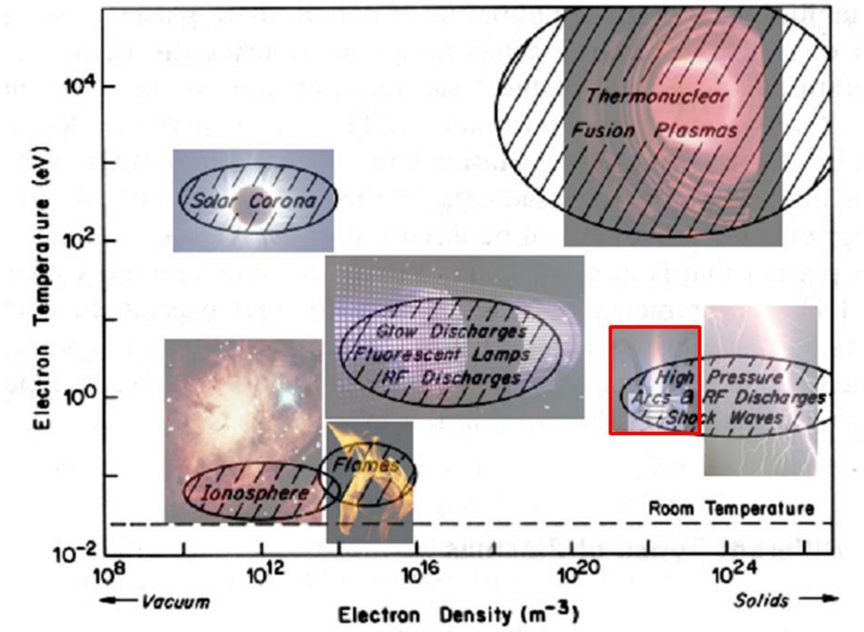

Figure 1.1: 2D classification of plasmas (electron temperature versus electron density) [6]. The ICP source under study in this PhD work is indicated by the red frame.

1.1.1. LTE plasmas

An LTE plasma requires that transitions and chemical reactions are governed by collisions and not by radiative processes. Moreover, collision phenomena have to be micro-reversible. This means that each kind of collision must be balanced by its inverse (i.e., excitation/deexcitation; ionization/recombination; kinetic balance) [5]. Moreover, LTE requires that local gradients of plasma properties (temperature, density, thermal conductivity) are low enough to let a particle in the plasma reach the equilibrium: the diffusion time must be similar or higher than the time the particle needs to reach the equilibrium [6]. For an LTE plasma, the heavy particle temperature is close to the electron temperature. According to the Griem criterion [7], an optically thin homogeneous plasma is in LTE if the electron density fulfills the following criterion:

$$n_e = 9 \cdot 10^{23} \left(\frac{E_{21}}{E_{H^+}} \right)^3 \left(\frac{k_B T}{E_{H^+}} \right) \qquad \left(m^{-3} \right)$$

E_{21} represents the energy gap between the ground state and the first excited level, E_{H^+} is the ionization energy of the hydrogen atom, T is the plasma temperature and k_B is the Boltzman constant. This criterion shows the strong link that exists between the required electron density for LTE and the energy of the first excited state. Those rules for LTE are very strict. Thus most of the plasmas deviate from LTE, especially all types of low density plasmas in the laboratory. LTE plasmas can be generated at atmospheric pressure or under soft vacuum conditions for a wide range of gases. Typical examples of thermal laboratory plasmas include various forms of direct current (DC) arcs and radio frequency (rf) induction plasmas. They are typically used for applications where heat is required, such as for cutting, spraying, welding or, as in the analytical ICP, for the evaporation of analyte material.

1.1.2. Non LTE plasmas

As mentioned above, deviation from LTE occurs when the temperature of the various species is not equal to each other, i.e., the electron temperature is much higher than the heavy particle temperature. Moreover, typically there is also departure from the Boltzmann distribution for the density of excited atoms. Indeed, for low-lying levels, the electron-induced deexcitation rate of the atom is generally lower than the corresponding electron induced excitation rate because of significant radiative decay [5]. Another deviation from LTE is induced by the mass difference between electrons and heavy particles. Electrons move very fast whereas heavy particles can be considered static: electrons are thus likely to dominate the collisions and transition phenomena. The high electron temperature gives rise to inelastic electron collisions, which, on the one hand, sustain the plasma (e.g. electron impact ionization) and on the other hand, result in a chemically-rich environment. Deviations from LTE are also due to strong gradients in the plasma and the associated diffusion effects. Non-LTE plasmas can be described by a two-temperature model, consisting of an electron temperature (T_e) and a heavy particle temperature (T_h). Due to the huge mass difference between electrons and heavy particles, the plasma temperature (or gas temperature) is determined by T_h. The higher the departure from LTE, the higher is the difference between T_e and T_h. Non-LTE plasmas are typically used for applications where heat is not desirable, such as for etching or the deposition of thin layers. Most of the applications result from the heavy particle kinetics (e.g. sputtering, deposition, ion implantation, chemical reactions,…).

Table 1.1 sums up the main characteristics of LTE and non LTE plasmas. Boulos et al. showed in [6] the influence of the pressure on the transition from a glow discharge to an arc discharge. They indicated that low pressure plasmas (0.1 to 10 Pa) are certainly non-LTE and the heavy particle temperature is clearly lower than the electron temperature. The inelastic collisions between electrons and heavy particles are mostly excitations and ionizations (and dissociations in the case of a molecular gas). These collisions do not rise the heavy particle temperature. When the pressure becomes higher, collisions become more important. They induce both plasma chemistry (by inelastic collisions) and heavy particle heating (by elastic collisions). The difference between T_e and T_h is reduced: the plasma becomes closer to LTE. Indeed a high power density induces LTE plasmas (e.g. arc plasmas) whereas non-LTE plasmas are favored by either a low power density or a pulsed power supply. In this latter case, the short pulse duration prevents the equilibrium state from establishing. Note, however, that atmospheric pressure plasmas can also be in non-LTE, like is the case for instance with dielectric barrier discharges. More details on LTE and deviations from LTE are given in the books by Huddlestone and Leonard [8], Griem [9], Lochte-Holtgreven [10] and Mitchner and Kruger [11].

Table: 1.1: Main characteristics of LTE and non-LTE plasmas [3]

	LTE plasmas	Non-LTE plasmas
Practical name	Thermal plasmas	Cold plasmas
Properties	$T_e = T_h$	$T_e >> T_h$
	High electron density $\sim 10^{21} - 10^{26}\ m^{-3}$	Lower electron density $< 10^{19}\ m^{-3}$
	Inelastic collisions between electrons and heavy particles create reactive species whereas elastic collisions heat the heavy particles (the electron energy is thus consumed)	Inelastic collisions between electrons and heavy particles induce the plasma chemistry. Heavy particles are slightly heated by a few elastic collisions (but the electron energy remains very high)
Examples	Arc plasmas (core) $T_e = T_h \approx 10{,}000\ K$	Glow discharges $T_e \approx 10{,}0000 - 100{,}000\ K$ $T_h \approx 300 - 1000\ K$

1.2. Inductively coupled plasmas (ICPs)

In an ICP, the rf currents in the coil (inductive element) generate an rf magnetic flux, which penetrates the plasma region. The time-varying magnetic flux density induces a solenoidal rf electric field, which accelerates the free electrons and sustains the discharge [12]. In general, inductively coupled plasmas (ICPs) are used for various kinds of applications. They can be used for coating deposition on surfaces, to sputter surfaces, for the production of fine powders, as lamps [13] or for elemental analysis. One major advantage that is valid for all ICPs is that they all are electrode-less plasmas. Thus, very pure plasmas are produced which is for instance very good for analytic purposes. Moreover, there is no abrasion of electrodes which would require a replacement of the electrode materials after some time of operation.

The ICPs used for the different applications are, however, operated under very different conditions, so it is clear that also very different kinds of plasmas are needed. Indeed, the major difference is the pressure at which they operate. In general, they are categorized in low pressure, intermediate pressure and atmospheric pressure ICP sources. For instance, ICPs for materials processing use pressures in the order of 0.1 to several Pascal (i.e., low-pressure ICPs) while ICPs for lamps work at several tens of Pascal (i.e., intermediate pressure ICPs), and ICPs for elemental analysis or for powder production work at atmospheric pressure. As a consequence, the first two types of ICPs are far from LTE while the latter type is near LTE. In the following we will describe in more detail the operating setup of the three types of ICPs. In most cases, a high frequency (HF) current is needed to sustain the plasma, typically ranging from several MHz to a few tens of MHz.

1.2.1. ICPs operating at low pressure

ICPs operating at low pressures (in the order of 0.1 to several Pascal) are typically used for materials processing. Basically, two different coil configurations can be distinguished in this type of ICPs, i.e. cylindrical and planar (see Figure 1.2.a and b) [14]. In the first configuration, a coil is placed around the discharge chamber, as a helix. In the second configuration, which is more commonly used for materials processing, a flat helix or spiral is positioned above the discharge chamber, separated from the discharge region by a dielectric material. Advantages of the latter configuration are reduced plasma losses and better ion generation efficiency; a disadvantage is the higher sputter-contamination, UV-damage and heating of neutrals at the substrate. The planar coil can also be moved close to the wafer surface, resulting in a near-planar source geometry, having good uniformity properties [15].

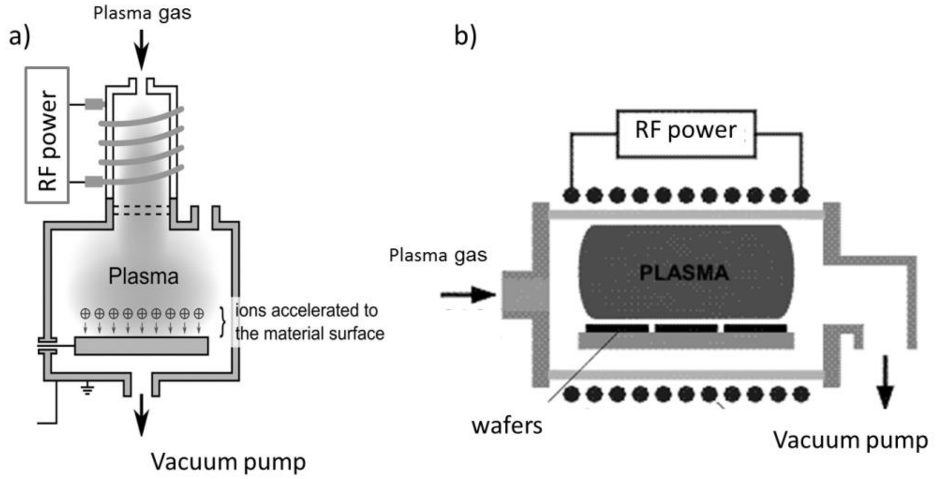

Figure 1.2: Schematic picture of an ICP source, used for plasma processing applications, in cylindrical geometry, with a helical coil placed around the discharge (a), and in planar geometry, with a flat helix or spiral positioned above (and/or below) the discharge chamber.

1.2.2. ICPs operating at intermediate pressure

ICPs at intermediate pressure (in order of several tens of Pascal) are used for lighting applications, in so-called electrode-less discharge lamps [16-17]. In contrast to the other types of ICPs, here the induction coil is typically placed inside the plasma (i.e., at the central axis), although ICP lamps with external coils do exist as well [18]. In conventional discharge lamps with electrodes, the energy is typically supplied as dc or low-frequency ac current, so that electrodes inside the tube are required to sustain the discharge. However, these electrodes are responsible for the limited lifetime of such lamps. To overcome this problem, electrode-less lamps have been developed, subdivided into low pressure, non-LTE (fluorescence) lamps and high pressure LTE lamps [17].

The most well-known, and the only commercial types of electrode-less low-pressure fluorescence lamps, are the electrode-less ICP lamps, where the energy is inductively coupled to the discharge plasma. In a re-entrant cavity lamp [19], which is one of the available designs, a ferrite core is surrounded by an isolated induction coil, placed in a cavity. The latter is surrounded by a bulb (see Figure 1.3). The discharge is ignited by an rf current, at a frequency of 2.65 MHz, which is in the band allowed for lighting. These lamps operate at a pressure below 100 Pa, which is lower than in fluorescence lamps with electrodes. The discharge gas can be argon or krypton. Besides the rare gas, mercury is also present, which is typical for fluorescence lamps. There is an additional phosphor layer at the surface of the cavity to enhance the conversion efficiency of the UV to the visible light [17].

Another ICP lamp configuration is the toroidal lamp (see Figure 1.4). This kind of lamp can be operated at a much lower frequency than the other ICP lamps (i.e. 250 kHz) and a pressure below 100 Pa, using krypton as the buffer gas. This kind of lamp is a high power, high brightness lamp, with a long lifetime, which makes it useful for inaccessible areas, like in tunnels [17].

ICP lamps with external coils also exist. They require extra electromagnetic screening by means of a Faraday cage. This lamp operates at an rf frequency of 13.56 MHz and uses neon as a buffer gas [18].

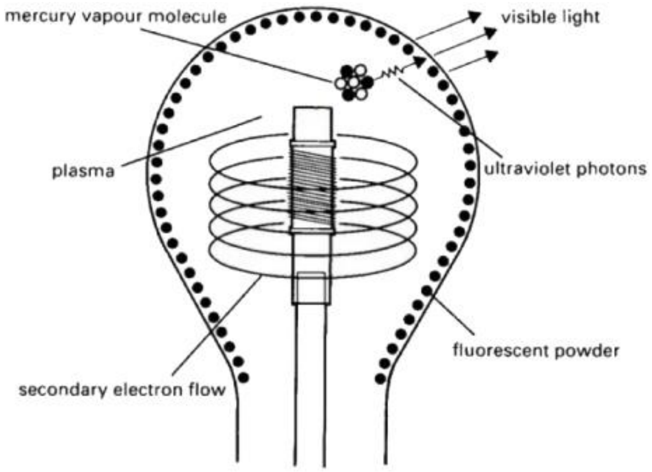

Figure 1.3: Schematic picture of re-entrant cavity ICP lamp

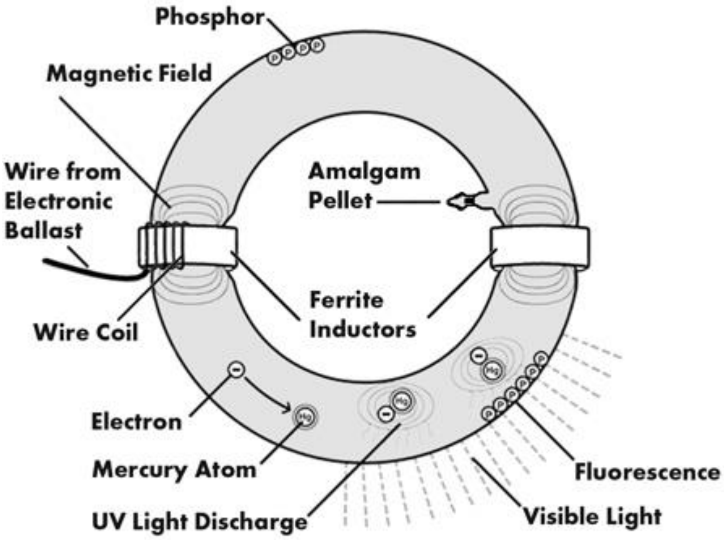

Figure 1.4: Schematic picture of toroidal ICP lamp

1.2.3. ICPs operating at atmospheric pressure

ICPs operating at atmospheric pressure are used for analytical applications, powder production and waste treatment.

In an analytical ICP, a plasma is created by applying electric power to a gas, which flows through a so-called “torch”. The torch is surrounded by a coil through which rf current is flowing. Like in the other ICP sources, this induces an electromagnetic field in the gas, causing the gas atoms to break up into positive ions and electrons. In this way, an “inductively coupled plasma” is created. The ICP is maintained because the electrons are heated by the electromagnetic field, which causes further ionization of the gas atoms. The sample to be analyzed is introduced, mostly as droplets, with an injector gas (mostly helium or argon), and will be subject to desolvation, vaporization, ionization and excitation in the plasma. The ions formed in this way can then be analyzed in a mass spectrometer, yielding ICP-MS. Furthermore, the excitation, followed by emission of radiation, creates characteristic photons, which can be detected with optical emission spectrometry, giving rise to ICP-OES (also known as atomic emission spectroscopy or AES). Indeed, ICPs are the most popular plasma sources in plasma spectrochemistry.

A typical analytical ICP is illustrated in Figure 1.5. They operate typically at atmospheric pressure, although low power (12–15 W) reduced pressure (order of 100 Pa) ICPs have also been reported for mass spectrometric detection [20]. Although the principle of inductive coupling is the same, the atmospheric pressure ICPs are clearly different from the above-described low-pressure inductive discharges used for processing applications and lamps. Indeed, at low pressure, the electrons will not undergo many collisions with the gas atoms, and they will, therefore, be characterized by rather high energy, whereas the gas temperature remains low. Hence, the low-pressure ICPs are far from LTE. In the analytical, atmospheric pressure ICP, on the other hand, the electrons undergo many collisions with the gas atoms, and they are characterized by only moderate energy (typical electron temperature of 8000–10 000 K), whereas the gas temperature is almost as high (typically 4500–8000 K) [21]. Hence, the analytical ICP is near LTE [21]. Since in the present PhD thesis the aim is to model an ICP used for mass spectrometry, we dedicate a separate section to ICP-MS and more details about the operation and applications will be presented in section 1.3. Therefore, in the current section we mostly explain ICP-OES for the analytical applications.

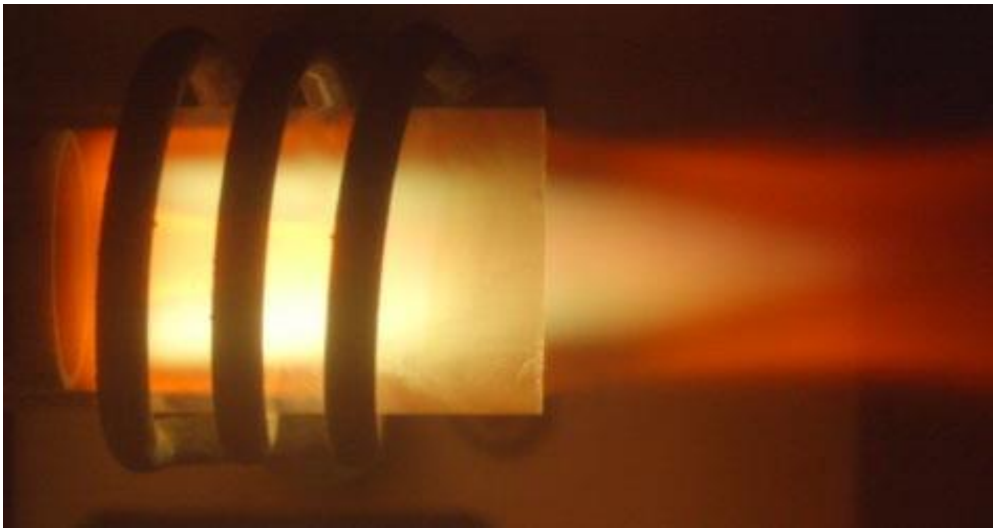

Figure 1.5: Argon plasma torch, used in analytical spectrochemistry

In ICP-OES, an optical spectrum with a typical range of 165 - 800 nm is viewed and measured, either sequentially or simultaneously. ICP-OES systems typically have two to three orders of magnitude higher detection limits than ICP-MS. However, ICP-OES can serve as a valuable analytical tool when certain lighter elements (e.g., S, Ca, Fe, K, and Se) that suffer from considerable interferences with ICP-MS require identification and quantification. Additionally, ICP-MS manufacturers have now eliminated negative ion capabilities from their instruments to reduce the cost of manufacture. This leaves ICP-OES as the only viable atomic spectroscopy method for determination of Cl, Br, and I [22,23].

The ICPs used for powder production, waste treatment, purification of both metallic and ceramic powders also typically operate at atmospheric pressure. However, they operate at much higher power than analytical ICPs, i.e., 5 to 25 KW [24]. These processes generally require a reaction chamber, which is mounted next to the torch outlet while being kept in soft vacuum [25-28]. For example, fluorescent lamp glass powders (i.e., waste-glass powders) have been treated within a laboratory scale rf thermal plasma source operated at 3 MHz with a maximum power of 25 kW, with Ar as coolant and injector gas and N_2 as auxiliary gas [24].

1.3. Inductively coupled plasma mass spectrometry (ICP-MS)

Inductively coupled plasma mass spectrometry (ICP-MS) is a method to chemically analyze several kinds of (environmental, biological and inorganic) samples. This is achieved by ionizing the sample with an ICP and using a mass spectrometer to separate and quantify the ions. A schematic illustration and a photograph of an ICP with MS interface are presented in Figure 1.6.a and 1.6.b, respectively. ICP-MS holds a unique position within the range of atomic spectrometry techniques used in analytical laboratories, because of its speed, sensitivity, dynamic range and elemental coverage. It can measure a full suite of elements in a single multi-element acquisition; it accepts almost any sample type and also provides isotopic information [29].

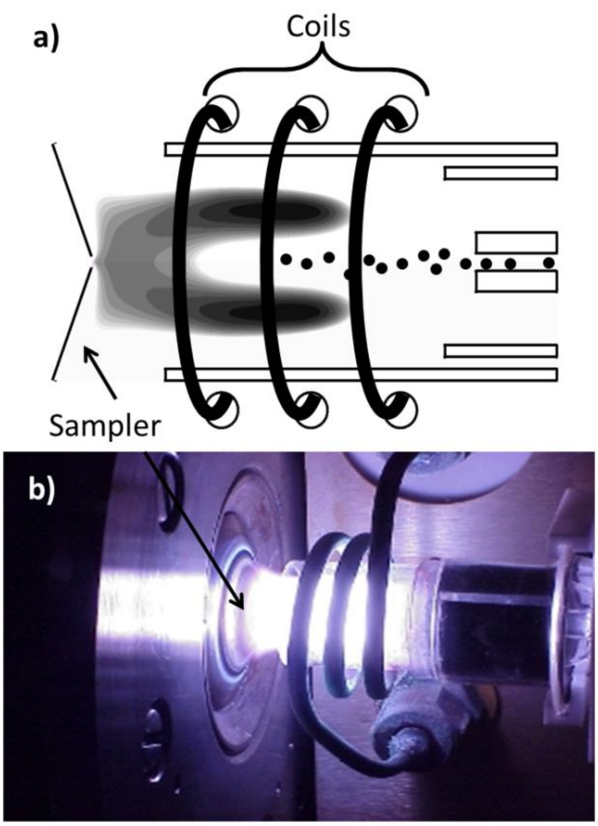

Figure 1.6: Schematic picture of an ICP with MS interface (a) and photograph of an ICP (b)

Figure 1.7 presents a periodic table, indicating (in green) which elements can be analyzed by ICP-MS, with detection limits at or below the ppt range. Elements that are in white are either not measurable by ICP-MS (the upper right-hand side) or do not have naturally occurring isotopes [30].

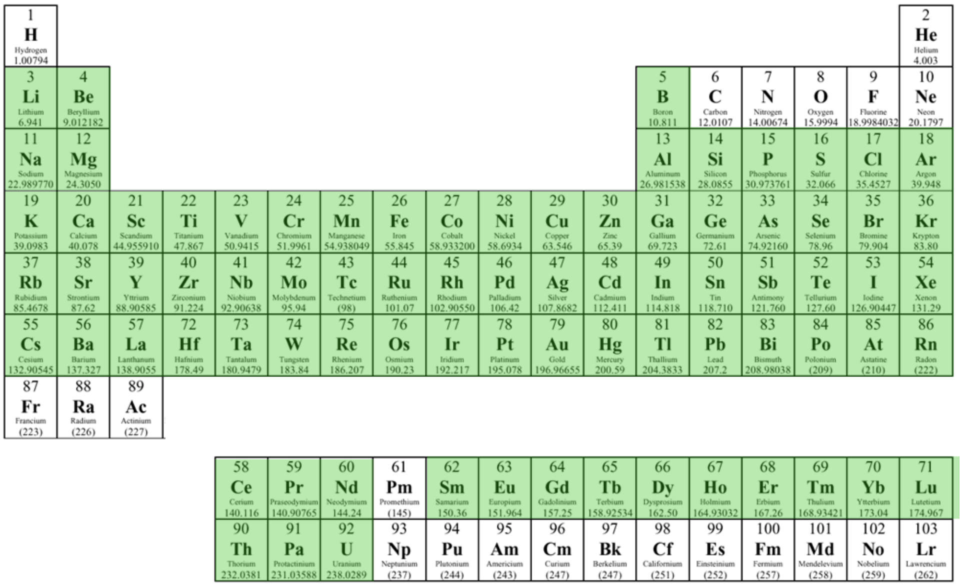

Figure 1.7: Elements that can be analyzed by ICP-MS (indicated in green) Image and permission for use provided courtesy of PerkinElmer, Inc.

In the following a summary of the various components of ICP-MS will be presented, and the most important applications will be explained.

1.3.1. ICP-MS instrumentation

An ICP-MS instrument typically consists of the following components (note that we selected the NexION ICP-MS from PerkinElmer [30] as an example here; ICP-MS instruments from other manufacturers might look slightly different):

- **The sample introduction system** provides the means of bringing the sample into the ICP. Samples can be introduced in the ICP in gas, liquid and solid state, i.e., as vapor, aerosol or cloud of particles. Injection of gaseous samples into the plasma can be done by different methods such as the hydride generation method, direct introduction and by gas chromatography [31]. Most samples introduced into an ICP-MS system are liquids. It is necessary to break up the liquid sample into small droplets before they can be introduced into the plasma. The most common liquid sample introduction is by using nebulizers (pneumatic or ultrasonic) or a spray chamber, which are continuous introduction methods [32-33]. There are also discrete sample injection devices, in which different kinds of techniques are used such as the liquid plug techniques [34], electro thermal techniques [35-36], direct insertion techniques [37], flow injection techniques [38] and liquid chromatographic techniques [39]. Introduction of solids into the plasma can also be achieved in several ways, i.e., direct sample insertion, electro-thermal vaporization, arc and spark ablation and laser ablation [31,37,40-53].

- The **ICP torch and RF coil** generate the plasma (typically in argon), which serves as the ion source for the mass spectrometer. The plasma generated in the ICP torch creates a very hot zone at a temperature of approximately 6000 °C (i.e., similar to the temperature at the surface of the sun). The plasma is generated by passing argon through a series of concentric quartz tubes (the ICP torch) that are wrapped by a radio frequency (rf) coil (See Figure 1.6 above). The energy supplied to the coil by the rf generator couples with the argon gas to produce the plasma. During their journey into the plasma, the liquid droplets (or other sample particles), containing the sample matrix and the elements to be determined, are dried to a solid and then heated to a gas. As the atoms continue their travel through the plasma, they absorb more energy and eventually release one electron to form singly charged ions (although multiply charged ions can also be formed). The ions will finally exit the plasma and enter the interface region.

- The **interface** links the atmospheric pressure ICP ion source to the high vacuum mass spectrometer. Indeed, the plasma, operating at 6000 °C, is placed near an ion focusing device operating near room temperature. In addition to a large temperature difference, the plasma operates at atmospheric pressure, hence much higher than the vacuum required by the ion lens and mass spectrometer. The interface allows the plasma and the ion lens system to coexist and makes sure that the ions generated by the plasma can pass into the ion lens region. The interface consists of two cones: a sampler and skimmer cone (see Figure 1.8). The cones are most often produced from nickel or platinum. The orifice of the cones should be large enough to allow the ion beam to pass, while at the same time, it should not allow that too much gas can enter the mass spectrometer, in order not to disturb the vacuum system. The typical size of the orifice is 1 mm.

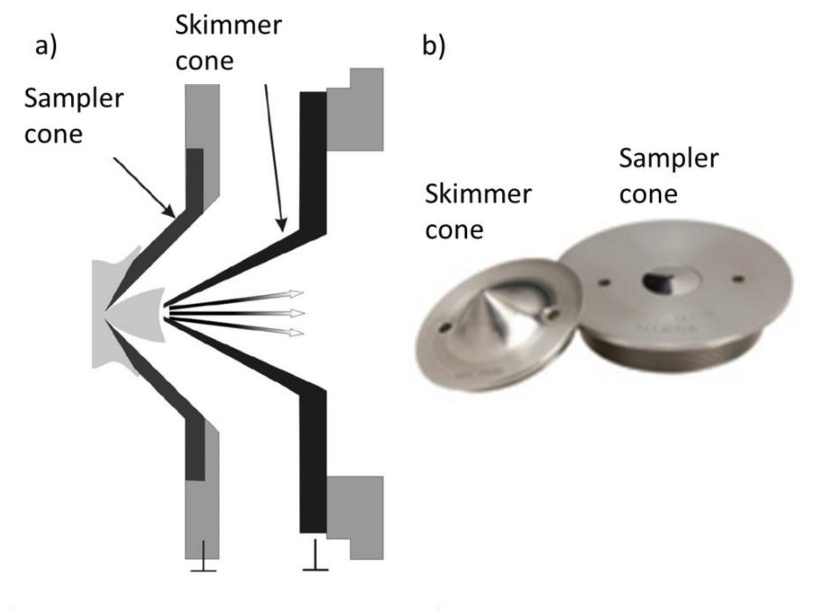

Figure 1.8: Schematic picture of sampler and skimmer cone (a) and picture of sampler and skimmer cones for NexION 300 ICP-MS, PerkinElmer (b). Image, schematic and permission for use provided courtesy of PerkinElmer, Inc.

- The **vacuum system** provides high vacuum for the ion optics, (quadrupole) mass spectrometer and detector. The distance from the interface to the detector of an ICP-MS is typically 1 meter or less. If an ion travels that distance, it should not collide with any gas molecule. This requires the removal of nearly all of the gas molecules in the space between the interface and the detector. This task is typically accomplished using a combination of a turbomolecular pump and mechanical roughing pump, which comprise the main components of the vacuum system. The turbomolecular pump works like a jet turbine and is capable of rapidly pumping a chamber to a pressure of 10^{-5} Torr or less. The roughing (mechanical) pump backs up the turbomolecular pump and evacuates the interface region.

- The **ion deflector** performs an essential function of separating the ions from the photons and residual neutral material. Agilent uses a high transmission off-axis or “Omega” lens arrangement that separates the positively charged ions from the photons and neutral particles, which would otherwise reach the detector and increase the random background noise [29]. PerkinElmer, however, uses a quadropole ion deflector. The ion beam exiting the interface region of the instrument contains some non-ionized materials (i.e., neutrals) and photons. The analyte ions need to be separated from the neutrals and photons. Indeed, neutrals can collect on sensitive components of the instrument, thereby creating drift. Moreover, photons that reach the detector can be erroneously counted as ions,which increases the background and deteriorates the detection limits. A quadrupole is typically used as a mass-filtering device, where the ions travel in a path parallel to the rods. The quadrupole seems to work in the optimum configuration if the ion beam is allowed to pass at the right angle (perpendicular) to the rods. Hence, when the quadrupole is placed at the right angle to the ion beam and immediately between the interface region and the filtering quadrupole, ions can be efficiently transmitted, while neutrals and photons are readily removed from the ion beam. As is shown in Figure 1.9, the ions are turned by the quadrupole at the right angle for their entry into the filtering quadrupole or universal cell.

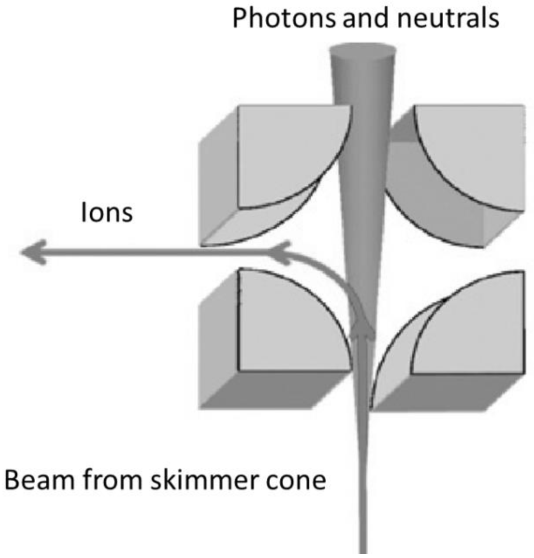

Figure 1.9: Schematic picture of a quadrupole ion deflector. Schematic and permission for use provided courtesy of PerkinElmer, Inc.

- A **collision/reaction cell** typically precedes the mass spectrometer and is used to remove interferences, which would otherwise deteriorate the detection limits that can be achieved. It is possible to have a cell that can be used both in the collision cell and reaction cell modes, which is referred to as a universal cell. An energy barrier is placed at the exit of the cell, and can be adjusted so that the higher-energy analyte ions are allowed to pass through, while the lower-energy interferences are not.

• The **mass spectrometer** acts as a mass filter to sort ions by their mass-to-charge ratio (m/Z). Three main types of mass spectrometers are used in commercial ICP-MS systems, i.e., quadrupole, time-of-flight, and magnetic sector instruments. For the overall performance and economic value, most laboratories work with an ICP-MS with a quadrupole mass spectrometer (e.g., Agilent 7500 series, NexION 300 PerkinElmer). A quadrupole works by setting voltages and radio frequencies to allow ions of a given mass-to-charge ratio to remain stable within the rods and pass through to the detector. Ions with different mass-to-charge ratios are unstable in the cell and are ejected. To cover the full mass range, the electronics rapidly change the conditions of the quadrupole to allow different mass-to-charge ratio ions to pass through. Under the control of the instrument software, the mass spectrometer can move to any m/Z needed to measure the elements of interest in the sample analyzed. The quadrupole is then stepped to cover the m/Z that is appropriate for all elements to be analyzed. Although it is actually a sequential device, the quadrupole is capable of scanning at a rate > 5000 atomic mass units (amu) per second. This is the reason that ICP-MS can determine so many different elements quickly, even though only one mass passes through the quadrupole at a certain time.

• The detector counts individual ions exiting the mass spectrometer. These ions reach the active surface of the detector and generate a measurable electronic signal. The active surface of the detector, known as a dynode, releases an electron for each ion that arrives, and then it starts the amplification process. The electrons released from the first dynode strike a second dynode where more electrons are released. This cascading of electrons continues until a measurable pulse is created. By counting the pulses generated by the detector, the system counts the ions that hit the first dynode. The software compares the intensities of the measured pulses to those from standards, which make up the calibration curve, to determine the concentration of the element. For each element measured, it is typically necessary to measure just one isotope, since the ratio of the isotopes, or the natural abundance, is fixed in nature. However, ICP-MS can also be used to measure the individual isotopes of each element, and this capability is of high value for laboratories interested in one specific isotope of an element or in the ratio between two isotopes of an element. The detectors used in commercial instruments are capable of reaching a wide dynamic range using a dual mode, which includes both digital and analog modes. Rapid data acquisition rates allow the ICP-MS to be used in the analysis of nano-particles [29,30,54,55].

- Finally, a **data handling and system controller** controls all aspects of the instrument, to obtain the final concentration results of elements in a given sample.

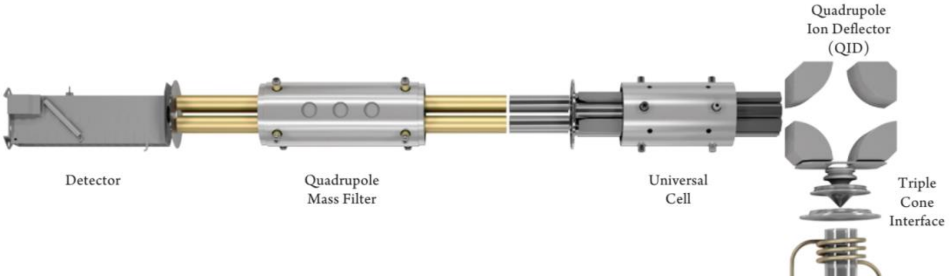

Figure 1.10: The ion optic path of the PerkinElmer NexION ICP-MS. Image and permission for use provided courtesy of PerkinElmer, Inc.

The whole ion optic path of an ICP-MS is shown in Figure 1.10.

1.3.2. ICP-MS applications

Because of its high sensitivity and ability to measure about 80% of the periodic table, the ICP has become one of the most popular ion sources in analytical chemistry, as a method for determining trace elements and isotopes in a wide variety of samples, for biological, geological, environmental and industrial (materials science) applications [31,56].

For biological materials it is possible to determine the elemental composition, but also to use stable isotopes as tracers. Biological materials that have been analyzed by ICP-MS in the past, include (1) animal tissue and body fluids, including organs, hair, muscles, bones, blood, faeces, and urine [57-60], (2) plant tissue, including samples of terrestrial plants, aquatic plants and humic materials [31,61,62], and (3) food products and related substance [31,63,64].

Moreover, the high-sensitivity multi-element capability of ICP-MS makes it an ideal technique for comprehensive rock and mineral analysis in geological studies, especially for lanthanide elements for example from granite [65-72]. Moreover, precious metals (e.g. Au, Ag, Pd, Pt,…) can be effectively determined in nickel sulfide after only classical fire assay separation [73].

Furthermore, the chemical composition of air, water, soil and living matter, which is important information for environmental studies, can also be studied by ICP-MS, including deficiency, toxicity, and sublethal dose-response characteristics, as well as for instance various size fractions of suspended matter in surface water, or air particulates collected on a high volume filter [74-76].

Finally, ICP-MS is also routinely used in industrial applications, such as for the determination of trace elements in metallurgical materials. Because of its high sensitivity, it is an ideal technique for the determination of low-concentration-level contaminants that potentially affect the physical properties of an alloy [77-79].

1.4. Fundamental studies on an ICP to improve the analytical applications

ICP-MS was commercially introduced in 1983 [80], only three years after the demonstration of the possibilities offered by the ICP-MS technique [81]. In the meantime it has gained general acceptance in all types of laboratories, ranging from academic research to service labs and industry [21,31].

To improve the analytical applications, fundamental studies of the ICP are indispensable, and have been carried out in both experimental [82-119] and computational groups [120-181].

1.4.1. Experimental investigations

In ICP-MS, the ions are sampled from the plasma by the insertion of a sampling cone into the plasma. As this (metal) sampling cone is relatively cool compared to the plasma temperature, it results in changes in the composition of the plasma gases that come in contact with the metal surface. Indeed, a boundary layer of cooler gases is formed along the surface of the metal. A detailed discussion about the boundary layer between the plasma stream and the sampler orifice, as well as sample introduction, ionization and ion extraction in ICP-MS was already presented in 1981 by Houk et al. [82]. Later on, several studies have reported on ICP characteristics in the presence of a MS sampling interface. Many studies focused on the downstream region from the interface e.g. [83-86], but did not give information on changes in the plasma itself. In [87-95], the upstream region, i.e., the plasma, was investigated, but no comparison was made with and without sampling interface. A detailed comparison of the plasma characteristics with and without sampling interface was made experimentally by Houk and group members [96,97], Farnsworth and coworkers [98] and Hieftje and group members [99]. Lehn et al. [99] reported that the presence of the interface causes changes in the fundamental plasma characteristics such as electron number density and gas kinetic temperature, whereas Ma et al. [98] used laser-induced fluorescence to investigate the effect of the sampling interface on the analyte atom and ion distributions in the ICP used as ion source for elemental mass spectrometry.

Moreover, a large number of investigations were performed to study the effect of ICP operating conditions on the plasma characteristics, in order to optimize the analytical performance [100-110]. However, most of these studies have focused on the effect of the operating conditions on the overall instrument performance and not on the upstream plasma [102-107]. Effects of the rf power, nebulizer flow rate, sample composition and torch-shield configuration on the ion-transport efficiency through the ICP-MS interface have been studied via laser-induced fluorescence upstream and downstream from the sampler by Macedone et.al. [100]. The same authors [110] also showed that the barium ion number density in the plasma upstream from the sampler drops as the sampling depth is reduced. Gamez et al. performed Thomson and Rayleigh scattering measurements using an imaging-based instrument for fundamental plasma studies. It was found that the perturbation in radial distribution of electron density and the drop in gas temperature due to the MS interface change with applied rf power, central gas flow rate and sampling depth [108,109].

Besides the optimization of the operating parameters, the effect of geometrical parameters has also been of considerable interest. In 1983 Gray and Date [111] already reported that larger sampler orifice diameters than those in boundary layer sampling (i.e., 50-80μm diameter range) were needed for sampling the bulk plasma (at least 0.2 mm diameter). However, with these larger orifice diameters another problem arose, i.e., a secondary discharge between the plasma and the sampling cone developed, as had also been already explained by Houk et al. [82]. The formation of this discharge was also discussed in [97,112]. Lichte et al. [113], however, reported that due to deposition of material, the sampling orifice becomes smaller and the metal-to-metal oxide ion ratios change. Crain et al. [114] reported that matrix effects are affected by the ratio of sampler and skimmer orifice diameters. Vaughan and Horlick [115] also varied the sampler and skimmer orifice diameters, and indicated that the sampler orifice diameter has a major impact on the signal characteristics. Indeed, for oxide forming elements, the MO^+/M^+ signal ratio appeared to be very dependent on the orifice diameter. This was also reported by Longerich et al. [116]. In addition, the sampling orifice diameter changes the shape of the signal versus nebulizer flow rate [115,116]. Furthermore, Vaughan and Horlick also indicated that the sampling orifice is the primary location for oxide formation in ICP-MS. However, the range of sampler orifice diameters in their study was from 0.51 to 0.94 mm, which is smaller than the range of more recent designs (i.e. larger than 1 mm). They also investigated the effect of the skimmer orifice diameter on the analyte signals and reported that this effect is not as dramatic as the effect of the sampler orifice diameter. In the range of small orifices, i.e., below 1 mm and using LA-ICP-MS, Günther et al. also reported that by decreasing the sampler cone orifice size (from 0.7 to 0.5 mm), many background intensities can be reduced by up to two orders of magnitude, while maintaining comparable sensitivity [117].

Finally, Taylor and Farnsworth recently investigated the effect of skimmer cone design (for five commercially available skimmer designs) on the shock formation and ion transmission efficiency in the vacuum interface of an ICP-MS [118]. They reported that the strongest shock was recorded for a skimmer with a cylindrical throat, and the weakest shock was produced by the skimmer with the largest diameter and a conical throat. The transmission efficiency increased with increasing skimmer orifice diameter.

These observations all suggest that the use of interfaces with different orifice sizes can make a change in the detection efficiency. In addition to the effect of sampler and skimmer orifice diameter, the place of the sampler itself was also investigated experimentally. Gamez et al. studied the effect of sampling position on the plasma characteristics of an ICP [109] and reported that as the MS interface is brought closer to the ICP load coil, the upstream plasma temperature dropped. Finally, Macedone et al. also showed that the barium ion number density in the plasma upstream from the sampler drops as the sampling position is reduced [110].

In order to optimize the efficiency of material transport, it is also crucial to study the occurrence of recirculation of the gas and to optimize the flow path lines. Although the operating and geometrical parameters can also influence the flow path lines inside the torch, this effect has not been thoroughly investigated experimentally as it is difficult to measure the gas flow characteristics along the entire ICP torch. Moreover, researchers are mostly interested in the region of the coil and after the coil in the case of ICP-OES, and in the sampler cone region in the case of ICP-MS. Nevertheless, the presence of recirculation has been confirmed by high-speed photography of plasma fluctuations by Houk et al. [119]. The authors indicated that the recirculation can be observed in horizontal plasmas as well as vertical plasmas. However, the insertion of a sampling cone blocks the downstream region where the rotations are prominent. Therefore, the rotations observed from yttrium oxide emission were found to be less evident in the presence of a sampler.

1.4.2. Computational investigations

Besides experimental studies, computer modeling has also contributed a lot towards a better understanding of the plasma characteristics and gas flow dynamics in an ICP. Various modeling efforts have been reported in literature by several groups [120-170]. Most of the pioneering work on ICP modeling was performed by Mostaghimi, Proulx and Boulos [121-138]. They applied a so-called “particle-source-in-cell” (PSI-Cell) method [120] to describe the injection of powders into an ICP torch with the assumption of 1D electro-magnetic fields [121-124]. They reported that the effect of plasma-particle interaction on the temperature field could be very significant. They also made a comparison between two different algorithms used for the computation of the flow and temperature fields in an ICP. The results showed that the formulation of the mathematical model and the chosen numerical technique can substantially influence the stability and the convergence of the solution [125]. However, the operating conditions were not always applicable for analytical chemistry purposes. Moreover, the ICP torch was not connected to a MS interface, so the relevance for ICP-MS was limited. Moreover, the gas viscosity is ignored in their model.

In collaboration with Barnes, this group developed a model for the calculation of the two-dimensional emission pattern from a spectrochemical ICP [126]. Assuming LTE, the flow, temperature and the concentration fields were computed and used to estimate the population density of different species present in the plasma, and accordingly the emission pattern for different atomic and ionic lines. The effects of the concentration of the analyte and their ionization energy on the emission patterns and on the analytical curves were demonstrated.

Subsequently, they proposed a two-temperature model for the computation of the two-dimensional flow and temperature fields in an rf ICP torch. The model was applicable to monoatomic gases. The results obtained for an argon plasma indicated that deviations from LTE were relatively small at atmospheric pressure, but at reduced pressure, substantial deviations from LTE were noted. Compared to LTE calculations, the non-LTE model predicted lower radiation losses and higher wall conduction [127]. Further investigations [128] showed that deviations from LTE were strongly related to the induction frequency. Calculations were carried out for an argon plasma at atmospheric pressure over the frequency range 3-40 MHz, and it was found that higher frequencies resulted in a larger difference between the electron and the atom/ion temperatures.

This group also presented a so-called standard k-ϵ model of turbulence for the determination of the flow and temperature fields in an rf ICP. Due to the large diffusion terms and fast decay, the central flow could not penetrate the discharge region in such a model. The effect of swirl in the sheath gas was found to increase the turbulence and to decrease the size of the discharge. The results indicated the presence of both laminar and turbulent regimes in the same flow field [129]. A more realistic two-dimensional representation of the electromagnetic fields in an rf ICP was presented in [130,131], as this can have an important influence on the energy distribution in the plasma. A three-dimensional laminar model for the prediction of the mixing pattern of single and multiple cold jets with a transverse plasma flow was presented in [132].

Furthermore, two numerical models (i.e., a chemical equilibrium and a kinetic model) for the analysis of chemical reactions in an rf plasma chemical reactor were formulated in [133, 134]. The gas flow and the temperature and concentration fields calculated with each model were compared, and the comparison showed that higher temperatures were predicted in the reactor by the chemical kinetic model. However, the concentrations of the different species predicted by the two models were very similar. Also the influence of radiative energy losses on the flow and temperature fields was studied, both for a pure argon ICP and an argon plasma in the presence of small concentrations of copper vapor [135]. Besides argon plasmas, the group also performed computer simulations for helium ICPs [136, 137] and argon-nitrogen mixtures [138]. Finally, they proposed an extended geometry for the electro-magnetic fields, hence not limited to the torch diameter [139] which allows the use of simpler boundary conditions in the so-called ‘open torch’ modeling, compared to ‘closed’ torches, i.e., not taking into account the gas flow to the ambient environment [140].

Benson, Montaser and colleagues performed some computational studies on droplet heating, desolvation and evaporation in an ICP [141-143]. The total desolvation rate of sample droplets in an argon ICP was investigated through the development of a two-phase continuum flow computer model. The desolvation model was extended by equations determining the trajectories of the particles through the plasma. The model was used to calculate the behavior of aerosol droplets from a direct injection high efficiency nebulizer (DIHEN). Two separate techniques, i.e., based on the Stokes equation and a direct simulation Monte Carlo treatment for determining the droplet trajectories, were compared [141, 142]. Moreover, droplet coalescence along with transport, heating and desolvation was studied, considering droplet-droplet interactions. The simulations predicted spatial maps of the droplet number and mass densities within the ICP for a conventional nebulizer-spray chamber arrangement, a DIHEN, and a large bore DIHEN (LB-DIHEN) [143].

The group of Colombo, Bernardi, Ghedini, Sanibondi, Mentrelli, and colleagues in Bologna also showed a lot of modeling activities for ICP torches, albeit mostly not for analytical chemistry conditions, but typically at higher power values (e.g., 5-25 kW) [144-159]. They developed a three-dimensional model by means of the commercial computational fluid dynamics code FLUENT. The helicoidal coil was taken into account, showing the effects of its non-axisymmetry on the plasma behavior [147]. Also different coil configurations, such as planar, elliptical, and double-stage, were studied [148,149]. The model was typically applied to higher power conditions (e.g., 25 kW [150]), but a study was also performed at a power of 300 W and a frequency of 40 MHz chosen for spectroscopic analysis, in collaboration with Mostaghimi [151].

The same group also studied the trajectory and heating history of powders injected with an injector gas into the ICP, taking into account the effects of coupling between particles and plasma, but again in a higher power range (10-25 kW) [152,153]. The effects of powder feed rate, injection probe position and frequency on the plasma and particle temperature were investigated in [154]. In [155,156] a turbulent model for an ICP torch working at a power range of 10-15 kW was presented. Furthermore, two-temperature thermodynamic and transport properties of argon-hydrogen and nitrogen-hydrogen [157] as well as carbon-oxygen [158] plasmas were studied. Finally, a model for the optimization of the reaction chamber for silicon nanoparticle synthesis by an rf ICP was reported in [159, 160]. Moreover, the backward motion of the gas flow could also be seen (although it was not discussed) in [148], which presents a numerical simulation of an ICP torch at atmospheric pressure.

Shigeta and coworkers also did outstanding computational work on rf-ICP torches [161-171]. A numerical analysis was conducted to investigate the synthesis of nanoparticles using a rf-ICP [161-163]. Since the aim of most of their studies was the production of nanoparticles, the size of the modeled torches was larger than the typical torches using in analytical chemistry applications (i.e., a length of 180 mm and a diameter of 45 mm). Moreover, the external power was higher and the current frequency was lower than the ones used in ICP-MS/OES (i.e., 5-16 kW and 4 MHz, respectively). In [164-165] an advanced rf-ICP reactor was modeled in which the plasma flow was generated by adding a direct current (dc) discharge to a conventional rf-ICP flow in order to overcome the disadvantages of a conventional flow. A two-dimensional model as well as a one-dimensional model was introduced for nanoparticle growth to investigate the effects of the spatial distributions of the thermo-fluid fields in the rf-ICP flows on the synthesized nanoparticles. In the advanced rf-ICP flow, the characteristic recirculation zone disappeared due to the dc plasma jet, and larger numbers of nanoparticles with smaller size could be produced by using this advanced rf-ICP flow. Later on, a time-dependent 3D numerical simulation was conducted to study the thermo-fluid dynamics of an argon rf-ICP with a direct-current (dc) plasma jet assistance, considering non-uniform density and temperature profiles in time and space as well as turbulence generation and suppression [166]. The flow field had a complicated 3D structure with a recirculating zone due to Lorentz forces. Because of the recirculating flow, the injected cold gas tended to avoid the high-temperature plasma region. The largest vortex structure, at approximately 10000 K, remained in the plasma region, whereas small cold eddies were generated near the top wall of the torch and transported downstream, avoiding the plasma region [167]

Moreover, the same authors studied how the number density, diameter and specific surface of the produced nano metal-particles were influenced by the operating conditions such as the quenching gas flow rate and the powder feed rate of the rf-ICP reactor [168]. Furthermore, the effects of several cooling methods on the formation mechanisms of the nanoparticles in distinctive thermo-fluid fields were discussed [169]. Also, a non-equilibrium modeling of argon-oxygen and argon-hydrogen induction thermal plasmas was performed without thermal and chemical equilibrium assumptions. Reaction rates of dissociation and recombination of diatomic gas and ionization were taken into account with two-temperature modeling. A substantial deviation from LTE exists near the torch wall in the argon-oxygen induction plasmas under atmospheric pressure, while a small deviation in the argon–hydrogen plasmas results from the large collision frequency between electrons and hydrogen atoms [170,171].

Benoy and van der Mullen at Eindhoven University also developed a model for an ICP, based on non-LTE, by solving the conservation laws of mass, momentum and energy [172]. The model included the macroscopic fluid dynamics, as well as the atomic collisional and radiative processes. The model was applied to a relatively large ICP at low frequency (3 MHz) and a relatively small ICP at high frequency (100 MHz). The description of the first ICP was found to be relatively simple, although the plasma depends strongly on the choice of the source terms, i.e., the ionization and recombination rate coefficients and the radiative loss term. The description of the second ICP turned out to be much more complicated, and it was concluded that due to the high energy densities, steep gradients and strong transport, the exact knowledge of the transport processes was crucial, and the numerical solution was found to be less stable [172].

At the Von Karman Institute for Fluid Dynamics in Brussels some modeling efforts were also reported for an ICP [173-176]. However, this model was again not applied to analytical spectrochemistry conditions, but it was developed for space vehicle re-entry experiments in a wind tunnel, using a so-called plasmatron ICP operating up to 1.2 MW.

To our knowledge, the first theoretical studies directly relevant for ICP-MS were conducted by Douglas and French [177], who presented an approximate model of ideal gas flow through the sampling cone of an ICP, i.e., the so called “hemispherical-sink model”. This model assumes that the gas flow toward the nozzle behaves like a flow in a duct. In a first approximation, the area of the duct at a specific point with radial distance R in a spherical geometry was taken equal to the area of the sampler orifice plus $2\pi R^2$. This made it possible to obtain the Mach number as a function of R and subsequently, the fluid quantities such as temperature and number density could be achieved. Spencer et al. [178-179] applied a Direct Simulation Monte Carlo algorithm to simulate the flow of neutral argon gas through the first vacuum stage of the ICP-MS and found a good agreement with the approximate hemispherical sink model of Douglas and French. Their calculations yielded plasma velocity data in the region a few millimeters upstream from the sampler which were in reasonable agreement with experiments. However, the upstream density and plasma temperature gradients were not included and no plasma was assumed in these models. Furthermore, the authors provided a formula for the Mach number as a function of distance along the central axis, which may be used to predict the variation of velocity, density and temperature along the central axis near the sampler [179].

Finally, Lindner et al. developed a model for an atmospheric pressure ICP, operating at typical analytical chemistry conditions, and focusing on the gas flow dynamics and plasma formation [180]. To our knowledge, this is the first model applied to the condition of analytical spectrochemistry applications, which takes viscosity and ionization into account, and can trace the gas flow from the injector inlet to the sampler cone, as well as calculate the plasma characteristics inside the entire ICP torch. A model was developed in which the transport parameters are calculated for arbitrary mixtures of atomic species. The calculated values for viscosity and thermal conductivity are found to be in good agreement with literature data in the relevant temperature range. The data were derived only from the data for the pure elements. For the mixtures, a simple approximation (see section 2.5.1 below) was used for neutral-neutral and neutral-charged collisions. Thus, the data may not be as exact as if calculated taking into account the specific interaction. Nevertheless, the relative deviation does not increase for mixtures compared to pure elements [180]. Thus, the model is applicable with reasonable accuracy. The advantage of this model is that only atomic-radius-data of the pure elements are required and the calculation can be performed in a rather straightforward manner. A validation of that model by experiments was provided in [181]. That model serves as the basis for the modeling work performed during this PhD thesis (see below).

1.5. Aim of this PhD thesis

The aim of this PhD thesis is to simulate an ICP torch which is connected to a mass spectrometer interface, for a better understanding of ICP-MS. The model needs to take ionization into account (i.e., plasma formation) and should be able to trace the gas flow from the injector inlet to the sampler cone, as well as calculate the plasma characteristics inside the entire ICP torch, in the presence of a MS interface.

For this purpose, the model developed by Lindner is used as the starting point. In first instance, we will numerically investigate the effect of the presence of a sampler on the fundamental plasma characteristics in ICP-MS. To our knowledge, such a detailed computational study has not been carried out before.

Furthermore, we aim to systematically investigate the effect of the operating conditions on the upstream plasma characteristics of the ICP in contact with this MS interface. Thus, a wide range of injector and auxiliary gas flow rates will be applied. Moreover, the effect of the applied power will be studied in detail. Also, the effect of the sampler distance and sampler orifice diameter on the plasma characteristics of the ICP will be investigated.

Finally, we aim at obtaining a better insight in the occurrence of the backward gas flows (i.e., recirculation) in the torch and we hope to be able to predict under which operating conditions this recirculation behavior can be controlled. This is especially true for the injector gas flow, which carries the sample, because any deviation from the central axis leads to a longer transit time and hence a loss of intensity and this should be avoided.

The model developed in order to achieve these goals will be explained in Part II (Chapters 2 and 3). The results of each modeling study will be presented in Part III (Chapters 4 to 7). Finally, an outlook for future work will be presented in Chapter 8.

PART II: Description of the model

Chapter 2:

Theoretical background

In this chapter, first some general considerations used to build the model will be presented, followed by the physics of the inductively coupled plasma and the related equations.

2.1. General considerations

The model is developed by means of the commercial computational fluid dynamics program FLUENT (ANSYS) [182], to which several self-written modules were added as user defined functions (UDFs). A two-dimensional (2D) axisymmetric geometry is assumed, and a schematic diagram of the setup is presented in Figure 2.1. The diameter of the central inlet and sampler orifice as well as the distance of the sampler from the load coil will be varied.

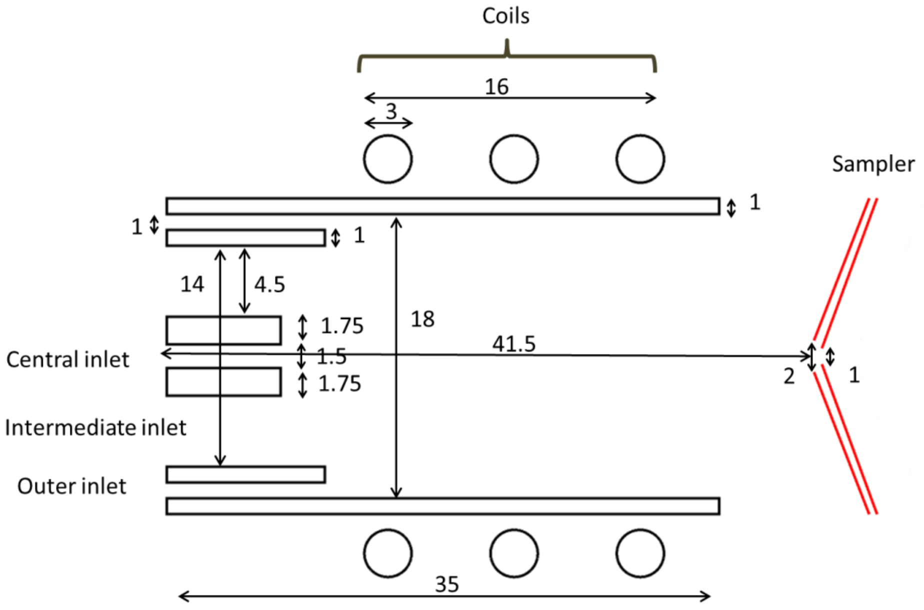

Figure 2.1: Schematic picture of the ICP geometry as an example for the geometry used in the simulations. The numbers represent the distances in mm.

The gas enters through the three concentric tubes of the ICP torch, and flows into an open ambient gas, which is taken to be argon for simplicity. The volume flow rate of the gas through the outer torch tube (called here “coolant gas”), the intermediate torch tube (called here “auxilliary gas”) and the central tube (called here “injector gas”) will be varied in the next chapters, to investigate their effect on the calculation results. Note that in literature different terms are being used for these gas flows, i.e., the coolant gas is also called plasma, cooling or outer gas, the auxiliary gas is also called sheath gas, and the injector gas is also called carrier or central gas. However, in this thesis we constantly use the terms coolant, auxiliary and injector gas. The flow rate of the ambient gas is determined by the pressure difference between the ambient pressure (101325 Pa) and the pressure set for the exhaust (101225 Pa). The flow was treated to be laminar, which is justified as the Reynolds number is typically in the order of 100 for regions close to the sampler, and certainly below 1000 for regions close to the inlets, for the most of conditions under study, so it is far from the turbulence regime (See chapter 7).

It is shown in Figure 2.1 that we assume the coils to be perpendicular to the ICP torch. This more or less justifies the use of a 2D model as there is symmetry in the φ direction. It should be noted, however, that in real ICP instruments, the coils wrap the torch not exactly perpendicular. Therefore, the plasma is not fully symmetric and modeling in 3D provides a higher accuracy. However, it is studied in [154] that by increasing the frequency of the external current from 3 MHz to 13.56 MHz, the asymmetric effect of the coil orientation on the plasma temperature decreases. In the present study we consider a frequency of 27 MHz (i.e., two times higher than 13.56), so we expect that the temperature profile would be more close to symmetric, even in a 3D study.

As will be discussed in detail further in this chapter, the gas flow dynamics are calculated with the Navier-Stokes equations. The power coupling in the ICP is accounted for by Ohm’s law. The power coupling is a source term in the energy conservation equation, whereas the emitted radiation is treated as a loss term. The viscosity of the mixture (consisting of various heavy species, such as the gas atoms and ions, as well as the electrons), the heat capacity, thermal conductivity and diffusion coefficients of the species are defined in the model as user defined functions (UDFs), being a function of the actual gas composition and the plasma temperature.

The model assumes local thermodynamic equilibrium (LTE), and a motivation for this was given in [180]. Although the assumption of LTE is not fully correct, the use of two-temperature models does not necessarily yield significantly different temperatures for electrons and heavy species [140]. Moreover, the results obtained for an argon plasma by Mostaghimi et al. indicated that at atmospheric conditions, deviations from LTE are relatively small. However, the situation is different under reduced pressure conditions [127]. Therefore, it is believed that the assumption of LTE closely approaches the accuracy of non-LTE models for the present plasma. Moreover, the LTE assumption has the advantage that the model can be more easily formulated in a self-consistent way and it requires less other assumptions, e.g., on power coupling and energy transfer from electrons to atoms and ions.

Based on this LTE assumption, the ionization is described by the Saha-Eggert-equation. Furthermore, based on the assumptions of quasi-neutrality and conservation of heavy particles of each element, in combination with the calculated ionization degree, the number densities of all species (various atoms and ions, as well as the electrons) can simply be calculated. In the case of pure argon, the species taken into account include the Ar atoms, Ar^+ and Ar^{2+} ions and the electrons. The conditions (i.e., both geometrical parameters and operating conditions) to which the model will be applied in the next chapters are listed in Table 2.1. The next sections describe the various aspects of the model in more detail.

Table 2.1: Geometry and range of operating conditions to which the model will be applied in the next chapters.

Table 2.1 Operating and boundary conditions	
Frequency	27 MHz
Input power	750 - 1500W
Injector gas flow rate	Ar; 0.3 - 2.5 L/min
Auxiliary gas flow rate	Ar; 0.3 - 1.2 L/min
Coolant gas flow rate	Ar; 12 - 16 L/min
Ambient pressure	101325 Pa
Exhaust pressure	101225 Pa
Pressure downstream the sampler cone	1.32×10^{-3} atm (1 torr)
Injector inlet diameter	1.5 – 2 mm
Inlet gas temperature	297 K
Sampler cone temperature	500 K
Sampler orifice diameter	1 – 2 mm
Sampler distance from the load coil	7 – 17 mm

2.2. Gas flow dynamics

We need to solve conservation equations for mass and momentum for all gas flows. For flows involving heat transfer (as in the current study), an additional equation for energy conservation also needs to be solved. In this section, the conservation equations for laminar flow in an inertial (i.e., non-accelerating) reference frame are presented. The source terms of the conservation equation will be explained in detail in a separate section (see section 2.4). Moreover, the species transport will be presented in this section.

2.2.1. Conservation equations for momentum, mass and energy

The gas flow dynamic equations are solved by FLUENT, assuming laminar flow conditions. The calculations are made for a two-dimensional axisymmetric geometry. For conservation of momentum, the Navier-Stokes equation has the following general form:

$$\rho\left(\frac{\partial v}{\partial t}+(\vec{v}\cdot\nabla)\vec{v}\right)=-\nabla p+\nabla\cdot\bar{\tau}+F \tag{1}$$

where ρ is the mass density, v is the velocity, p is the pressure, $\bar{\tau}$ is the stress tensor and F is the body force (per unit volume). The left hand side of the equation describes acceleration, and is composed of time dependent and convective effects. Note that also the effects of non-inertial coordinates can be included, but this is not the case in the present study. The right hand side of the equation denotes the divergence of stress (i.e., pressure and shear stress, first and second terms respectively) and the summation of body forces (third term). More specifically, the effect of stress in the fluid is represented by the ∇p and $\nabla\cdot\bar{\tau}$ terms; these are gradients of surface forces. Here ∇p is called the pressure gradient and originates mainly from the difference between inlet and outlet pressures and partially from the electron distribution. The anisotropic part of the stress tensor gives rise to $\nabla\cdot\bar{\tau}$ which conventionally describes viscous forces. For incompressible flow, this is only a shear effect. In the current study, the term “F” is represented only by the Lorentz force, which will be explained in section 2.4.1 below.

Since we use cylindrical coordinates, we rewrite the equation in the relevant directions. Therefore, the momentum conservation equation in the axial direction is:

$$\begin{aligned}\frac{\partial}{\partial t}(\rho v_z)+\frac{1}{r}\frac{\partial}{\partial z}(r\rho v_z v_z)+\frac{1}{r}\frac{\partial}{\partial r}(r\rho v_r v_z) &= -\frac{\partial p}{\partial z}+\frac{1}{r}\frac{\partial}{\partial z}\left(r\eta\left[2\frac{\partial v_z}{\partial z}-\frac{2}{3}(\nabla^*\cdot\vec{v})\right]\right)\\ &\quad +\frac{1}{r}\frac{\partial}{\partial r}\left[r\eta\left(\frac{\partial v_z}{\partial r}+\frac{\partial v_r}{\partial z}\right)\right]+F_z\end{aligned} \tag{2}$$

and in the radial direction it becomes:

$$\begin{aligned}\frac{\partial}{\partial t}(\rho v_r)+\frac{1}{r}\frac{\partial}{\partial z}(r\rho v_z v_r)+\frac{1}{r}\frac{\partial}{\partial r}(r\rho v_r v_r) &= -\frac{\partial p}{\partial r}+\frac{1}{r}\frac{\partial}{\partial z}\left(r\eta\left[\frac{\partial v_r}{\partial z}+\frac{\partial v_z}{\partial r}\right]\right)\\ &\quad +\frac{1}{r}\frac{\partial}{\partial r}\left(r\eta\left[2\frac{\partial v_r}{\partial r}-\frac{2}{3}(\nabla^*\cdot\vec{v})\right]\right)\\ &\quad -2\eta\frac{v_r}{r^2}+\frac{2}{3}\frac{\eta}{r}(\nabla^*\cdot\vec{v})+\rho\frac{v_\varphi^2}{r}+F_r\end{aligned} \tag{3}$$

with

$$\nabla^*\cdot\vec{v}=\frac{\partial v_z}{\partial z}+\frac{\partial v_r}{\partial r}+\frac{v_r}{r} \tag{4}$$

Here x is the axial coordinate, r is the radial coordinate, v_z is the axial velocity, v_r is the radial velocity, v_φ is the swirl velocity and η is the viscosity.

The equation for conservation of mass (also called continuity equation for mass-flow) can be written as follows:

$$\frac{\partial\rho}{\partial t}+\nabla\cdot(\rho\vec{v})=S_{mass} \tag{5}$$

which reduces for steady flow conditions to:

$$\nabla\cdot(\rho\vec{v})=S_{mass} \tag{6}$$

The source S_{mass} is the mass added to the continuous phase (gas) from a second dispersed phase (e.g., due to vaporization of liquid droplets). In the current study it is set to zero as we do not introduce any samples to the flow yet.

For the 2D-axisymmetric geometry the continuity equation then takes the form:

$$\frac{\partial}{\partial z}(\rho v_z) + \frac{\partial}{\partial r}(\rho v_r) + \frac{\rho v_r}{r} = S_{mass} \tag{7}$$

Finally, the energy equation has the form:

$$\frac{\partial}{\partial t}(\rho E) + \nabla \cdot (\vec{v}(\rho E + p)) = \nabla \cdot (\kappa_{eff} \nabla T - \sum_k h_k \vec{J}_k + (\bar{\tau}_{eff} \vec{v})) + S_h \tag{8}$$

Here κ_{eff} is the effective thermal conductivity, h_k is the enthalpy of the different species k, J_k is the diffusion flux of species k and $\bar{\tau}_{eff}$ is the effective stress tensor. In fact, the first three terms on the right hand side are the contribution from species thermal conductivity, diffusion and viscosity, respectively. Two source terms (S_h) are added to the energy equation: the coupled electric power density and the energy loss by emitted radiation (see section 2.4.2).

Furthermore, the energy is defined as:

$$E = h - \frac{p}{\rho} + \frac{v^2}{2} \tag{9}$$

with the enthalpy h calculated as:

$$h = \sum_k Y_k h_k \tag{10}$$

where Y_k is the mass fraction and h_k the enthalpy of the different species k. The enthalpies h_k are calculated from:

$$h_k = \int_{T_{ref}}^{T} c_{pk} dT \tag{11}$$

with the reference temperature $T_{ref} = 298.15K$. c_{pk} is the heat capacity of species k .

Note that in principle also the energy sources due to chemical reactions can be included:

$$S_{h,react} = -\sum_k \frac{h_{0k}}{M_k} R_k \tag{12}$$

where h_{0k} is the enthalpy of formation of species k and R_k is the volumetric creation rate of species k . However, because the sample introduction is not yet included in the model, this energy source term due to chemical reactions does not apply in the current work.

2.2.2. Species transport

The local mass fraction of a species k (Y_k) is predicted from the following transport-diffusion equation:

$$\frac{\partial}{\partial t}(\rho Y_k) + \nabla \cdot (\rho \vec{v} Y_k) = -\nabla \cdot \vec{J}_k \tag{13}$$

where J_k is the diffusion flux of species k . For steady state conditions the first term at the left hand side in the above equation is neglected. Finally, the diffusion flux J_k is given for laminar flows by:

$$\vec{J}_k = -\rho D_{k,m} \nabla Y_k - D_{k,T} \frac{\nabla T}{T} \tag{14}$$

where $D_{k,m}$ is the mass diffusion coefficient and $D_{k,T}$ is the thermal diffusion coefficient.

2.3. Electro-magnetic field

2.3.1. Solving the electric field

The electric field can be calculated in Fluent as a user defined scalar (UDS). There is a defined equation for any scalar variable in FLUENT in the form:

$$\frac{\partial}{\partial t}\rho\Psi + \nabla\cdot(\rho\vec{u}\Psi) = \nabla\cdot(D\nabla\Psi) + S \tag{15}$$

Ψ is the scalar variable to be calculated. The first term on the left hand side is the unsteady term (which only needs to be included if the FLUENT calculation is unsteady, and in our study it is neglected), the second term on the left hand side is the flux term, D is the diffusivity, and S is a source term. In order to use this equation for solving the electric field, we have to re-write the electric field related equation in the format of this equation. In fact each component of the electric field, i.e., sine and cosine parts, need to be considered as a separate Ψ, to be written in the format of equation (15), and then calculated separately. The steps to re-write the electric field equation will be presented in the following.

We start with the following Maxwell-equations:

$$\nabla\cdot\vec{D} = \rho_e \tag{16}$$

$$\nabla\times\vec{E} = -\frac{\partial}{\partial t}\vec{B} \tag{17}$$

$$\nabla\cdot\vec{B} = 0 \tag{18}$$

$$\nabla\times\vec{H} = \vec{j}_{ext} + \vec{j}_{ind} - \frac{\partial}{\partial t}\vec{D} \tag{19}$$

$\vec{E}$ is the electric field, $\vec{D}$ is the electric displacement field , $\vec{B}$ is the magnetic field, $\vec{H}$ is the magnetic field strength, ρ_e is the charge density, $\vec{j}_{ext}$ is the external current, $\vec{j}_{ind}$ is the induced current by the electric field and the last term in the right hand side of equation (19) is the displacement current. We can rewrite the equations (16-17) by applying the general expressions for isotropic conditions:

$$\vec{D} = \varepsilon\varepsilon_0\vec{E} \tag{20}$$

$$\vec{B} = \mu\mu_0\vec{H} \tag{21}$$

and Ohm's law:

$$\vec{j}_{ind} = \sigma\vec{E} \tag{22}$$

where ε is the permittivity , μ the permeability and σ the electrical conductivity. The zero indices indicate the values for vacuum. Furthermore, we can assume that $\mu = 1$ and ε and σ are constant in time. Note that for the latter assumption (time independent electrical conductivity) it is sufficient that a temporal change is slow compared to the oscillation time of the electro-magnetic fields. Therefore, the Maxwell equations can be simplified in the following way:

$$\nabla \cdot \varepsilon\vec{E} = 0 \tag{23}$$

$$\nabla \times \vec{E} = -\frac{\partial}{\partial t}\vec{B} \tag{24}$$

$$\nabla \cdot \vec{B} = 0 \tag{25}$$

$$\nabla \times \vec{B} = \mu_0(\vec{j}_{ext} + \sigma\vec{E}) + \frac{\varepsilon}{c^2}\frac{\partial}{\partial t}\vec{E} \tag{26}$$

Equation (23) is the so called neutrality equation. By applying a rotation on both sides of equation (24) and filling in equation (26) we have:

$$\nabla \times \left(\nabla \times \vec{E}\right) = \nabla \times \left(-\frac{\partial}{\partial t}\vec{B}\right) = -\frac{\partial}{\partial t}\left(\mu_0(\vec{j}_{ext} + \sigma\vec{E}) + \frac{\varepsilon}{c^2}\frac{\partial}{\partial t}\vec{E}\right) \tag{27}$$

The Laplace operator is defined in the form:

$$\nabla^2\vec{A} = \nabla\left(\nabla \cdot \vec{A}\right) - \nabla \times \left(\nabla \times \vec{A}\right) \tag{28}$$

And therefore:

$$\nabla \times \left(\nabla \times \vec{A}\right) = \nabla\left(\nabla \cdot \vec{A}\right) - \nabla^2 \vec{A} \tag{29}$$

Combined with the assumptions for μ, ε and σ from above, equation (27) takes the form:

$$\nabla\left(\nabla \cdot \vec{E}\right) - \nabla^2 \vec{E} = -\left(\mu_0 \frac{\partial}{\partial t} \vec{j}_{ext} + \mu_0 \sigma \frac{\partial}{\partial t} \vec{E} + \frac{\varepsilon}{c^2} \frac{\partial^2}{\partial t^2} \vec{E} \right) \tag{30}$$

Neglecting the displacement current (i.e., the last right term in equation (30)) and taking $\nabla \cdot \vec{E} = 0$, we obtain:

$$\nabla^2 \vec{E} = \left(\mu_0 \frac{\partial}{\partial t} \vec{j}_{ext} + \mu_0 \sigma \frac{\partial}{\partial t} \vec{E} \right) \tag{31}$$

To solve the latter equation we assume that the external current density has a sine time dependence:

$$\vec{j}_{ext}(t) = \vec{j}_{ext} \sin \omega t \tag{32}$$

And the temporal dependence of the electrical field can be split into a $\cos \omega t$ and $\sin \omega t$ part:

$$\vec{E}(t) = \vec{E}_1 \cos \omega t + \vec{E}_2 \sin \omega t \tag{33}$$

These parts can be solved independently from each other.

Figure 2.2 shows the direction of the coil current, magnetic and electric fields. Assuming that the magnetic field inside the torch is as shown in Figure 2.2.b, we can define that the electric field only goes into the φ direction. Therefore, we only have to look at one spatial component of the electric field:

$$\nabla^2 E_\varphi = \mu_0 \frac{\partial}{\partial t} j_{ext,\varphi} + \mu_0 \sigma \frac{\partial}{\partial t} E_\varphi \tag{34}$$

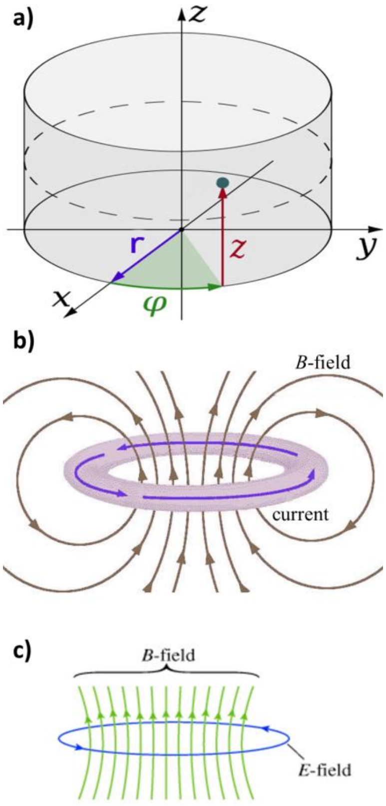

Figure 2.2: Schematic picture of the cylindrical coordinates (a), the spatial direction of the magnetic field and coil current (b), and the spatial direction of the magnetic and electric field inside the torch (c).

Splitting up the electric field into a cosine and a sine part, one can solve each part independently:

$$\nabla^2 E_{1\varphi} = \mu_0 \omega \; j_{ext,\varphi} + \mu_0 \sigma \omega \; E_{2\varphi} \tag{35}$$

$$\nabla^2 E_{2\varphi} = -\mu_0 \sigma \omega \; E_{1\varphi} \tag{36}$$

The Laplace operator of vectors in cylindrical coordinates has the form:

$$\nabla^2\vec{A}=\left(\frac{\partial^2 A_r}{\partial r^2}+\frac{1}{r^2}\frac{\partial^2 A_r}{\partial\varphi^2}+\frac{\partial^2 A_r}{\partial z^2}+\frac{1}{r}\frac{\partial A_r}{\partial r}-\frac{2}{r^2}\frac{\partial A_\varphi}{\partial\varphi}-\frac{A_r}{r^2}\right)\vec{e}_r$$
$$+\left(\frac{\partial^2 A_\varphi}{\partial r^2}+\frac{1}{r^2}\frac{\partial^2 A_\varphi}{\partial\varphi^2}+\frac{\partial^2 A_r}{\partial z^2}+\frac{1}{r}\frac{\partial A_\varphi}{\partial r}+\frac{2}{r^2}\frac{\partial A_r}{\partial\varphi}-\frac{A_\varphi}{r^2}\right)\vec{e}_\varphi \quad (37)$$
$$+\left(\frac{\partial^2 A_z}{\partial z^2}+\frac{1}{r^2}\frac{\partial^2 A_z}{\partial\varphi^2}+\frac{\partial^2 A_z}{\partial r^2}+\frac{1}{r}\frac{\partial A_z}{\partial r}\right)\vec{e}_z$$

where $\vec{e}_r$, $\vec{e}_\varphi$ and $\vec{e}_z$ are the eigenvectors in three directions of the cylindrical coordinate r , φ and z (see Figure 2.2). The last terms in both the r and φ directions are the extra terms which appear when the Laplace operator is applied on a vector in "cylindrical coordinates" ($-\frac{A_r}{r^2}$ and $-\frac{A_\varphi}{r^2}$).

Therefore, equation (35) and (36) can be written in the following form:

$$\nabla^2 E_{1\varphi}=\mu_0\omega\ j_{ext,\varphi}+\mu_0\sigma\omega\ E_{2\varphi}+\frac{E_{1\varphi}}{r^2} \quad (38)$$

$$\nabla^2 E_{2\varphi}=-\mu_0\sigma\omega\ E_{1\varphi}+\frac{E_{2\varphi}}{r^2} \quad (39)$$

If the used assumptions (i.e., $\frac{\partial}{\partial t}\Psi=0,\ \nabla\cdot(\rho\vec{u}\Psi)=0$) are applied to the UDS equation of FLUENT (see equation (15) above), it yields:

$$0=D\nabla^2\Psi+S \quad (40)$$

If equations (38) and (39) are written in the following form:

$$0=-\nabla^2 E_{1\varphi}+\mu_0\omega\ j_{ext,\varphi}+\mu_0\sigma\omega\ E_{2\varphi}+\frac{E_{1\varphi}}{r^2} \quad (41)$$

$$0=-\nabla^2 E_{2\varphi}-\mu_0\sigma\omega\ E_{1\varphi}+\frac{E_{2\varphi}}{r^2} \quad (42)$$

they are in the same form as the UDS equation (equation (40)) and we can define the electric field as a UDS in FLUENT. One can see that the UDS diffusivity (parameter D in equation (40)) becomes -1 in the electric field equations (equations (41) and (42)). The terms on the right hand sides (except the first ones) all will be treated as the source term (S) in equation (40).

2.3.2. Calculation of the magnetic field

The magnetic field can be calculated from the electric field via the Maxwell equations. The time dependence of the magnetic field is given by

$$\vec{B}(t) = \vec{B}_1 \cos \omega t + \vec{B}_2 \sin \omega t \tag{43}$$

Assuming that the electric field acts only in the φ direction, the magnetic field in cylindrical coordinates becomes (see Figure 2.2):

$$-B_{1r}(-\omega \sin \omega t) = -\frac{\partial E_{2\varphi}}{\partial z} \sin \omega t \tag{44}$$

$$-B_{1z}(-\omega \sin \omega t) = \left(\frac{E_{2\varphi}}{r} + \frac{\partial E_{2\varphi}}{\partial r} \right) \sin \omega t \tag{45}$$

$$-B_{2r}(-\omega \cos \omega t) = -\frac{\partial E_{1\varphi}}{\partial z} \cos \omega t \tag{46}$$

$$-B_{2z}(-\omega \cos \omega t) = \left(\frac{E_{1\varphi}}{r} + \frac{\partial E_{1\varphi}}{\partial r} \right) \cos \omega t \tag{47}$$

and consequently, the amplitudes of the magnetic field can be calculated from:

$$B_{1r} = -\frac{1}{\omega}\frac{\partial E_{2\varphi}}{\partial z} \tag{48}$$

$$B_{1z} = \frac{1}{\omega}\left(\frac{E_{2\varphi}}{r} + \frac{\partial E_{2\varphi}}{\partial r}\right) \quad 49)$$

$$B_{2r} = +\frac{1}{\omega}\frac{\partial E_{1\varphi}}{\partial z} \tag{50}$$

$$B_{2z} = -\frac{1}{\omega}\left(\frac{E_{1\varphi}}{r} + \frac{\partial E_{1\varphi}}{\partial r}\right) \tag{51}$$

2.4. Sources terms

As mentioned in section 2.2.1 above, in the momentum equation, the Lorentz force acts as a source. Furthermore, two source terms are added to the energy equation, i.e., the coupled electric power density and the energy loss by emitted radiation.

2.4.1. Source term for the momentum equation

The source term taken into account for the momentum equation (equations (2) and (3) in section 2.2.1 above) is defined by the Lorentz force. The Lorentz-force density (i.e., per unit volume) is given in Cartesian coordinates by:

$$\vec{F}_L = \vec{j} \times \vec{B} = \sigma \vec{E} \times \vec{B} = \sigma \begin{pmatrix} E_x \\ E_y \\ E_z \end{pmatrix} \times \begin{pmatrix} B_x \\ B_y \\ B_z \end{pmatrix} = \sigma \begin{pmatrix} E_y B_z - E_z B_y \\ -E_x B_z + E_z B_x \\ E_x B_y - E_y B_x \end{pmatrix} \tag{52}$$

When the electric field acts only in the φ direction and the magnetic field only in the radial (r) and axial (z) direction, one has the following expressions:

$$E_x = -E_\varphi \sin\varphi \tag{53}$$

$$E_y = E_\varphi \cos\varphi \tag{54}$$

$$E_z = 0 \tag{55}$$

$$B_x = B_r \cos\varphi \tag{56}$$

$$B_y = B_r \sin\varphi \tag{57}$$

$$B_z = B_z \tag{58}$$

Hence the Lorentz-force density becomes as follows:

$$\begin{aligned}\vec{F}_L &= \sigma\begin{pmatrix} E_\varphi \cos\varphi \cdot B_z \\ E_\varphi \sin\varphi \cdot B_z \\ -E_\varphi \sin\varphi \cdot B_r \sin\varphi - E_\varphi \cos\varphi \cdot B_r \cos\varphi \end{pmatrix} \\ &= \sigma\left[E_\varphi B_z \begin{pmatrix}\cos\varphi \\ \sin\varphi \\ 0\end{pmatrix} + (-E_\varphi B_r)\begin{pmatrix}0\\0\\1\end{pmatrix}\right] \\ &= (\sigma E_\varphi B_z)\vec{e}_r + (-\sigma E_\varphi B_r)\vec{e}_z\end{aligned} \tag{59}$$

Furthermore, adding the time-dependences of the electric and magnetic fields, we obtain:

$$\begin{aligned}\vec{F}_L &= (\sigma(E_{1\varphi}\cos\omega t + E_{2\varphi}\sin\omega t)(B_{1z}\cos\omega t + B_{2z}\sin\omega t))\vec{e}_r \\ &+ (-\sigma(E_{1\varphi}\cos\omega t + E_{2\varphi}\sin\omega t)(B_{1r}\cos\omega t + B_{2r}\sin\omega t))\vec{e}_z\end{aligned} \tag{60}$$

Averaging over one oscillation period, this yields:

$$<\vec{F}_L>=\frac{1}{2}\sigma(E_{1\varphi}B_{1z} + E_{2\varphi}B_{2z})\vec{e}_r + \frac{1}{2}(-\sigma E_{1\varphi}B_{1r} + E_{2\varphi}B_{2r})\vec{e}_z \tag{61}$$

Hence, these two components of the Lorentz force will be used in the two momentum equations (in the radial and axial direction, respectively).

2.4.2. Source terms for the energy equation

(a) Power coupling by the electrical field

The power density P introduced into the plasma is given by

$$\mathrm{P} = \vec{j}\cdot\vec{E} \tag{62}$$

with the current density $\vec{j}$. Assuming Ohm's law in simple form we have

$$\vec{j} = \sigma \vec{E} \tag{63}$$

where σ is the electrical conductivity. Hence, the power density can be written as

$$\mathrm{P} = \sigma \vec{E}^2 \tag{64}$$

The electric field oscillates with a frequency ω and has a time period of $\frac{2\pi}{\omega}$. As our calculations apply to much longer time scales compared to the oscillation period (i.e., timescales $>> \frac{2\pi}{\omega}$) it is appropriate to calculate a time-average (over one period) for the power density.

$$< \mathrm{P} >= \frac{\omega}{2\pi} \int_0^{2\pi/\omega} dt \sigma \vec{E}^2 \tag{65}$$

It is assumed that the electrical conductivity does not change significantly during one period. Consequently, it is set constant in time. Furthermore, the electric field can be split up into a cosine and a sine part. This yields:

$$< \mathrm{P} >= \sigma \frac{\omega}{2\pi} \int_0^{2\pi/\omega} dt (E_1{}^2 \cos^2 \omega t + E_2{}^2 \sin^2 \omega t + 2 E_1 E_2 \cos \omega t \sin \omega t) \tag{66}$$

The integration over $\cos^2$ and $\sin^2$ gives π and over $\cos \cdot \sin$ gives 0. As a result one has:

$$< \mathrm{P} >= \frac{1}{2} \sigma (E_1{}^2 + E_2{}^2) \tag{67}$$

Note that E_1 is the amplitude of the cosine part and E_2 is the amplitude of the sine part of the electric field.

Within FLUENT, the coupled power needs to be adapted during the simulations. The total power introduced, as calculated from the electric field in the way explained above, should not exceed the input power value, but it may be lower. Indeed, the generator will not deliver more power, but it is well possible that less power is coupled into the plasma. The total coupled power can be calculated by:

$$P_{total} = \int dV < \mathrm{P} > \qquad (68)$$

where V is the volume into which the power is coupled. As mentioned, the power density is proportional to the square of the electrical field (equation (64)), which itself is proportional to the external current. Hence, the current can basically be adapted by:

$$I = I_{old}\sqrt{\frac{P_{goal}}{P_{total}}} \qquad (69)$$

One needs to make sure that the new power does not exceed the input power (due to the changed conductivity conditions). This can be achieved by a test loop. Indeed, in case the total coupled power becomes higher than the input power or lower than 80% of the input power, the loop to update the current, electric field and coupled power is repeated until the total coupled power is in the acceptable range. As soon as that is achieved, the later updates for the current and the electric field can be used for calculating the magnetic field and the rest of the calculations. If after a specific number of loops (=10), the acceptable value for the power is not achieved, which happens for powers below 80% of the input power, then the loop stops and works with the lower power. In the next iterations, the updated power will gradually reach the value of 80% of the input power. Furthermore, also the current is controlled not to exceed the defined maximum (= 1000 A) and minimum (= 0) values by setting it to the maximum/minimum value if it reaches a value higher than the maximum or lower than the minimum.

(b) Radiation

Emitted radiation, as mentioned, is treated as a loss term in the energy conservation equation (equation (8) of section 2.1.1 above). We used the provided equation by [183] for the emitted radiation. Wilbers et al. have calculated the total radiative loss in an argon plasma at wavelengths from $100\ nm$ to $100\ \mu m$ (zero absorption) as a function of temperature (3000-15000K) in a wide pressure range (10^{-1}-10^{6} Pa) under LTE and non-LTE conditions. Under LTE conditions, as we assumed for this work, the plasma is optically thin, so that no absorption or scattering inside the plasma was taken into account. The radiative loss at 1×10^{5} Pa as a function of temperature for six different values of $\frac{T_h}{T_e}$ (i.e. 0.1, 0.2, 0.4, 0.6, 0.8 and 1) was plotted in Figure 2 in [183]. T_h and T_e are the temperature of heavy particles and electrons, respectively. The authors showed that when the calculated total radiative loss curves are divided by the square of electron density, the differences between the curves decrease strongly and vanish completely above 6000K (see Figure 3 in [183]). The influences of pressure and deviation from LTE on these curves are small and in many cases negligible. Indeed, almost all influences of pressure and deviation from equilibrim are incorporated in the electron density. Radiation to the argon ground level is not taken into account because most of this radiation does not escape the plasma [183]. In this reference, the radiation energy loss due to continuum (Bremsstrahlung) and line radiation (spectrum) in the wavelength range from 100 nm to 100 µm is calculated. The continuum emissivity consists of the free-bound and free-free emissivities. It is indicated in [184] that the main contribution of energy loss is due to continuum radiation, namely free-free and free-bound transitions of the electrons. A numerical fit to the curves corresponding to the condition of $T_h = T_e$ represents a simple expression for the calculation of the radiative loss as a function of temperature that is independent of small deviations from LTE:

$$\frac{Q_{total}}{n_e^2} = (C_1 + C_2 / T^{1/2} + C_3 / T + C_4 T + C_5 T^{3/2}) \exp\left(C_6 / T\right) \tag{70}$$

The parameter n_e is the electron density, T is the temperature in Kelvin, $C_1 = -6.932 \cdot 10^{-41}$ is the electron-ion continuum constant and $C_2 = 4.753 \cdot 10^{-39}$ is the electron-neutral continuum constant. The other fitted numerical constants are $C_3 = -5.808 \cdot 10^{-38}$, $C_4 = -2.843 \cdot 10^{-45}$, $C_5 = 8.629 \cdot 10^{-47}$, and $C_6 = 6.706 \cdot 10^{4}$. By using equation (70) the problem is reduced to the fact that we only need to know the electron density to determine the radiative power [183].

2.5. Ionization

As mentioned above, we assume that the ICP is in local thermodynamic equilibrium (LTE). Therefore, the electron and ion densities are determined from the Saha-Eggert equation [31];

$$\frac{n_e n_{kZ}}{n_{k(Z-1)}} = 2\frac{\zeta_{kZ}}{\zeta_{k(Z-1)}}\left(\frac{2\pi m_e k_B T}{h^2}\right)^{3/2} \exp\left(-\frac{E_{ion,kZ} - \Delta E_{ion,kZ}}{k_B T}\right) \tag{71}$$

where n_e is the electron number density, n_{kZ} is the number density of element (or molecule) k in the ionization stage Z, ζ is the partition function, E_{ion} is the ionization potential and ΔE_{ion} is the reduction of the ionization potential. k_B , T and h are the Boltzmann constant, the temperature and Plank constant, respectively. The partition functions of argon are calculated according to the functions given in [185]. For temperatures below 1000 K, the value is kept the same as for 1000 K which has no influence since the amount of ionization is negligible in that temperature range. The heavy species taken into account in the calculations are Ar, Ar^+ and Ar^{2+}. In fact, the Saha-Eggert equation describes the degree of ionization in the plasma as a function of the temperature, density, and ionization energies of the atoms. In a plasma of finite density the potential distribution in and near a given ion is influenced not only by its own bound electrons (E_{ion}) but also by free electrons, the neighboring ions and to a lower extent by the neutral atoms. This perturbation effect (ΔE_{ion}) is to alter the set of energy levels available to the ion in question. This effectively lowers all the ionization potentials and shifts the equilibrium occupation numbers in the direction of increased ionization. This effect is usually called “pressure ionization” [186].

Another equation to be taken into account is the conservation equation for the number densities of the heavy particles for each element:

$$n_{Hk} = n_{k0} + \sum_{Z=1}^{Z_{\max k}} n_{kZ} \tag{72}$$

where $Z_{\max}$ is the maximum ionization stage of element k. The sum of all heavy particle number densities n_{Hk} gives the total heavy particle number density n_{Htot}:

$$n_{Htot} = \sum_k n_{Hk} \tag{73}$$

Furthermore, the quasi-neutrality equation must be fulfilled:

$$n_e = \sum_k \sum_{Z=1}^{Z_{\max k}} Z n_{kZ} \tag{74}$$

This means that the electron fraction should be equal to the sum of all ion fractions, weighted according to their charge. For the following, it is assumed that the total number densities of the elements n_{Hk} and the temperature T are known. Therefore, n_{Htot} is then directly known as well from equation (73). We introduce a variable for the average charge stage Z_{av} as done in [187], in the form:

$$Z_{av} = \frac{n_e}{n_{Htot}} \tag{75}$$

This means that the electron density can be written as the product of the average ionization degree Z_{av} and n_{Htot}.

The fractions for the heavy particles are again defined as follows:

$$x_{kZ} = \frac{n_{kZ}}{n_{Hk}} \tag{76}$$

$$x_{Hk} = \frac{n_{Hk}}{n_{Htot}} \tag{77}$$

Hence, x_{kZ} is the fraction of species k in ionization state Z and x_{Hk} is the total fraction of species k.

We can call the right hand side of the Saha-Eggert equation (equation (71)) K_{kZ} :

$$\frac{n_e n_{kZ}}{n_{k(Z-1)}} = \mathrm{K}_{kZ} \tag{78}$$

By dividing the numerator and denominator of the left hand side by n_{Hk}, and replacing the electron density by $Z_{av}n_{Htot}$ we have:

$$\frac{Z_{av}n_{Htot}x_{kZ}}{x_{k(Z-1)}} = \mathrm{K}_{kZ} \tag{79}$$

and thus:

$$x_{kZ} = \frac{x_{k(Z-1)}}{Z_{av}n_{Htot}}\mathrm{K}_{kZ} = x_{k0}\,\frac{\prod_{j=1}^{Z}\mathrm{K}_{kj}}{(Z_{av}n_{Htot})^{Z}} \tag{80}$$

By dividing both sides of the conservation equation for the number densities of the heavy particles (equation (72)) by n_{Hk} we obtain:

$$1 = x_{k0} + \sum_{Z=1}^{Z_{\max}} x_{kZ} \tag{81}$$

and

$$1 = x_{k0} + \sum_{Z=1}^{Z_{\max}} x_{k0}\,\frac{\prod_{j=1}^{Z}\mathrm{K}_{kj}}{(Z_{av}n_{Htot})^{Z}} \tag{82}$$

In which x_{kZ} is replaced from equation (80) and gives x_{k0} as follows:

$$x_{k0} = \frac{1}{1 + \sum_{Z=1}^{Z_{\max k}} Z\,\frac{\prod_{j=1}^{Z}\mathrm{K}_{kj}}{(Z_{av}n_{Htot})^{Z}}} \tag{83}$$

Additionally, we can write the average ionization degree as follows:

$$Z_{av} = \frac{\sum_k \sum_{Z=1}^{Z_{\max k}} Z n_{kZ}}{n_{Htot}} = \frac{\sum_k \sum_{Z=1}^{Z_{\max k}} Z x_{kZ}}{\frac{1}{x_{Hk}}} = \sum_k x_{Hk} \sum_{Z=1}^{Z_{\max k}} Z x_{kZ} \tag{84}$$

By replacing x_{kZ} and x_{k0} from equations (80) and (83), we obtain:

$$\begin{aligned} Z_{av} &= \sum_k x_{Hk} x_{k0} \sum_{Z=1}^{Z_{\max k}} Z \frac{\prod_{j=1}^{Z} \mathrm{K}_{kj}}{(Z_{av} n_{Htot})^Z} \\ &= \sum_k x_{Hk} \frac{\sum_{Z=1}^{Z_{\max k}} Z \frac{\prod_{j=1}^{Z} \mathrm{K}_{kj}}{(Z_{av} n_{Htot})^Z}}{1 + \sum_{Z=1}^{Z_{\max k}} Z \frac{\prod_{j=1}^{Z} \mathrm{K}_{kj}}{(Z_{av} n_{Htot})^Z}} \end{aligned} \tag{85}$$

The average charge stage Z_{av} can now be calculated from the transcendental equation (85) (e.g. by the Newton method) without the necessity to solve the equation for the heavy particle fractions at the same time. The derivation to calculate the average ionization degree, Z_{av}, follows basically the derivation given in [188], except that the "heavy particle fractions" are inserted into the neutrality equation for more than one element. In this way, only one equation needs to be solved for any number of elements and any number of ionization stages, as is also presented in [188]. When Z_{av} is known, the proportions of the heavy particles can subsequently be calculated from equations (80) and (83).

The ionization potential reduction that appeared in the Saha-Eggert equation is calculated from [189]

$$\Delta E_{ion} = \frac{Ze^2}{4\pi\varepsilon_0(\lambda_D + \lambda_B/8)} \tag{86}$$

where λ_D is the Debye-length, calculated as:

$$\lambda_D = \sqrt{\frac{\varepsilon_0 k_B T}{e^2}\left(n_e + \sum_k \sum_{Z=1}^{Z_{\max k}} Z^2 n_{kZ}\right)} \tag{87}$$

and the de Broglie length λ_B is:

$$\lambda_B = \sqrt{\frac{h^2}{2\pi m_e k_B T}} \tag{88}$$

where ε_0 is the vacuum permittivity and h is the Plank constant.

2.6. Material Parameters

Several material parameters need to be defined in the model. In the following, the viscosity, thermal conductivity, heat capacity, diffusion and electrical conductivity will be explained.

2.6.1. Viscosity

The viscosity for a pure gas is given by [190]:

$$\eta = 0.5\sqrt{\frac{4k_B T}{(m/2)\pi}} \cdot m \cdot n \cdot l \tag{89}$$

where the square-root term is the thermal velocity, m is the (atomic) mass, l is the mean free path and n is the number density. One has to note that the mass contributing to the velocity is in principle the reduced mass ($\sqrt{m/2}$) to account for their relative velocity. This fact is especially important when looking at gas mixtures. The mean free path is usually taken as

$$l = \frac{1}{nS} \tag{90}$$

where S is the collision cross section. We only consider two-particle collisions. Thus, for each collision, different reduced masses need to be applied. In this sense, for multi-species collisions, the following transformation is to be applied:

$$\frac{\sqrt{m/2}}{l} \rightarrow \sum_i \sqrt{\frac{m_k m_i}{m_k + m_i}} n_i S_{ki} = \sum_i \sqrt{\mu_{ki}} n_i S_{ki} \tag{91}$$

Therefore, the viscosity of the mixture, η, is calculated from the generalization of the viscosity equation for pure elements:

$$\eta_{mixture} = \frac{1}{2}\sqrt{\frac{4k_B T}{\pi}} \left(\sum_k \frac{m_k n_k}{\sum_i \sqrt{\mu_{ki}} n_i S_{ki}} \right) = \eta_e + \sum_{k \neq e} \eta_k \tag{92}$$

where m_k and n_k are the mass and number density of the species k (heavy species and electrons) respectively and μ_{ki} is the reduced mass of the species k and i. η_e and η_k are the viscosities corresponding to electrons and heavy species. In fact, the square-root in the denominator originates from the different relative velocities of different species at the same temperature T. The viscosity of the electrons is also taken into account but it is effectively negligible due to the small mass of the electrons.

A simple approximation is used to calculate the cross-sections for neutral-neutral and neutral-charged collisions from the atomic (and ionic) radii as follows:

$$S_{ki} = \sqrt{2}\pi(R_{eff,k} + R_{eff.i})^2 \tag{93}$$

where the radius of electrons is neglected here. The temperature dependent diameters for helium and argon are calculated from the data given in [180-192]. The fit functions used during the calculation for argon and helium are given in Table 2.2. The collision cross-section for charged particles is taken as [193]:

$$S_{ki} = Z_k^2 Z_i^2 \cdot 3\pi b_0^2 \left(\ln \Lambda_C + \frac{1}{2} \ln\left(\frac{3\pi}{2} \right) \right) \tag{94}$$

where $\ln \Lambda_C = 12\pi\lambda_D^3 n_e$ is the Coulomb logarithm [194] and $b_0 = e^2 /(12\pi\varepsilon_0 k_B T)$ is the 90-degree collision parameter.

Table 2.2: Fit functions used for the calculation of the effective diameter of argon; the parameters are derived from viscosity data given in [190-192].

Element	Effective diameter[190]	Temperature range
Ar	$d = \frac{5.2603 \cdot 10^{-10}}{(T - 154.46485)^{0826}} - 7.0465 \cdot 10^{-16} \cdot T + 1.2167 \cdot 10^{-11}$	$273K < T < 9300K$
	$d = 3.3 \cdot 10^{-28} \cdot (T - 7700)^{4.7} + 2.5275 \cdot 10^{-10}$	$9300K < T < 12000K$
He	$d = \frac{9.5066 \cdot 10^{-6}}{(T + 1133.33407)^{1.66528}} - 2.6575 \cdot 10^{-15} \cdot T + 1.6499 \cdot 10^{-10}$	$273K < T < 11250K$

2.6.2. Thermal conductivity

The thermal conductivity for atomic elements is given by [193]:

$$\kappa = \frac{5}{2} \eta \, C_V \tag{95}$$

where η is the viscosity and C_V is the heat capacity at constant volume. If C_V is set equal to $\frac{3k_B}{2m}$ [195] then the thermal conductivity becomes:

$$\kappa = \frac{15 k_B \, \eta}{4m} \tag{96}$$

More in general, the thermal conductivity of a gas consisting of monoatomic species can be calculated from the viscosities of the electrons, η_e, and the various heavy species (atoms, ions), η_k, [195]

$$\kappa = \frac{15}{4} \frac{k_B}{m_e} \eta_e + \sum_k \sum_{Z_k} \frac{15}{4} \frac{k_B}{m_k} \eta_{k,Z_k} \tag{97}$$

where m_e and m_k are the masses of the electrons and atomic heavy species. The second term counts various elements in different ionization states (i.e., Ar^+ and Ar^{2+}

in the current work). In contrast to the viscosity, small masses have a strong influence on the thermal conductivity. Consequently, the first term, originating from the electrons, gives a strong contribution if a sufficient number of free electrons is present. Hence, it is better to determine the effective atomic radius from viscosity data rather than from thermal conductivity data, at least for higher temperatures. We assumed that the ionic radius for interactions with neutrals should not deviate too much from the atomic one. Therefore we use the same values for the ionic radius of Ar^{+} and Ar^{2+} as for the argon atomic radius.

2.6.3. Heat capacity

The (total mean) heat capacity consists of the standard gas heat capacity and some further terms:

$$c_p = c_{p,gas} + c_{p,exc} + c_{p,diss} + c_{p,e} + c_{p,ion} \tag{98}$$

The right hand side terms are the standard heat capacity of an ideal gas (first term), the heat capacity contribution from excitation of the bound electrons of the atoms (second term), dissociation of the molecules (third term), and ionization, which includes the contribution of free electrons (fourth term) and ions (last term).

The standard heat capacity at constant pressure $c_{p,gas}$ for ideal gases is given by:

$$c_{p,gas,k} = c_{V,k} + \frac{R}{M_k} \tag{99}$$

where $c_{V,k}$ is the heat capacity at constant volume of species k, R is the universal gas constant and M_k is the molar mass of species k. In this work we used the standard heat capacity tabulated in FLUENT for the first term. Because ionization is not available from FLUENT (and it is included as user defined function, see section 2.5 above), we added the contribution of ionization to the heat capacity separately. The second term is ignored in this work to simplify the calculations. However, we plan to add it to the model in our future work. The third term vanishes as we do not consider chemical reactions.

The heat capacity from ionization (free electrons and ions; last term) can be calculated from the derivative of enthalpy with respect to temperature:

$$c_{p,ionization} = \left.\frac{\partial H_{ionization}}{\partial T}\right|_{p} = c_{p,ion} + c_{p,e} \tag{100}$$

The enthalpy originating from ionization can be calculated from

$$H_{ionization} = \sum_{k} \frac{N_A}{M_{Htot}} x_{Hk} \sum_{Z=1}^{Z_{\max,k}} \left(\sum_{l=1}^{Z} E_{ion,kl}^{eff} \right) x_{kZ} + \frac{N_A}{M_{Htot}} Z_{av} \frac{5}{2} k_B T \tag{101}$$

$E_{ion,kl}^{eff}$ is the ionization potential of the ionization level l of element k ,corrected for the ionization potential reduction (see section 2.5). The first and second terms account for the heat capacity of ions, $c_{p,ion}$, and free electrons, $c_{p,e}$, respectively.

The total molar mass M_{Htot} is calculated from

$$M_{Htot} = \sum_{k} x_{Hk} M_{k} \tag{102}$$

where x_{Hk} are the molar fractions of the elements as we defined above:

$$x_{Hk} = \frac{n_{Hk}}{n_{Htot}} \tag{77}$$

where n_{Hk} is the number density of heavy species k and n_{Htot} is the total number density of heavy species. M_k is the molar mass of species k, N_A is Avogadro's constant and Z and Z_{av} are the charge number and average charge numbers, respectively. The FLUENT version used in this work, i.e., FLUENT v.13, only provides temperature and mass fractions of the elements for the calculation of c_p. Therefore, a constant heavy particle pressure of 101,225 Pa was assumed within the whole calculation region from which the total heavy particle number density and subsequently the c_p contribution of ionization was calculated.

2.6.4. Diffusion

The isotropic diffusion coefficients [195] for the various species k (i.e., atoms, ions, electrons) are taken into account in the present model by:

$$D_k = \frac{6}{5} \sum_{Z=1}^{Z_{\max,k}} x_{kZ} \sqrt{\frac{k_B T}{\pi}} \frac{1}{\sum_i \sqrt{\mu_{ki}} n_i S_{ki}} \tag{103}$$

where $x_{kZ} = n_{kZ} / n_{Hk}$, n_{kZ} is the heavy particle number density of species k in the ionization stage Z, μ_{ki} is the reduced mass for species k and species i, n_i is the number density of species i and S_{ki} is the collision cross-section for species k and species i. Note that ambipolar diffusion, which is only relevant for ionic species [196], is not applied in the present model. Indeed, the maximum ionization degree for the present conditions is less than 3%. The possible error from this effect on diffusion can hence be estimated to be below 3%. We expect that this error lies within the uncertainty of our model.

2.6.5. Electrical conductivity

The basic equation for electrical conductivity originating from the electrons is [193]:

$$\sigma_e = e n_e \frac{e}{m_e} \tau_e \tag{104}$$

where e is the elementary charge, m_e and n_e are the mass and number density of an electron, and τ_e is the collision time. A similar equation also holds for the heavy particles. The electrical conductivity for a mixture can then be determined from the contribution of electrons and heavy particles:

$$\sigma = \sum_k q_k n_k \frac{q_k}{m_k} \sqrt{\frac{\pi}{4k_B T}} \frac{1}{\sum_i \frac{n_i S_{ki}}{\sqrt{\mu_{ki}}}} \tag{105}$$

Where k counts for the electrons and the heavy particles, $q_k = eZ_k$ is the species charge, m_k and n_k are the mass and number density of the species k respectively and μ_{ki} is the reduced mass of the species k and i. S_{ki} for different collisions are the same as mentioned for the viscosity. We used a factor of 1.5 in equation (105) to fit the data for argon.

Chapter 3

Calculation strategy

To describe the ICP, we divide the whole simulation setup in three major steps, as outlined in this Chapter. The first step is the pre-processing step, which includes preparing the geometry and mesh, providing the needed physical equations or properties as user defined functions written in C, as well as defining user defined scalars and finally setting the boundary and initial conditions. The second step is solving the model and the third step does the post-processing, i.e., analyzing the results.

3.1. Pre-processing

3.1.1. Geometry and mesh generation

The required geometry for the model is made by the geometry and mesh generation software, called GAMBIT, which is also ANSYS software. This program is the pre-processor for the computational fluid dynamics (CFD) analysis. GAMBIT allows building 2D or 3D geometries, and it has a single interface for the geometry creation and the meshing that brings together several preprocessing technologies in one environment.

The geometry we made is shown in Figure 2.1 above. Any line shown in Figure 2.1 has to be specified as a "torch wall", "coil" or "sampler". A sampler is designed in the geometry which is set to a pressure outlet boundary condition in FLUENT. Because the area close to the sampler is the most interesting region to study, the created mesh close to the sampler is much finer than in the rest of the torch. For instance, the mesh defined for the region close to the sampler can reach a maximum size of 0.25 mm while in the region of the walls or the ambient gas this value can be as large as 2 mm. The calculation region extends further than only the inside of the torch, to enable a proper description of the entire gas flow dynamics, and to allow simpler boundary conditions for the model. Indeed, the electric fields, for instance, could be set to zero at the boundary without affecting the plasma behavior. This can be considered as the equivalent of the metal shielding box around the ICP, which prevents the rf radiation from entering the laboratory. The entire calculation region has a radius of 10 cm and an axial length of 15 cm (in the case without sampling cone) or 4.5 cm (in the case with sampling cone). The geometry is subdivided into about 23,000 (in the case without sampling cone) and 15,000 cells (in the case with sampling cone), of which about half are located inside the torch and in the region directly behind the torch and close to the sampler.

We define three "cell zones" as follows: the coil zone, torch zone and fluid zone (including the plasma flow and ambient gas flow).

After creation of the geometry and the mesh, the GAMBIT output files need to be loaded in FLUENT.

3.1.2. Physics, UDFs and UDSs

For modeling the gas flow dynamics we apply the Navier-Stokes equations coupled with the energy conservation equation from FLUENT [182], as explained in Chapter 2. The energy source (external power coupling) and loss (radiation) terms need to be written in a separate code (in C) and loaded as UDFs into FLUENT. The same applies to the component of the Lorentz force density as the source term for the momentum equation. Each component of the electric field is also loaded as a UDS into FLUENT. Moreover, some other self-written codes calculate the material parameters, i.e., viscosity, heat capacity, thermal and electrical conductivity and diffusion coefficients as a function of the actual gas composition and plasma temperature. Ionization is also taken into account by solving the Saha-Eggert equation for which again a UDF, defining the ion and electron density, needs to be loaded into FLUENT. Details about the applied equations are provided in Chapter 2.

3.1.3. Operating and boundary conditions

Once the geometry and separate code files (i.e., UDFs and UDSs) are loaded into FLUENT, we need to define the operating and boundary conditions. We assume that the gas flow is laminar and the system is in steady state. A solver called “pressure based” (see section 3.2.1 below) is chosen and the so-called “coupled algorithm” (see also section 3.2.1 below) is set for the calculations.

The properties of each torch, coil and fluid zone are defined as well as the amount of gas flow rate for each mass flow inlet (i.e., central, intermediate and outer inlets). Furthermore, the sampler is set as a pressure outlet. In the case of the presence of a sampler, as the pressure at both sides of the sampler has a huge difference, the calculation cannot start if we set the final values of the pressure at the beginning. In fact, we first need to calculate the flow continuity equation without any energy source to reach convergence for the calculation. Moreover, the pressure at both sides of the sampler should be set equal at the beginning (101225 Pa) and only after the first convergence, the pressure behind the sampler has to be lowered step by step (with intervals of 10000 Pa) and the calculations need to be repeated to reach convergence again until the value of 133.32 Pa (1 torr) is reached. This is the most time consuming part of setting up the model in FLUENT prior to beginning the calculation.

The operating and boundary conditions are different for the calculations presented in the following results chapters. Therefore, we will present in each chapter the conditions to which the model will be applied.

3.2. Solution procedure

In this section, first we describe in section 3.2.1 how the FLUENT solvers work in general, and subsequently we explain in section 3.2.2 the solution strategy of our ICP-MS model.

3.2.1. General FLUENT flow solvers

FLUENT provides two different numerical methods to solve the flow equations, i.e., a pressure-based solver and a density-based solver [182]. The pressure-based approach is developed for low-speed incompressible flows, while the density-based approach is mainly used for high-speed compressible flows. Using either method, FLUENT will solve the governing integral equations for the conservation of mass, momentum and energy, and some other scalars such as the magnetic fields in the present study. In both cases a control-volume-based technique is used that consists of:

- Division of the domain into discrete control volumes using a computational grid.
- Integration of the governing equations on the individual control volumes to construct algebraic equations for the discrete dependent variables (“unknowns”) such as velocities, pressure, temperature, and conserved scalars.
- Linearization of the discretized equations and solution of the resultant linear equation system to yield updated values of the dependent variables.

We applied the pressure-based solver in this study. In both methods the velocity is obtained from the momentum equation. In the pressure-based approach, the pressure equation is derived from the continuity and the momentum equations in such a way that the velocity, corrected by the pressure, satisfies the continuity. Since the governing equations are nonlinear and coupled to one another, the solution process involves iterations wherein the entire set of governing equations is solved repeatedly until the solution converges.

Two pressure-based solver algorithms are available in FLUENT, i.e., a so-called segregated algorithm and a coupled algorithm [182]. In the pressure-based segregated algorithm the governing equations are solved sequentially. This means that the individual governing equations for the solution variables are solved one after another. Each governing equation, while being solved, is "decoupled" or "segregated" from the other equations, hence its name. Because the governing equations are in fact non-linear and coupled, the solution loop must be carried out iteratively in order to obtain a converged numerical solution. The segregated algorithm is memory-efficient, since the discretized equations need only to be stored in the memory one at a time. However, the solution convergence is relatively slow, because the equations are solved in a decoupled manner [182].

With the segregated algorithm, each iteration consists of the steps illustrated in Figure 3.1 (left side). These steps are continued until the convergence criteria are met.

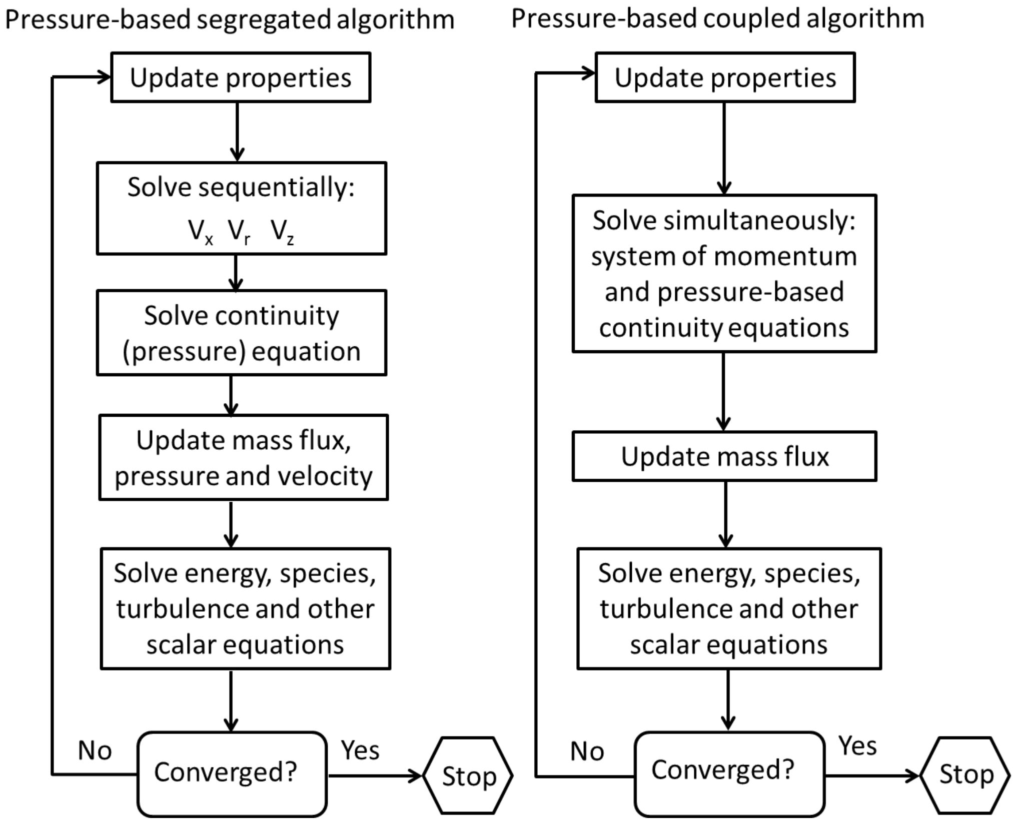

Figure 3.1: Overview of the pressure based segregated (left) and coupled (right) solution methods [182].

Unlike the segregated algorithm described above, the pressure-based coupled algorithm solves a coupled system of equations comprising the momentum equations and the pressure-based continuity equation. Since the momentum and continuity equations are solved in a closely coupled manner, the rate of solution convergence significantly improves when compared to the segregated algorithm. However, the memory requirement increases by 1.5 - 2 times compared to that of the segregated algorithm since the discrete system of all momentum and pressure-based continuity equations needs to be stored in the memory when solving for the velocity and pressure fields. The solution procedure of the pressure-based coupled algorithm is also explained in Figure 3.1 (right side).

3.2.2. Solving the ICP-MS model

Figure 3.2 summarizes the solution strategy of our model. As we explained the physics of each equation in Chapter 2 above, we show here only how and in which order the model works.

The ignition power creates a current density and an electric field. Subsequently, the magnetic field is calculated from the spatial derivative of the electric field. From the electro-magnetic fields, the Lorentz force density becomes available. Next, the three conservation equation of mass, momentum and energy are solved (including the source terms) and the electric field is calculated (as a UDS).This provides among others the gas flow velocities and the plasma temperature. Assuming LTE, we use the plasma temperature to solve the Saha-Eggert equation, which gives us the number density of ions and electrons. The transport parameters (i.e. electrical conductivity, viscosity, heat capacity, diffusion and thermal conductivity) are calculated based on the temperature and number density of the species. From the electric field and electrical conductivity, a new value for the power is reached for each cell. By integrating this power over the entire volume in which the power is coupled, we can calculate the total coupled power. At this point, it should be checked whether the total calculated power exceeds the input power or not. If yes, we need to update the current and the electric field, as indicated by the red circle in Figure 3.2, and this procedure needs to be repeated until the power becomes lower than or equal to the input power. Subsequently, the magnetic field can be updated as well as the rest of the equations.

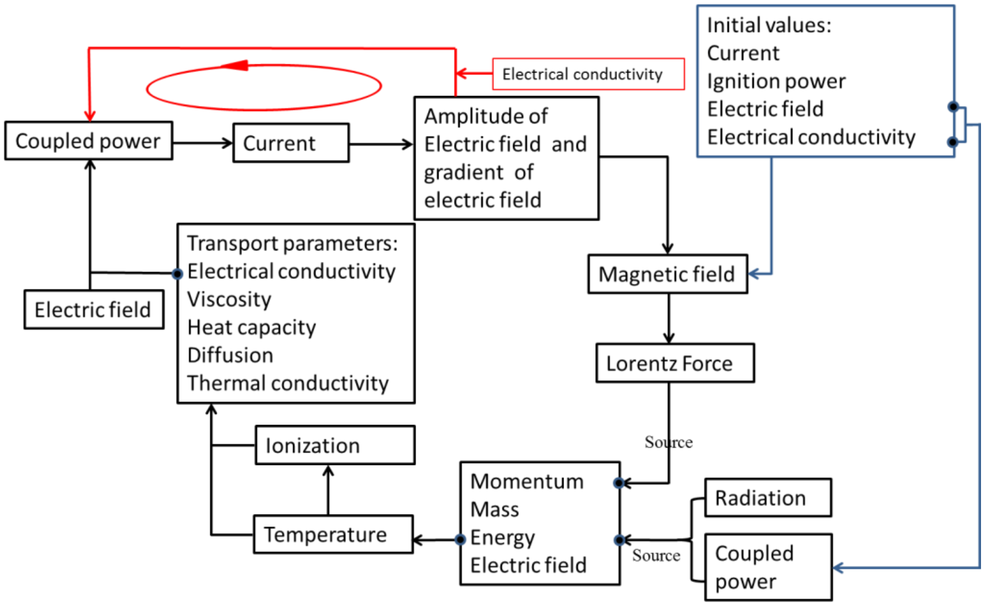

Figure 3.2: Solution strategy of the model.

Because of the nonlinearity of the equation set solved by FLUENT, it is necessary to control the change of a variable φ. This is typically achieved by under-relaxation of this variable (also referred to as explicit relaxation), which reduces the change of φ produced during each iteration. In a simple form, the new value of the variable, φ_{new}, within a cell depends upon the old value, φ_{old}, the computed change, $\varphi_{computed} - \varphi_{old}$ and the under-relaxation factor, $\overline{URF}$, as follows:

$$\varphi_{new} = \varphi_{old} + \overline{URF}(\varphi_{computed} - \varphi_{old}) \tag{106}$$

For example, to control the current changes in each iteration, an URF is introduced for I into the formula:

$$I = \overline{URF}\left(I_{old}\sqrt{\frac{P_{goal}}{P_{total}}} - I_{old} \right) + I_{old} \tag{107}$$

The fact that the current is variable in our calculations is physically reasonable since the coil is part of a resonant circuit where the current is not fixed.

3.3. Post-processing

When the calculation is converged, we can either make some plots in FLUENT or use the ANSYS CFD-post-software. The latter is a post-processor software to which we can export the data from FLUENT. It provides a user friendly interface to plot 2D or 3D contour plots, as well as stream lines of the gas flow, and XY diagrams, as will be presented in the coming chapters.

PART III: Results and Discussions

Chapter 4:

Coupling a mass spectrometer to the ICP torch

In this chapter, the effect of the presence of a sampler on the fundamental plasma characteristics in ICP-MS is computationally investigated. To investigate the effects of the sampler, two sets of calculations with exactly the same conditions, with and without the sampler, are performed. The details of the geometry and of preparing the calculations are discussed in Chapter 3. Typical plasma characteristics, such as gas flow velocity, plasma temperature and electron density, are calculated in two dimensions (cylindrical symmetry) and compared with and without a mass spectrometer sampling interface. The results indicate a dramatic increase in the plasma velocity in the region close to the interface. Furthermore, a cooled metal interface lowers the plasma temperature and electron density on the axial channel very close to the sampling cone but the corresponding values in the off axial regions are increased. Therefore, the effect of the interface strongly depends on the measurement position. It is shown that even a small shift from the actual position of the sampler leads to a considerable change of the results. The calculation results are compared with the measured data from [98,99,197], and provide a better insight in the underlying physics responsible for the effect of the sampling interface.

This chapter is based on the following publication: M. Aghaei, H. Lindner, A. Bogaerts, Effect of a mass spectrometer interface on inductively coupled plasma characteristics: A computational study, J. Anal. At. Spectrom. 27 (2012) 604-610.

4.1. Operating and geometrical conditions

The total power coupled to the plasma is set to 1000 W and the frequency of the harmonic external electric current density is 27 MHz. The injector gas flow rate is 1 L/min and the flow rate of the coolant and auxiliary gases are 12 L/min and 0.4 L/min, respectively. The ambient gas pressure and exhaust pressure are set to 101325 Pa and 101225 Pa, respectively. In the case with sampler, the pressure downstream of the sampler is set to 133.32 Pa. The schematic picture of the ICP geometry used in the simulations is shown in Figure 2.1. The diameters of the central torch inlet and sampler orifice are 1.5 mm and 1 mm respectively. The sampler position from the load coil is 10 mm.

4.2. Gas flow path lines and velocity

The gas flow path lines, originating from the central and outer inlets, colored by velocity in m/s, are plotted in Figure 4.1.a and 4.1.b, for the case without and with sampler, respectively. The path lines originating from the intermediate inlets are colored in black to be distinguishable from the injector and coolant gas, and for the sake of further discussions in section 4.3.

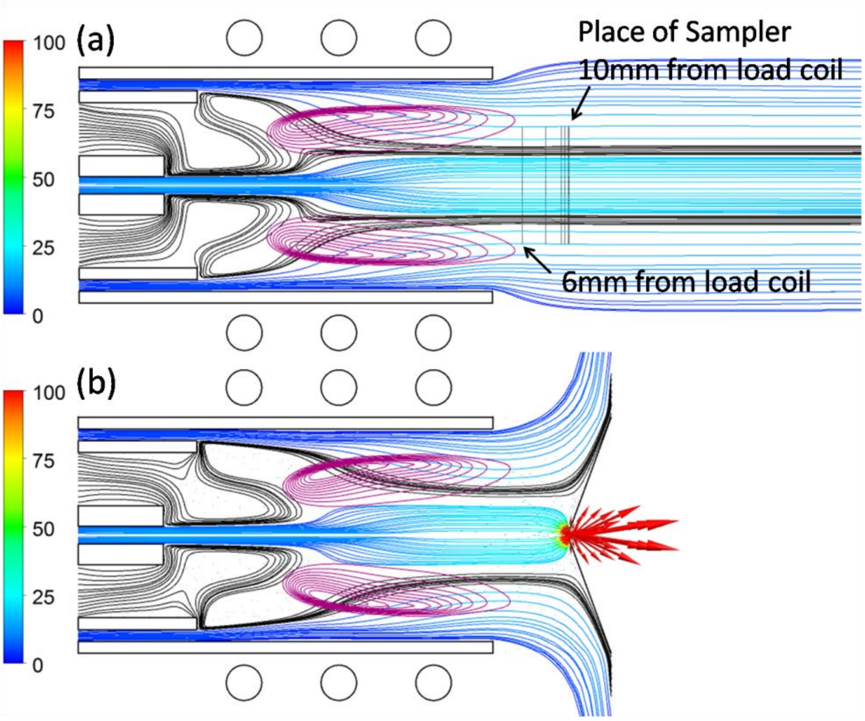

Figure 4.1: Effect of presence of sampler: 2D gas flow velocity path lines originating from the central and outer inlets, colored by velocity in m/s, and from the intermediate inlet, colored in black, (a) without and (b) with sampler. The thin vertical solid lines in (a) indicate the axial positions at which the radial profiles of Figure 4.4 and 4.7 are plotted, i.e., at 6mm, 8mm, 9.3mm, 9.6mm, 9.9mm, and 10mm from the load coil. Velocity vectors are also plotted in Figure (b), when the gas is flowing through the sampling orifice. The purple contours indicate the area of external power coupling.

It is seen in both figures that the flow coming from the central inlet, instead of maintaining a straight line trajectory, adopts a curved flow profile due to the entrainment forces acting upon it, as was predicted by Stewart et al. to be a likely scenario for off-axis sampling of an ion cloud (see Figure 8.c of reference [197]). This scenario was supported by experiments [197]. Nevertheless, in the case with sampler (Figure 4.1.b), as a consequence of flow acceleration to the orifice of the sampler, the whole injector gas flow is able to pass through the interface cone. However, the auxiliary and coolant gas flows are not affected by the acceleration process to the orifice, and they adopt a curved line trajectory to the open sides of the torch at the end sides of the interface cone. This modification of path lines affects the temperature and electron density profiles, which will be presented below.

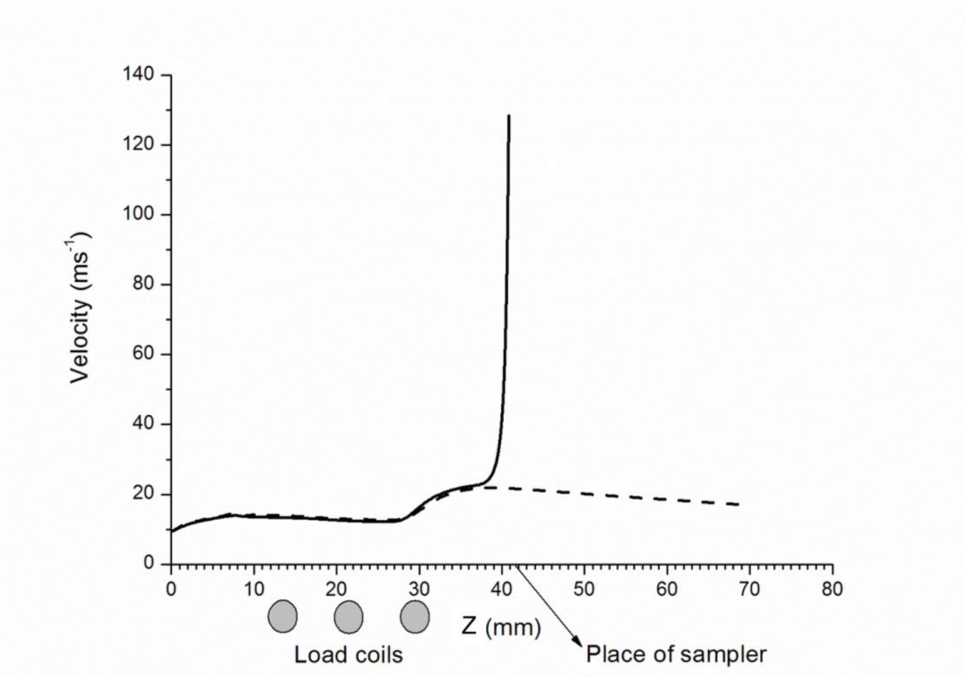

Figure 4.2: Effect of presence of sampler: Axial distribution of gas flow velocity (m/s) in the case with (solid line) and without (dashed line) sampler, on the central axis of the plasma torch. The load coils and the place of the sampler are also indicated in this figure, for clarity.

In addition, the graphs illustrate how the gas velocity in the area close to the sampler is changed by the presence of the sampler. Indeed, a large difference in pressures upstream and downstream of the sampler (i.e., 101191.68 Pa), considering Bernoulli's principle, causes an extreme increase in the velocity of the flowing plasma, as is illustrated in Figure 4.1.b by the red velocity vectors in m/s, added to better visualize this effect. The same effect is apparent from Figure 4.2, which shows the velocity on the central axis as a function of axial position. In both cases, i.e., with and without sampler, the velocity rises when the flow leaves the load coil (i.e., around 30 mm from the central inlet), because the gas is heated up by the power coupled into the plasma, which results in the increased velocity [181]. The effect of the sampler on the velocity is indicated by the solid line in Figure 4.2, which exhibits a sharp increase towards the sampler. Note that the solid line is plotted to 1 mm before the sampler, to fit in the y-scale of this figure, but the velocity increases further to about 500 m/s when it passes the sampler orifice. Ma et al. have also observed a similar rise in velocity due to the presence of the sampler, as reported in [98].

4.3. Plasma temperature

The plasma temperature is a fundamental property of the ICP. Indeed, temperature changes affect the plasma thermal conductivity. Moreover, the rate of droplet desolvation and particle vaporization is affected by the gas kinetic temperature [198]. Inserting a cooled metal sampler as an interface between ICP and mass spectrometer causes the following changes, as presented in Figure 4.3-4.7.

The 2D profiles of the plasma temperature are presented in Figure 4.3, both in the absence (Figure 4.3.a) and presence (Figure 4.3.b) of the mass spectrometer interface. It is shown that the off-axial region of the plasma has a higher temperature than the central region in both Figure 4.3.a and Figure 4.3.b, which indicates the presence of the central channel cooling the plasma. Furthermore, as the coolant gas has a strong flow rate, the gas layers next to the torch wall stay cool, as is also seen in Figure 4.3 in both cases. The hottest region in the radial direction is close to the middle of the intermediate inlet, which is the place of maximum power deposition (see purple contours in Figure 4.1 above). The absolute values of the calculated plasma temperature, i.e. 8000-9000 K above the load coil, are in good agreement with experiments [21,199].

Insertion of the sampler does not seem to affect the plasma temperature inside the load coil to a great extent. However, a small temperature rise can still be observed, attributed to the change in path lines in this region, as seen in Figure 4.1 above. Indeed, in the coil region, when the interface is inserted, the auxiliary flow (path lines colored in black in Figure 4.1) passes the area which is characterized by high electrical power deposition (i.e., the center of the purple contours in Figure 4.1.b), while in the case without sampler, part of the auxiliary flow passes through the area which has lower coupled power values (see Figure 4.1.a). The total external power and auxiliary mass flow rate are the same in both cases with and without sampler, but the flow seems to pass through more efficient areas to heat up, in the case of presence of the sampler. In other words, the auxiliary flow combines later with the injector flow, after passing through the high power area, in the case of presence of the sampler, while in the other case, part of the auxiliary flow combines sooner with the injector flow, with less heating by the external power. Therefore, this causes a higher temperature in the central region when the sampler is present, as we will see later in Figure 4.5. To obtain a more detailed picture close to the sampler, which is the most important region for mass spectrometry, Figure 4.4 illustrates the plasma temperature distribution in the radial direction, at several axial

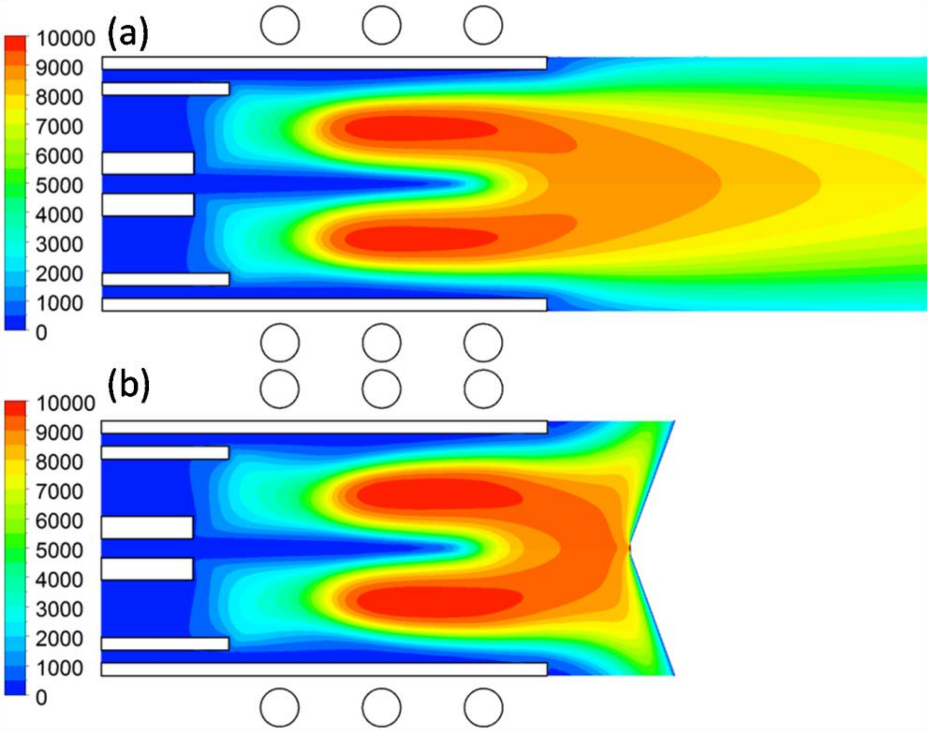

Figure 4.3: Effect of presence of sampler: 2D plasma temperature profile (K), (a) without and (b) with sampler.

positions, in the presence and absence of the sampler (i.e., solid and dashed lines, respectively). It is shown that the temperature in the presence of the sampler drops dramatically towards the central axis, with a sharp minimum at about 0.5-1 mm from the central axis, and it is higher again at the central axis. This can be explained by the cooling of the sampler, which has an orifice of 1 mm diameter.

It appears from the solid lines in Figure 4.4 that the radial temperature profile changes considerably, especially when moving closer towards the sampler. Even at 0.1 mm from the sampler (i.e., solid line in Figure 4.4.b), the profile looks different from the position of the sampler (i.e., solid line in Figure 4.4.a), especially near the central axis. This indicates that the above-mentioned cooling effect is only very local. This behavior is important when comparing simulation results with experiments, or different experimental data, i.e., they should be compared at exactly the same position.

Looking at the dashed lines in Figure 4.4 tells us that the temperature profile in the case without sampler is very similar for the different axial positions, with a broad maximum in the central region. Only in Figure 4.4.e and 4.4.f a minor local minimum can be observed at the central axis, which arises from the torus-shaped temperature profile in the coil region (see Figure 4.3 above). On the other hand, the temperature profile in the presence of a sampler is largely affected by the sampler, and differs a lot for different axial positions, especially near the sampler position, as discussed above. At the position of the sampler (Figure 4.4.a) the plasma temperature drops significantly in the central area and it increases in the outer regions, compared to the case without sampler. Lehn et al. [99] have reported the same behavior, but it should be mentioned that the setup of their experiments was different from ours and consequently, they observed a similar behavior but at different positions compared to our current work. The drop in the central region was explained above, i.e., it originates from the cooling from the sampler. The higher temperature in the outer regions is attributed to the different path lines, as shown in Figure 4.1.b above. Indeed, the gas flow which is accelerated to the orifice mostly originates from the central torch inlet, whereas the gas molecules coming from the intermediate and outer torch inlets, change their path and leave the ICP torch as they face the interface cone. This affects the temperature profile, as is shown in Figure 4.3.b, i.e., the high temperature plasma is spread towards the open sides of the torch, resulting in higher temperature values in the region outside the load coil, at radial positions farther away from the central axis, compared to the case without sampler (Figure 4.3.a). Therefore, the radial temperature distributions plotted in Figure 4.4 exhibit larger values in the outer regions in the case with sampler compared to without. A similar effect as in Figure 4.4.a is also observed in Figure 4.4.b, Figure 4.4.c and Figure 4.4.d, for the temperature profiles at 9.9 mm , 9.6 mm, and 9.3 mm away from the load coil, respectively, or in other words, 0.1 mm, 0.4 mm, and 0.7 mm from the sampler, respectively, although the cooling effect in the central region is far less pronounced. At positions further away from the sampler (see Figure 4.4.e-f) the temperature profiles with and without sampler look very similar, indicating that the sampler does not affect the temperature profile at positions beyond 1mm from the sampler.

Figure 4.5 shows the plasma temperature as a function of axial position on the central axis, again with and without sampler (i.e., solid and dashed line, respectively). Note that x = 0 mm corresponds to the position where the central torch inlet is placed. As shown in Figure 4.3, the temperature at the central axis is very low in the coil region, and it starts to increase dramatically at the end of the coil region. This can also

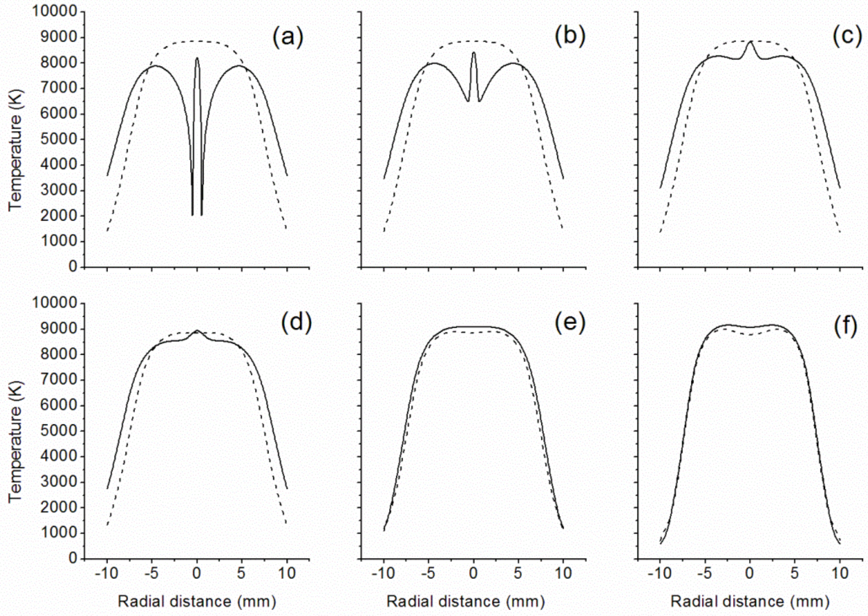

Figure 4.4 Effect of presence of sampler: Radial distributions of plasma temperature (K) in the case with (solid lines) and without (dashed lines) sampler, at several axial positions, i.e., at 10mm (place of the sampler) (a), 9.9mm (b), 9.6mm (c), 9.3mm (d), 8mm (e), and 6mm (f) from the load coil.

be seen in Figure 4.5. As the sampler is placed at 41.5 mm from the injector, the solid line stops at this position, while the dashed line continues till 70 mm from the injector. A slightly higher temperature at the central axis is observed in the case with sampler compared to without. This is attributed to the plasma heat conductivity from the slightly higher off-axis plasma temperature in this case, as mentioned above. Moreover, as seen in Figure 4.1, the path lines of the injector gas flow in the case with sampler are broader than in the case without sampler. Therefore, in Figure 4.1.b, the central path lines come closer to the region of high power coupling, which is another reason for the higher temperature at the central area of the torch. Only close to the sampler, the situation is reversed, and the plasma temperature drops significantly due to the presence of the cooled metal sampler, as was also observed in Figure 4.4. This so-called cross point (point ‘a’ in Figure 4.5) was also reported in [98] from images of ion fluorescence.

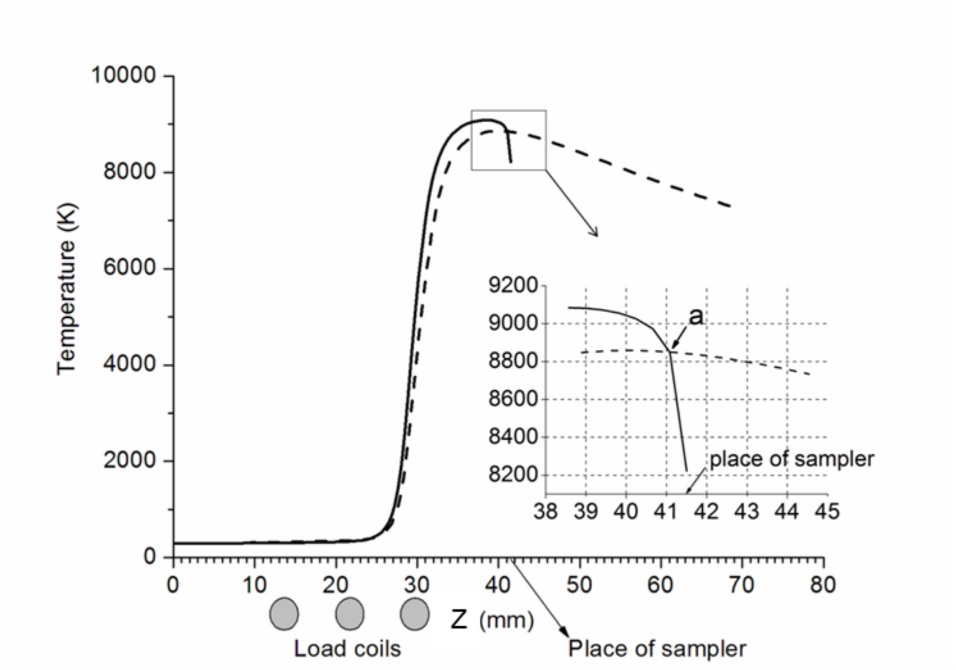

Figure 4.5 Effect of presence of sampler: Axial distribution of plasma temperature (K) in the case with (solid line) and without (dashed line) sampler, on the central axis of the plasma torch. The load coils and the place of the sampler are also indicated in this figure, for clarity. The small graph shows a detail of the crossing point of the two lines.

4.4. Electron density

Another fundamental property of the ICP is the electron number density, which determines the electrical conductivity in the plasma, as well as the analyte excitation and ionization rates due to electron impact [200,201].

Figure 4.6.a and 4.6.b present the 2D profiles of the electron density, without and with sampling interface, respectively. Again, the maximum electron density in both cases is reached at the position of maximum power coupling, where also the plasma temperature exhibits its maximum. Moreover, the electron density appears again somewhat higher in the case with sampler than without (i.e., about $1.5\times10^{22}\ m^{-3}$ vs. $1.3\times10^{22}\ m^{-3}$). This can be explained by the slightly higher maximum temperature in the case with sampler, as mentioned above.

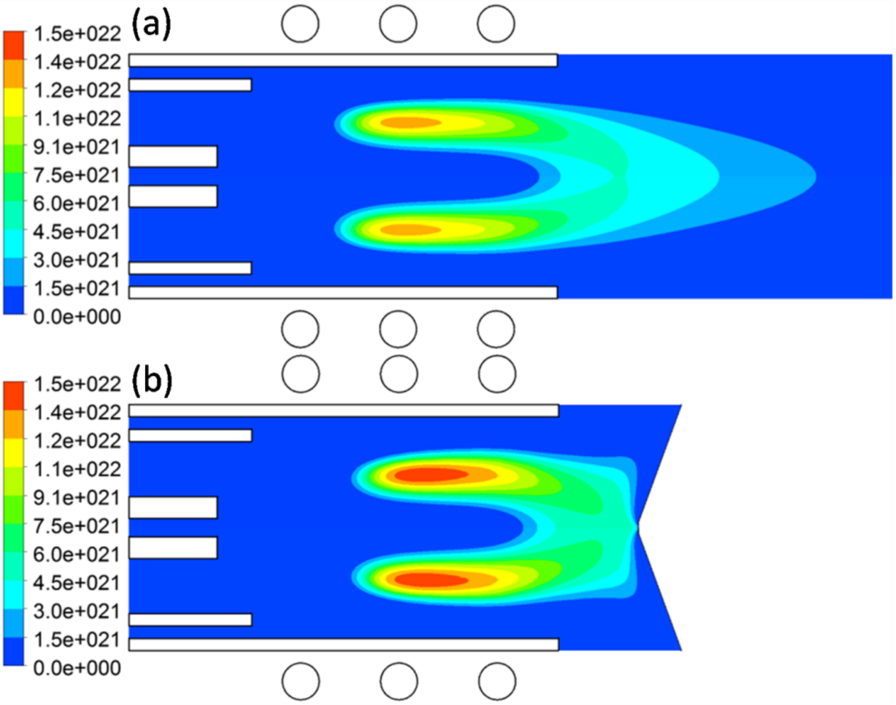

Figure 4.6 Effect of presence of sampler: 2D electron density profile (m^{-3}), (a) without and (b) with sampler.

In Figure 4.7, the radial distributions of electron density at different axial positions are presented in the case with and without sampling interface (solid and dashed lines, respectively). In the presence of a sampler, again the measurement position clearly affects the results obtained. At the position of the sampler (10 mm from load coil; solid line in Figure 4.7.a), the electron density exhibits two maxima at 4-5 mm from the center, and a small one in the center, whereas at 0.1 mm, 0.4 mm and 0.7 mm before the sampler (i.e., solid lines in Figure 4.7.b-d respectively), the peak in the center becomes much more pronounced. The general pattern here follows the plasma temperature changes discussed in section 4.3 above; however, the change in electron density is larger than for the plasma temperature, which can be explained from the temperature dependence in the Saha-Eggert equation $(n_e \propto T^{3/2} \exp[-(E_{ion} - \Delta E_{ion})/k_B T]$, where E_{ion} is the ionization potential, ΔE_{ion} is the ionization potential reduction and k_B is the Boltzmann constant) [21].

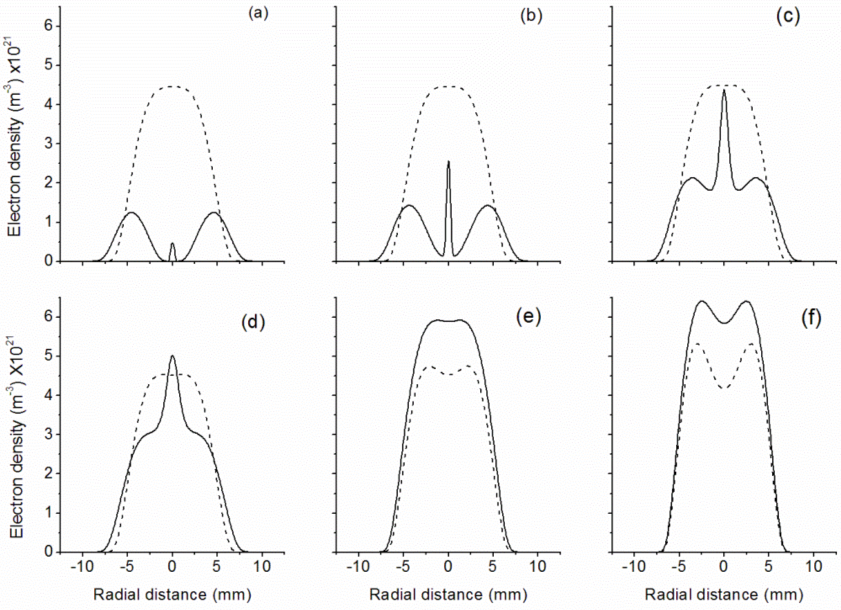

Figure 4.7 Effect of presence of sampler: Radial distributions of electron density (m^{-3}) in the case with (solid lines) and without (dashed lines) sampler, at 10mm (place of the sampler) (a), 9.9mm (b), 9.6mm (c), 9.3mm (d), 8mm (e), and 6mm (f) from the load coil.

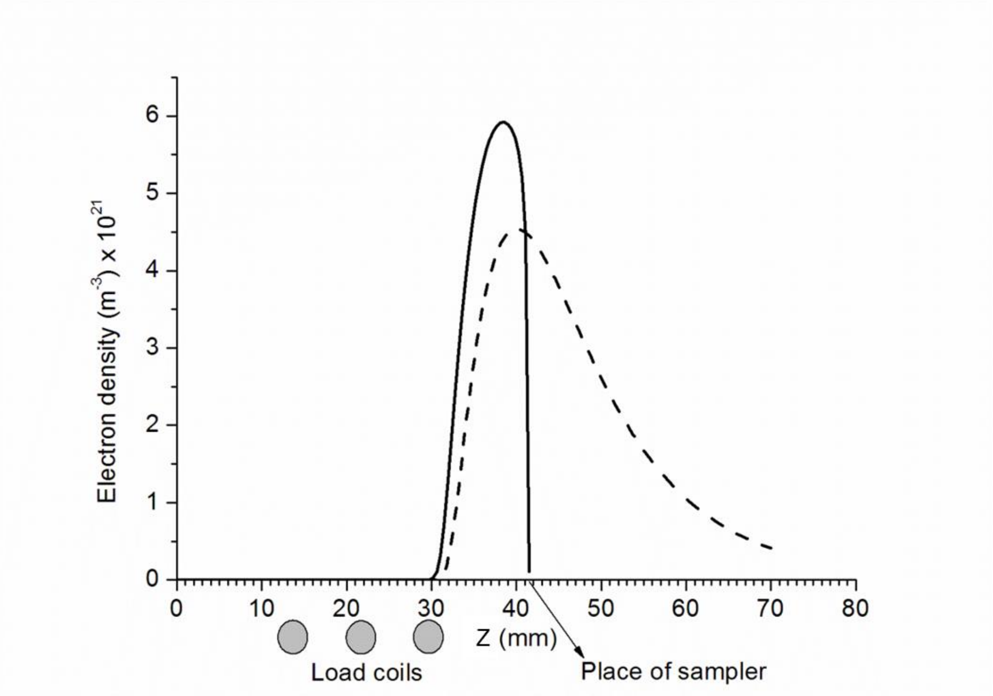

Figure 4.8 Effect of presence of sampler: Axial distribution of electron density (m^{-3}) in the case with (solid line) and without (dashed line) sampler, on the central axis of the plasma torch. The load coils and the place of the sampler are also indicated in this figure, for clarity.

The measurements by Lehn et al. [99] revealed the same behavior, but because of the different geometries, direct comparison is not possible. Looking at the dashed lines in Figure 4.7 (i.e., calculation results without sampler), it is seen that the profiles do not change a lot for different axial positions, except for the appearance of a small minimum near the center in Figure 4.7.f, which arises from the two characteristic maxima observed inside the coil region (see Figure 4.6). However, the profiles in the case with sampler are very much dependent on the axial position as discussed above. The closer to the sampler, the larger is the difference between the two profiles. In the case with sampling interface, the electron density becomes much lower in the central region and somewhat higher in the outer sides, at the position of the sampler (Figure 4.7.a) as well as at 0.1mm, 0.4 mm and 0.7 mm away from the sampler (Figure 4.7.b-d). The drop in density is attributed to the cooling effect of the interface cone in the central region, and the slightly higher density in the outer regions is due to the path lines of the intermediate and outer inlets, extending the plasma towards the outer region, as discussed above for the plasma temperature. As these positions are too close to the sampler for accurate measurements, there are no experimental data reported in literature for these positions. However, further away from the sampler, the electron density appears to be higher, both in the center and in the outer regions, as is shown in Figure 4.7.e and 4.7.f (indicating measurement positions of 2 mm and 4 mm from the sampler, respectively).

The latter effect is seen more clearly in Figure 4.8, illustrating the axial electron density profile at the center axis, with and without sampling interface (solid and dashed line, respectively). Close to the sampler, the electron density is near zero, and hence lower than in the case without sampler, but it shows a pronounced rise at a few mm from the sampler, and hence, in general the electron density is higher in the case with sampler than without, due to the slightly higher temperature, as explained above. This behavior was also reported by Ma et al. [98], based on ground state ion fluorescence measurements, obtained at positions of 1 mm from the sampler.

4.5. Conclusion

The effect of a mass spectrometer sampling interface on the fundamental plasma characteristics in an ICP, i.e., gas flow velocity, plasma temperature and electron density, is computationally investigated. The model deals with plasma by kinetic theory in the whole ICP torch region to provide a complete description of ICP-MS upstream the sampler.

The calculation results indicate that the maximum temperature and electron density increase when a sampling cone is inserted in the ICP. Moreover, the plasma velocity increases dramatically when flowing through the sampling orifice, due to the sudden pressure drop. The sampler cools the gas flowing into the MS, which results in a reduction of the total number of ions that can be measured. Thus, maybe an increase of the sampler temperature could yield an increased transmission of ions into the MS. The effect of the sampler is especially important in the downstream region from the plasma, but not so much in the most intense plasma region (i.e., the coil region). Other effects, such as for instance the effect of a nebulizer flow that also contains water, will mainly affect the plasma in the coil region, and the effect close to the sampler will probably be minor.

From the detailed radial profiles of temperature and electron density at different axial positions, we can see that the changes induced by the sampling cone are very sensitive to the distance from the sampler. The general behavior is a decrease in the central region and a rise in the outer areas for both the temperature and the electron density profiles, close to the sampler. Further away from the sampler, both temperature and electron densities are higher than in the case without sampler, also in the central region. These calculations are of great value, because they yield information about the plasma very close to the sampler, i.e., a region which is not or barely accessible by measurements and which is nevertheless the most important plasma region where the measured data are sampled from, as it is the connection point between the ICP and the mass spectrometer.

Chapter 5:

Optimizing the operating parameters

The purpose of this chapter is to systematically investigate the effect of the operating conditions on the upstream plasma characteristics of the ICP in contact with a MS interface. Thus, different injector gas and auxiliary gas flow rates are applied in a wide range. Moreover, the effect of the forward power is studied in detail. There seems to be an optimum range of injector gas flow rates for each setup which guaranties the presence and also a proper length of the central channel in the torch. Moreover, our modeling results show that for any specific purpose, it is possible to control that either only the central gas flow passes through the sampler orifice or that it is accompanied by the auxiliary gas flow. It was also found that depending on geometry, the variation of outgoing gas flow rate is much less than the variation of the injector gas flow rate and this causes a slightly higher pressure inside the torch. The general effect of increasing the applied power is a rise in the plasma temperature, which results in a higher ionization in the coil region. However, the negative effect is reducing the length of the cool central channel which is important to transfer the sample substances to the sampler. Using a proper applied power can enhance the efficiency of the system. Indeed, by changing the gas flow path lines, the power can control which flow (i.e., only from the injector gas or also from the auxiliary gas) goes to the sampler orifice. The calculation results will be compared with measured data from [100, 108, and 109].

This chapter is based on the following publication: M. Aghaei, H. Lindner, A. Bogaerts, Optimization of operating parameters for inductively coupled plasma mass spectrometry: A computational study, Spectrochim. Acta Part B 76 (2012) 56-64.

5.1. Effect of injector gas flow rate

It is well known that adjustments in the injector gas flow rate will lead to a change in the axial distribution of ions in the ICP [202-203]. The gas flow path lines, originating from the central and outer inlets, colored by velocity in m/s, are plotted in Figure 5.1 at different injector gas flow rates, ranging from 0.3 to 1.4 L/min. The path lines originating from the intermediate inlets are colored in black to be distinguishable from the ones from the central and outer inlets, and for the sake of further discussions. The flow rates of the coolant and auxiliary gas are 12 L/min and 0.4 L/min, respectively.

The formation of a central channel in the ICP torch upon increase of the injector gas flow rate can be studied in Figure 5.1. In Figure 5.1.a, no central channel is formed yet and the injector flow is not straight at all. By increasing the flow rate of the central injector to 0.35L/min (see Figure 5.1.b), a small part of the flow moves directly toward the end of the torch and faces the sampler cone without turning toward the outer sides in the coil region. To explain this, we refer to the so-called “transition flow rate” introduced by Lindner et al. in [181]. Indeed, for each specific central inlet diameter, there is a specific transition flow rate below which the injector flow does not go straight and does not form a central channel (see Figure 9 in ref [181]). This means that depending on the geometrical setup, the central channel could only be observed above a specific injector gas flow rate (i.e., 0.3 L/min in the current study). Therefore, in order to guide the sample substances efficiently along the torch and toward the mass spectrometer, the injector gas flow rate should exceed this crucial transition flow rate.

By further increasing the injector gas flow rate, the fraction of central path lines which turns toward the outer sides of the torch decreases and a larger fraction of path lines goes straight toward the sampler orifice (see Figure 5.1.b-f). This trend continues until an injector flow rate of 1.0 L/min (see Figure 5.1.f), when 100% of the injector gas flows in a more or less straight line through the central channel. In [109], Gamez et al. also demonstrated experimentally that the central channel becomes well-defined only at flow rates above 1.0 L/min. When the injector gas flow rate further increases to 1.2 and 1.4 L/min (see Figure 5.1.g and h), the injector gas stays along the central line; however, a change in the pattern of the auxiliary gas is seen in Figure 5.1.h, i.e., a part of the auxiliary gas comes closer to the central line.

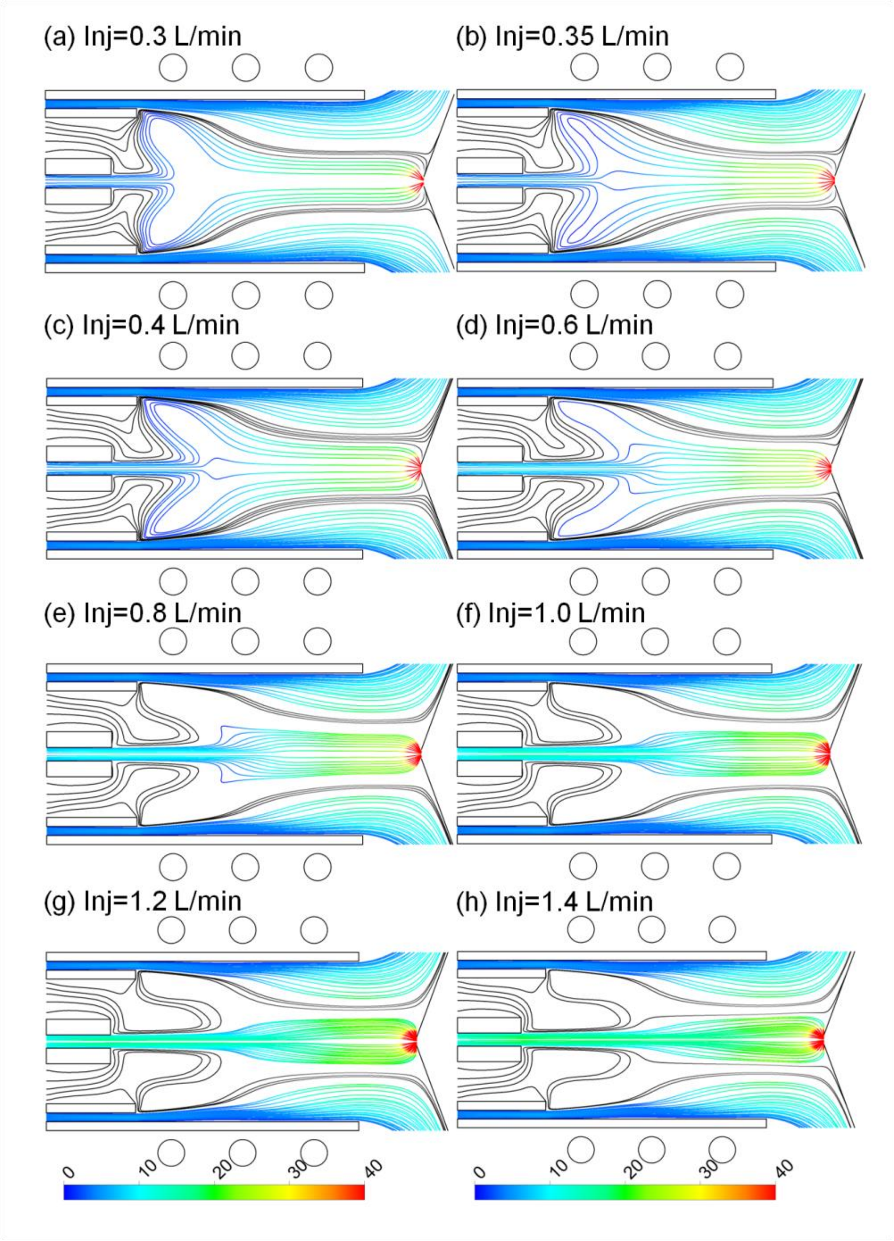

Figure 5.1: Effect of injector gas flow rate: 2D gas flow velocity path lines originating from the central and outer inlets, colored by velocity in m/s, and from the intermediate inlet, colored in black, at different injector gas flow rates, ranging from 0.3 to 1.4 L/min. The intermediate gas and outer gas flow rates are kept fixed at 0.4 and 1.2 L/min and the power is 1000W.

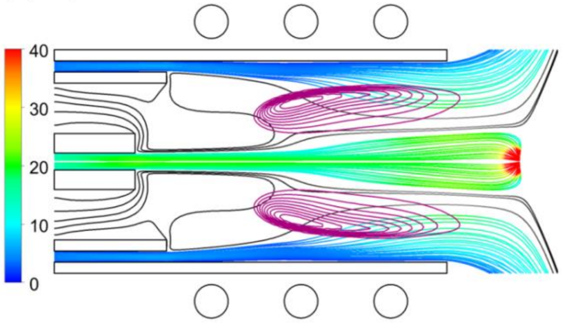
(a) Inj=1.6 L/min

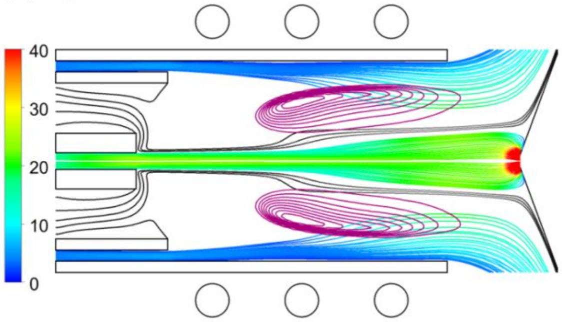
(b) Inj=1.8 L/min

Figure 5.2: Effect of injector gas flow rate: 2D gas flow velocity path lines originating from the central and outer inlets, colored by velocity in m/s, and from the intermediate inlet, colored in black, at (a) 1.6 and (b) 1.8 L/min injector gas flow rates. The purple contours demonstrate the area of external power coupling. The other conditions are the same as in Figure 5.1.

This is studied in detail in Figure 5.2, which shows the path lines at still higher flow rates, i.e. 1.6 and 1.8 L/min. The purple contours demonstrate the area of external power coupling. It is shown in Figure 5.2.a and especially from Figure 5.2.b that the flow originating from the intermediate inlet passes through a region where the amount of the coupled electrical power is low (i.e., the outer part of the purple contours in Figure 5.2). This means that the efficiency of power coupling to the plasma decreases, because the auxiliary gas cannot transfer the external power and heat up the injector gas. It is known that a rise in injector gas flow rate, at fixed external power, always leads to a lower plasma temperature inside the torch, as will be demonstrated in Figure 5.3 below; however, the behavior illustrated in Figure 5.2 is the reason why the transport efficiency of aerosol drops for flow rates above 1.4 L/min, as is reported by Macedone et al. [100]. Therefore, the current calculations predict that the injector gas flow rate should not exceed 1.4 L/min in order to keep the aerosol transport efficiency acceptable. On the other hand, as discussed above, to ensure that the injector gas entirely flows in a straight line and efficiently guides the sample substances toward the mass spectrometer, the injector gas flow rate should be at least 1.0 L/min. Therefore, our calculations predict that for the operating conditions under study (i.e., geometrical setup of Figure 2.1 with 1 mm sampler orifice diameter, auxiliary gas flow rate = 0.4 L/min, coolant gas flow rate = 12 L/min and power = 1000 W), the optimum injector gas flow rate is around 1.0 - 1.2 L/min.

Figure 5.3 illustrates the 2D profiles of the plasma temperature at different injector gas flow rates, ranging from 0.3 to 1.4 L/min (i.e., the same as in Figure 5.1 above). It is shown that increasing the injector gas flow rate yields a general drop in temperature, but simultaneously, the (cooler) central channel becomes more distinguished (see Figure 5.3.f, g, h). The small black lines above each plot in Figure 5.3 indicate the length of the cool central channel, to make this clear. This effect of injector gas flow rate on the central channel is in agreement with experiments. Indeed, it was measured in [109] that a higher injector gas flow rate yields a wider central channel.

As illustrated in Chapter 4, the electron density profiles show the same pattern as the plasma temperature profiles, and they are therefore not presented here in 2D plots. However, Figure 5.4 presents the electron density in the plasma at the edge of the sampler orifice (i.e., at an axial position of 41.5 mm and at 0.5 mm above the central axis) as a function of injector gas flow rate. Following the behavior of the plasma temperature, the general effect of increasing the injector gas flow rate is a drop in electron density, which is indicated for the flow rates above 0.6 L/min. However, a rise in electron density upon increasing injector gas flow rate for the flow rates below 0.6 L/min is observed in Figure 5.4. To explain this trend, we refer to the relevant flow path lines in Figure 5.1 (i.e. Figure 5.1.a, b, c, d). It is shown that in these cases, a part of the injector gas flow passes through the high power coupling areas (cf. Figure 5.2) and directly receives the energy and becomes ionized; however, for the higher flow rates, the injector gas flow is heated up mostly by the heat transferred from the auxiliary gas. Referring to Figure 5.2, it can therefore easily be understood why at injector gas flow rates above 1.4 L/min, the electron density is too small, as is indeed observed in Figure 5.4.

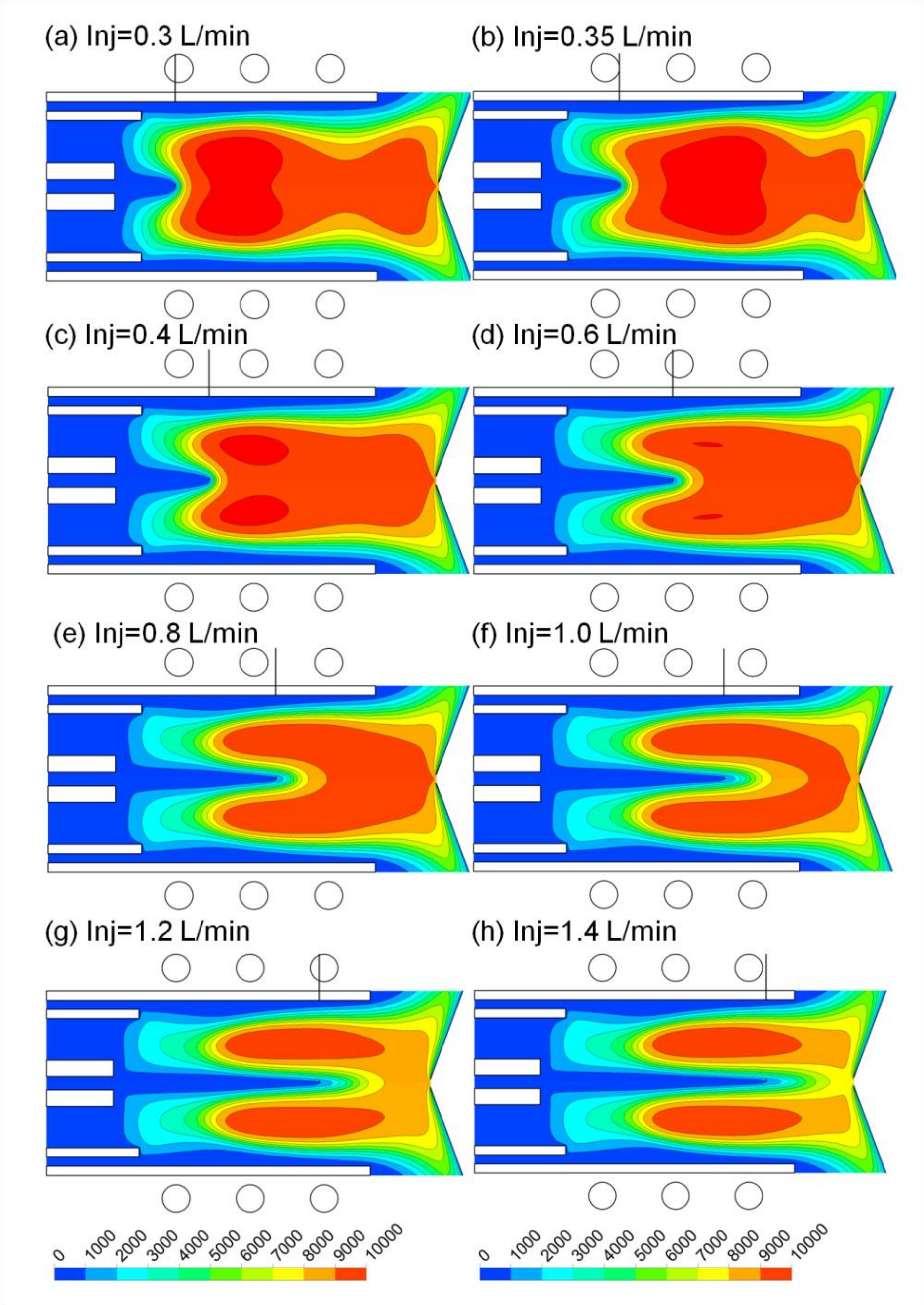

Figure 5.3: Effect of injector gas flow rate: 2D temperature profiles (K), at different injector gas flow rates, ranging from 0.3 to 1.4 L/min. The other conditions are the same as in Figure 5.1. The small black lines above each plot indicate the length of the cool central channel.

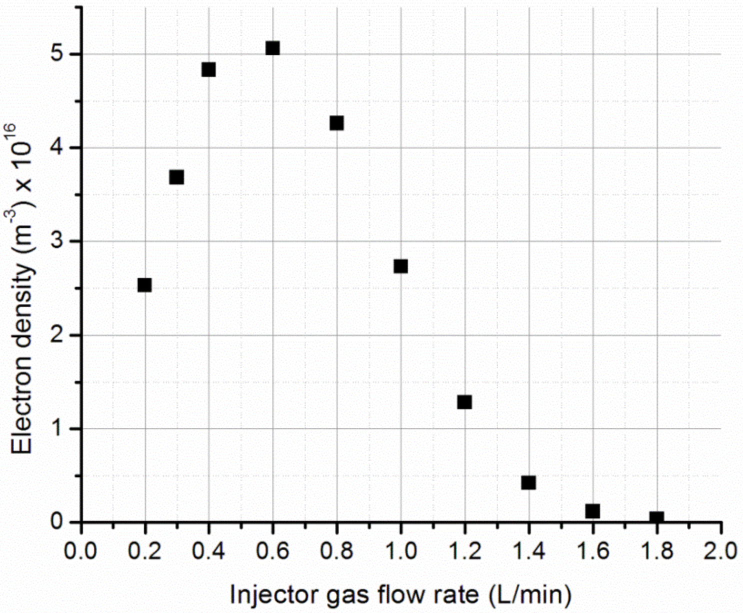

Figure 5.4: Effect of injector gas flow rate: Electron density (m^{-3}) in the plasma at the edge of the sampler orifice (i.e. at an axial position of 41.5 mm and at 0.5 mm above the central axis) as a function of injector gas flow rate.

Figure 5.5 shows the outgoing gas flow rate from the ICP torch to the mass spectrometer through the sampler orifice, in L/min, for different injector gas flow rates. When the injector gas flow rate increases from 0.3 to 1.4 L/min, the flow rate passing through the sampler orifice only changes from 1.12 to 1.21 L/min. Hence, at fixed conditions of geometry and pressure behind the sampler, changing the injector gas flow rate does not change significantly the flow rate passing through the sampler. This implies that the gas pressure inside the torch should increase, because the amount of flow inserted is increasing while the amount of outgoing flow is almost constant, and hence more gas stays inside the ICP torch. It should be noted that the flow inserted from the central inlet never escapes to the open sides of the torch (see Figure 5.1) and the only way of exiting the torch is through the sampler. Figure 5.6 presents the pressure inside the ICP torch at different points along the central channel, for different injector gas flow rates. The rise of pressure due to the rise in the injector gas flow rate is

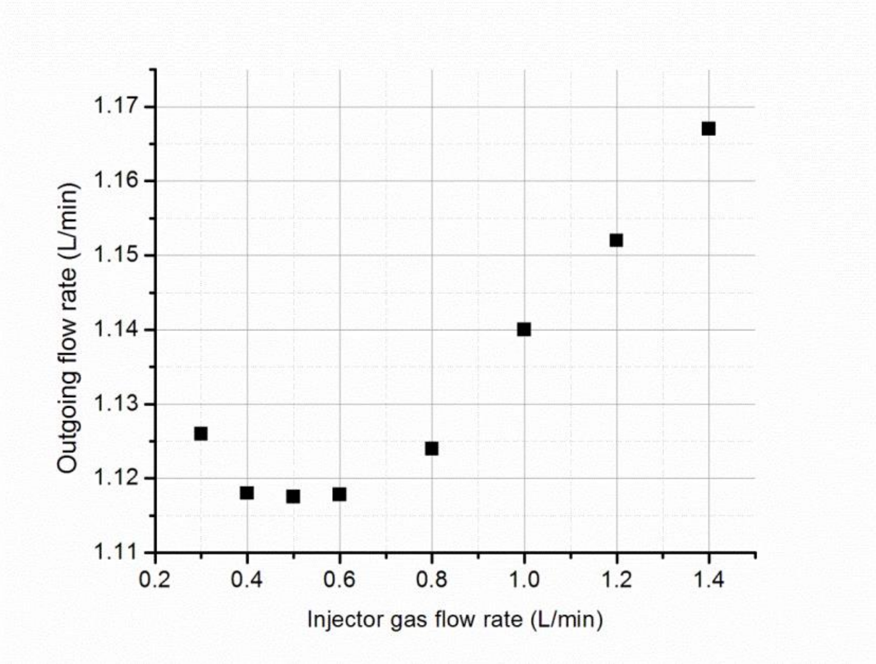

Figure 5.5: Effect of injector gas flow rate: Outgoing gas flow rate (in L/min) from the ICP torch to the mass spectrometer through the sampler orifice, in L/min, for different injector gas flow rates.

confirmed by this figure, and is especially apparent near the gas inlets (i.e., at x = 0 mm). However, looking at the y-axis, it can be seen that the changes in the pressure are limited. Indeed, in the current study, for a sampler orifice of 1 mm diameter and a central inlet of 1.5 mm diameter, a change in injector gas flow rate of 1.1 L/min causes 0.095 L/min change in the outgoing flow rate, and this results in a pressure rise of at maximum about 140 Pa (or $1.4\text{x}10^{-3}$atm) inside the torch. These values can be different for different geometrical shapes of the ICP.

In order to understand better the behavior of the path lines inside the torch, we will now focus on the path lines going out through the sampler toward the mass spectrometer. As shown in Figure 5.1. a-c, for the flow rates up to 0.4 L/min (i.e. 0.3, 0.35, 0.4 L/min), in addition to the injector gas, a part of the auxiliary gas also exits through the sampler orifice, while for the higher flow rates (i.e. Figure 5.1.d-h), only the injector gas can escape through the sampler orifice. This change in the behavior of the auxiliary gas flow can be explained by the ratio of auxiliary gas and injector gas

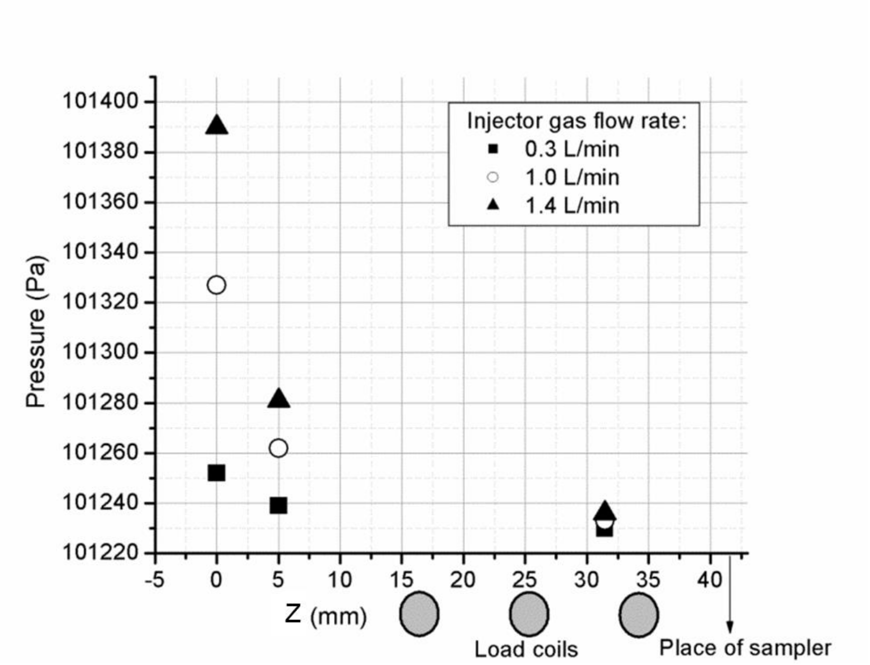

Figure 5.6: Effect of injector gas flow rate: Pressure (Pa) inside the ICP torch at different points along the central channel, for different injector gas flow rates. The load coils and the place of the sampler are also indicated in this figure, for clarity.

flow rates. In these simulations, the auxiliary flow rate was set to 0.4 L/min. Therefore, it appears that at injector gas flow rates above this value of auxiliary gas flow rate, only the injector gas can escape through the orifice, whereas at injector gas flow rates below or equal to the auxiliary gas flow rate, both the auxiliary and injector gas can pass through the orifice. To investigate this behavior in more detail and to check whether this thumb rule is generally valid, we performed calculations with various auxiliary gas flow rates, as will be presented in the next section.

5.2. Effect of auxiliary gas flow rate

Calculations are performed with various auxiliary gas flow rates, i.e. 0.6, 0.8, and 1.0 L/min, as presented in Figure 5.7.a, b and c, respectively. The results with auxiliary gas flow rate of 0.4 L/min were presented in Figure 5.1 above. In all plots of Figure 5.7, the flow originating from the central inlet passes through the sampler orifice, and the flow originating from the outer inlet escapes to the open sides of the torch. Hence, the exit patterns of injector and coolant gas flows always stay the same. However, for the auxiliary gas flow, the pattern is changed, depending on the values of the injector and auxiliary gas flow rates. Indeed, if the injector gas flow rate is lower than or equal to the auxiliary gas flow rate (i.e. Figure 5.7. a1, a2, b1, b2, c1 and c2), our calculations predict that some part of the auxiliary gas can pass through the sampler cone. On the other hand, when the injector gas flow rate is higher than the auxiliary gas flow rate (i.e. Figure 5.7. a3, b3 and c3), all the auxiliary gas escapes to the open sides of the torch and it does not pass through the sampler. This behavior was observed for all

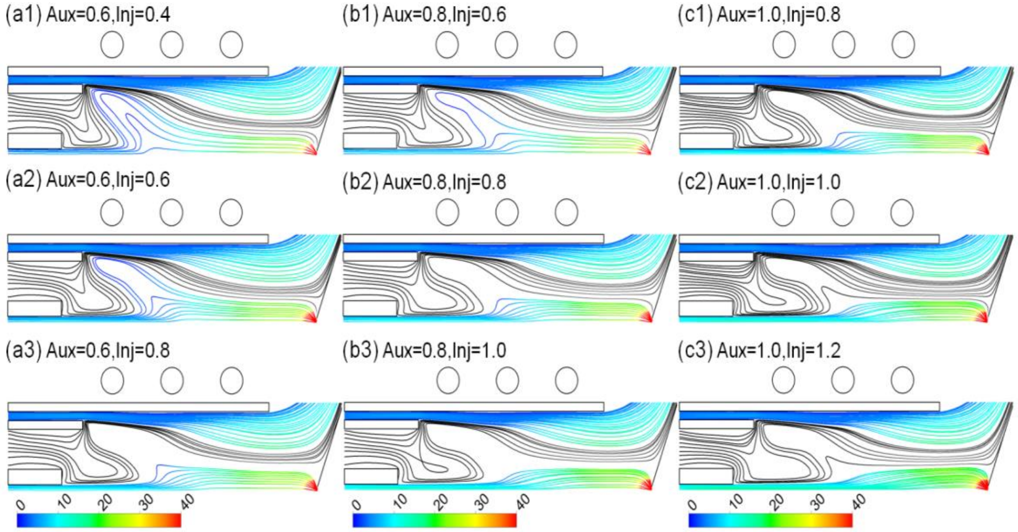

Figure 5.7: Effect of auxiliary gas flow rate: 2D gas flow velocity path lines originating from the central and outer inlets, colored by velocity in m/s, and from the intermediate inlet, colored in black, at (a) 0.6, (b) 0.8 and (c) 1.0 L/min auxiliary gas flow rates. The injector gas flow rate is (1) lower than, (2) equal to and (3) higher than the auxiliary gas flow rate. Only half of the 2D axisymmetric torch is plotted.

injector gas flow rates investigated, i.e., higher than 0.3 L/min and lower than 1.2 L/min.

The behavior is somewhat different for an auxiliary gas flow rate as low as 0.3 L/min or as high as 1.2 L/min, as is illustrated in Figure 5.8. Figure 5.8.a1-a4 shows the flow path lines for an auxiliary gas flow rate of 0.3 L/min. It is indicated by these plots that when the auxiliary gas flow rate is 0.3 L/min (or less), some fraction of the auxiliary gas can pass through the orifice even when the injector gas flow rate is higher than the auxiliary gas flow rate (i.e., up to 0.5 L/min; see Figure 5.8.a3). Only when the injector gas flow rate becomes 0.6 L/min (see Figure 5.8.a4), the auxiliary gas cannot escape through the orifice anymore. This suggests that for the injector gas flow rates in the range of 0.3 - 0.5 L/min, the amount of gas flowing through the orifice is too low for filling the orifice, and there is still “room” for some auxiliary gas. If we want to have only the injector gas entering the mass spectrometer, as this gas flow typically contains the sample substances to be analyzed, we should increase the injector gas flow rate to values of 0.6 L/min or higher, as shown in Figure 5.8.a.4. Therefore, by tuning the values of injector gas flow rate and auxiliary gas flow rate, we can control which gas fraction enters the mass spectrometer, and this might be a way to increase the detection efficiency.

On the other hand, when the auxiliary gas flow rate is 1.2 L/min (and more), the auxiliary gas can even not pass through the orifice when the injector gas flow rate is still 0.2 L/min lower than the auxiliary gas flow rate (i.e., 1.0 L/min; see Figure 5.8.b.2), and only the injector gas can enter the mass spectrometer. This suggests that in this range of injector gas flow rate (i.e., 1.0 to 1.4 L/min), the amount of gas originating from the central inlet is high enough to completely fill the orifice and it does not allow any other flow (e.g., originating from the intermediate inlet) to pass through the sampler orifice. Only for an injector gas flow rate of 0.8 L/min or less (see Figure 5.8.b.1), some fraction of the auxiliary gas can pass through the sampler orifice.

Again, we can conclude that for each specific geometrical shape, by setting the proper flow rates for the injector and auxiliary gas, we can control which gas can escape through the sampler orifice. The sample substances are inserted together with the injector gas flow into the torch. If the analyte ion cloud is small, which means that the analytes do not diffuse more than 2-3 mm, i.e., the width of the injector gas flow, they are only transported by the injector gas stream. Therefore, the ion detection efficiency would be higher in the case that only the injector gas passes through the sampler.

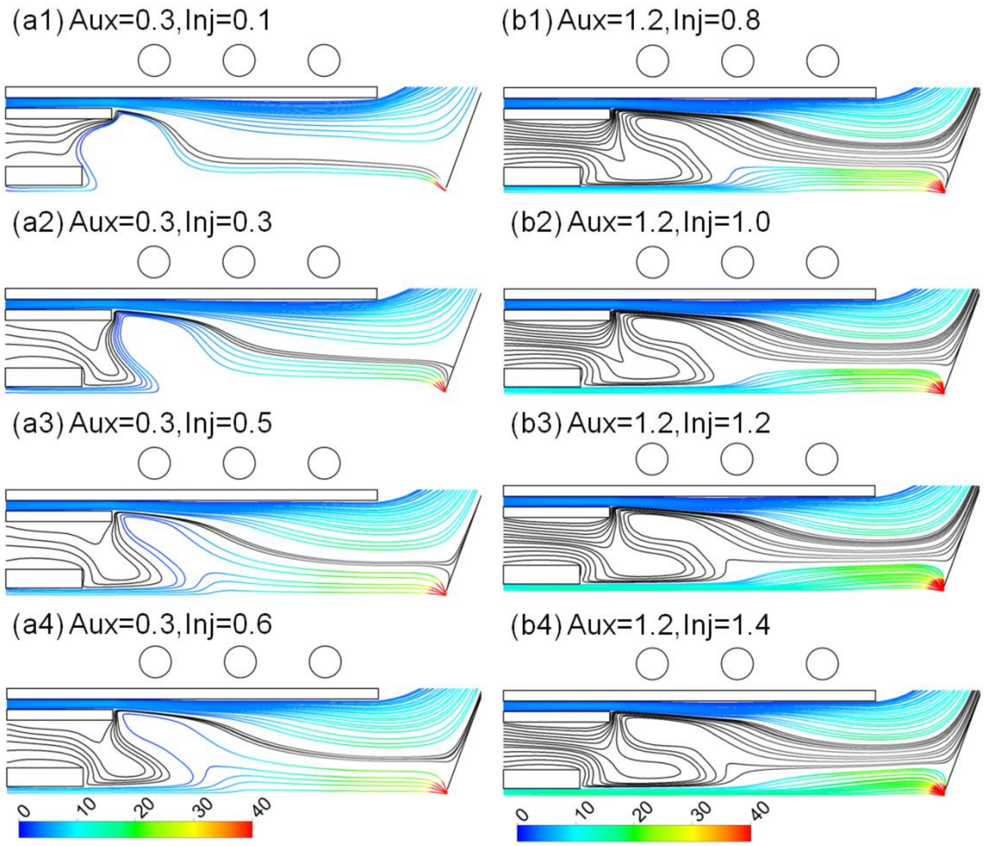

Figure 5.8: Effect of auxiliary gas flow rate: 2D gas flow velocity path lines originating from the central and outer inlets, colored by velocity in m/s, and from the intermediate inlet, colored in black, at (a) 0.3 and (b) 1.2 L/min of intermediate gas flow rates and different values of injector gas flow rate. Only half of the 2D axisymmetric torch is plotted.

However, depending on the position upstream the ICP where analyte diffusion starts, the diffusion length can also be larger than the injector flow width. This means that some of the analyte ions will also be in the auxiliary gas stream, and in that case, it would be better that also (part of) the auxiliary gas can pass through the sampler orifice. It should be noted that the width of the injector flow depends on the torch and sampler geometry, especially on the diameter of the central inlet and of the sampler orifice.

5.3. Effect of applied power

To study the effect of the applied power on the plasma characteristics in the ICP, calculations were performed for several values of applied power, i.e., 750, 1000, 1250 and 1500W. The injector gas flow rate is kept fixed at 1 L/min and the coolant and auxiliary flow rates are 12 L/min and 0.4 L/min, respectively.

Figure 5.9 shows the gas flow path lines, originating from the central and outer inlets, colored by velocity (in m/s) for different applied powers. Again, the path lines originating from the intermediate inlets are colored in black for better visualization. The purple contours demonstrate the area of maximum external power coupling. It can be seen that the shape, size and position of these efficient power coupling regions change by varying the applied power. At 750, 1000 and 1250W (see Figure 5.9 a, b, c) the auxiliary gas flows entirely through the efficient power coupling areas. On the other hand, at 1500W (Figure 5.9.d), the intermediate flow passes through a region with lower coupled power, while most power is transferred to the coolant gas. Indeed, by increasing the applied power, the auxiliary gas flow is slightly shifted to the central region of the torch. This behavior was not observed in the absence of the sampler cone (see chapter 4). Besides the effect on the auxiliary gas flow path lines, the higher applied power also causes the injector gas flow path lines to expand more rapidly, and this trend was also found to be more significant in the presence of the sampler. Finally, the power also affects the fraction of gas that can pass through the sampler orifice. Indeed, at 750, 1000 and 1250W, the auxiliary gas will entirely escape to the open sides of the ICP torch and only the injector gas flow reaches the sampler orifice. At 1500W, however, a part of the auxiliary gas, along with the injector gas, passes through the sampler orifice. Hence, the gas reaching the sampler is not just the injector gas flow which contains the sample substances to be analyzed, and this may lead to a lower detection efficiency. At first sight, it seems surprising that a higher applied power would yield a lower detection efficiency, but it is also reported in [100] that only a rise in power up to 1300W causes a better transport efficiency, while for power values above 1300 W, the transport efficiency decreases, which is in agreement with our computational results.

Another, more expected effect of increasing the power is a rise in the plasma temperature inside the torch. In Figure 5.10, the 2D temperature profiles are depicted at different applied powers. In fact, when the plasma temperature inside the coil region increases due to higher power input, this also yields a higher temperature in the rest of

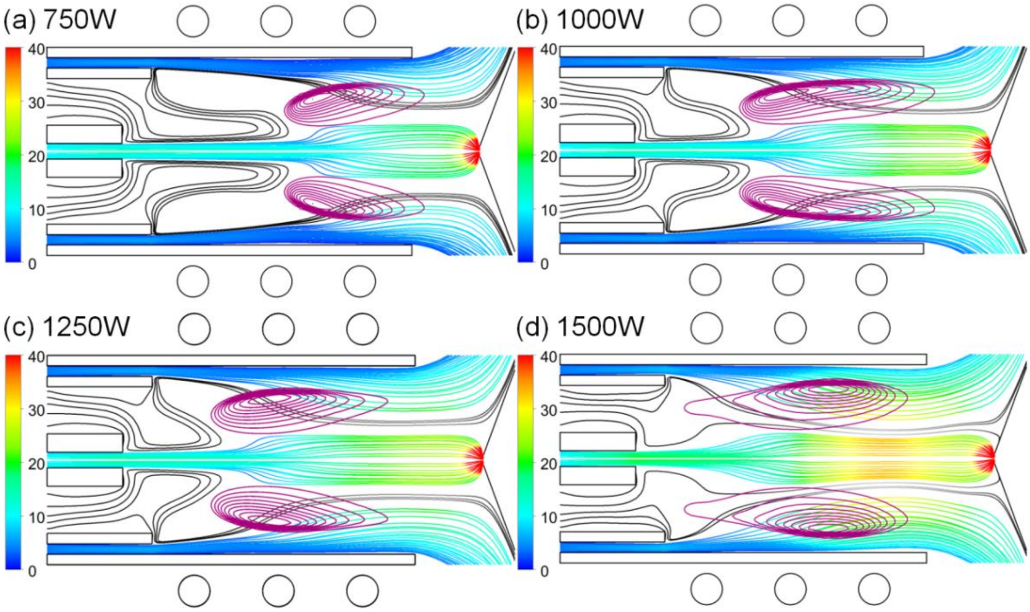

Figure 5.9: Effect of applied power: 2D gas flow velocity path lines originating from the central and outer inlets, colored by velocity in m/s, and from the intermediate inlet, colored in black, at (a) 750, (b) 1000, (c) 1250 and (d) 1500W of applied power. The injector, auxiliary and coolant gas flow rates are kept fixed at 1.0, 0.4 and 1.2 L/min.

the ICP, and therefore the length of the cool central channel decreases slightly, as indicated by the small black lines above each plot. This means that the sample particles should pass through a hotter central channel, which is to be avoided, because a cool central channel is crucial for transferring the sample substances to the sampler. Combining the effect of power on the gas flow path lines and on the temperature profiles, it can be concluded that a rise in the applied power increases the plasma temperature, which leads to more ionization in the coil region, but on the other hand, it also causes the central channel to become less cool and a bit narrower, which should be avoided (see above). Therefore, our calculations suggest that the applied power should be kept below 1500W (favorably up to 1250W) for the conditions under study. Moreover, a fraction of the auxiliary gas will be able to pass also through the sampler orifice when the power becomes too high. Again, it depends on the ion cloud diameter compared to the width of the injector gas flow whether the latter is beneficial or not (see above). However, as the geometry used in this model is the same as the one used

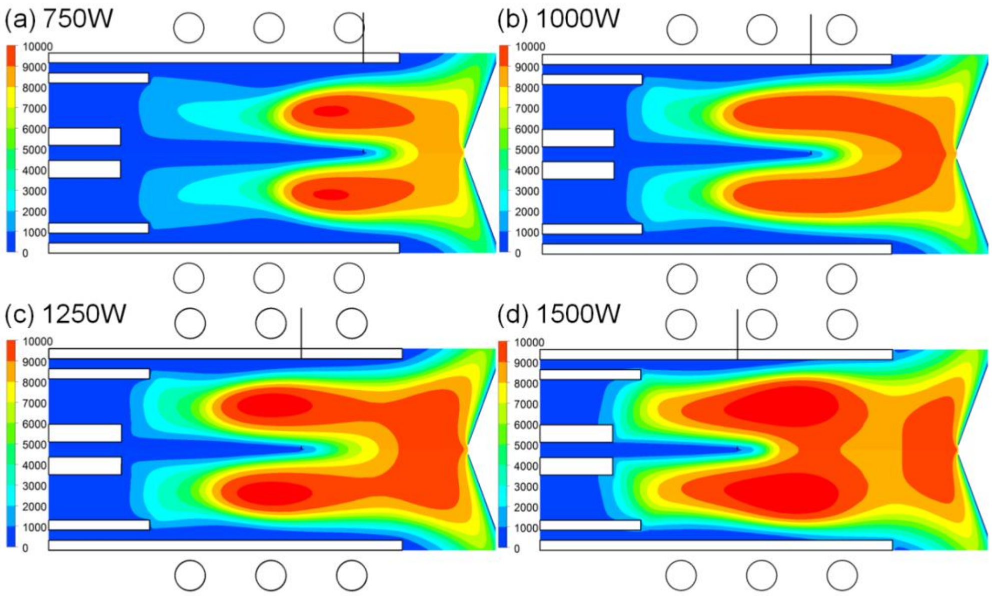

Figure 5.10: Effect of applied power: 2D temperature profile (K), at (a) 750, (b) 1000, (c) 1250 and (d) 1500W of applied power. The other conditions are the same as in Figure 5.9. The small black lines above each plot indicate the length of the cool central channel.

by Farnsworth et al. [100], it seems beneficial for the ICP-MS detection efficiency using a similar geometry as our work to allow only the injector gas flow passing through the sampler orifice toward the mass spectrometer because a lower detection efficiency is reported in [100] for the higher coupled power (1500W), which is the case when the auxiliary gas also passes through the sampler.

5.4. Conclusion

The effect of injector gas flow rate, auxiliary gas flow rate, and applied power on the plasma characteristics in an ICP connected to a mass spectrometer is computationally studied, in order to optimize the operating conditions for good analytical practice in ICP-MS. It should be noted that we kept the frequency of the external current fixed at 27 MHz as it is the value used commonly in analytical applications.

Our calculations predict that the optimum injector gas flow rate is around 1.0 - 1.2 L/min for the conditions under study (i.e., geometrical setup, auxiliary gas flow rate, power…). Indeed, to ensure that the injector gas entirely flows in a straight line and efficiently guides the sample substances toward the mass spectrometer, the injector gas flow rate should be at least 1.0 L/min. On the other hand, the injector gas flow rate should not exceed 1.4 L/min, to avoid that the auxiliary gas cannot pass through regions in the plasma with high power coupling and will not be able to transfer the energy efficiently to the injector gas.

It was also observed that when increasing the injector gas flow rate, the outgoing flow rate (i.e., passing through the sampler orifice) does not vary so much, so that a higher injector gas flow rate causes a slightly higher pressure inside the torch.

Furthermore, the calculation results have demonstrated that the injector gas flow rate should preferentially be higher than the auxiliary gas flow rate, to avoid that the auxiliary gas can pass through the sampler orifice, and to ensure that only the injector gas can enter the mass spectrometer, which is necessary to optimize the detection efficiency of the sample substances, at least in the case when the ion cloud diameter is small, i.e., when the analyte ions are transported only by the injector gas.

The latter effect can also be achieved by tuning the applied power. Indeed, the applied power affects the gas flow path lines, and can therefore control which flow (i.e., only the injector gas or also the auxiliary gas) can pass through the sampler orifice. Furthermore, depending on the geometry, the general effect of increasing the applied power is a rise in the plasma temperature which results in a higher ionization in the coil region. However, it also results in a reduction of the length of the cool central channel, which is crucial for transferring the sample substances to the sampler. Moreover, at too high power values (~ 1500 W for the gas flow rates under study in this Chapter), the auxiliary gas cannot pass through the high power coupling regions in the plasma anymore, and will not be able to transfer the energy efficiently to the injector gas. Therefore, our calculations predict that the optimum applied power will be in the range of 1000 - 1250 W at the conditions under study.

Chapter 6:

Optimizing the geometrical parameters

In the present chapter, the effects of sampler orifice diameter (ranging from 1 to 2 mm) and distance of sampler cone from the load coil (ranging from 7 to 17 mm) are studied. An increase in sampler orifice diameter leads to a higher central plasma temperature at the place of the sampler, as well as a more efficient gas transfer through the sampler, by reducing the interaction of the plasma gas with the sampling cone. However, the flow velocity at the sampler position is found to be independent from the sampler orifice diameter. Moreover, by changing the sampler orifice diameter, we can control whether only the central gas or also the auxiliary gas can exit through the sampler. Finally, at increasing distance of the sampler from the load coil, the plasma temperature at the place of sampler decreases slightly, which might also have consequences for the ion generation and transport through the sampling cone. The calculation results will be compared with measured data from [108,109].

This chapter is based on the following publication: M. Aghaei, H. Lindner, A. Bogaerts, Effect of sampling cone position and diameter on the gas flow dynamics in an ICP, J. Anal. At. Spectrom. 28 (2013) 1485-1492.

6.1. Operating and geometrical conditions

The total power coupled to the plasma is set to 1000 W and the frequency of the harmonic external electric current density is 27 MHz. The injector gas flow rate is 1 L/min (except for figure 6.3) and the flow rates of the coolant and auxiliary gases are 12 L/min and 0.4 L/min, respectively. The ambient gas pressure and exhaust pressure are set to 101325 Pa and 101225 Pa, respectively. The pressure downstream of the sampler is set to 133.32 Pa. The schematic picture of the ICP geometry used in the simulations is shown in Figure 2.1. A large number of sampler distances from the load coil, ranging from 7 mm to 17 mm, and different sampler orifice diameters, ranging from 1 to 2 mm, are considered in the model. For different sampler distances from the load coil, new geometries were made in GAMBIT and separately read into FLUENT. Also, for each sampler distance, we made geometries with three different orifice diameters, i.e., 1 mm, 1.5 mm and 2 mm. Note that another geometrical parameter, i.e., the central inlet diameter, was already investigated by Lindner et al. in [181], so it is kept constant here (= 1.5 mm).

6.2. Plasma temperature and gas flow path lines

Figure 6.1 shows the 2D plasma temperature profiles (upper frames) and velocity path lines (lower frames) for two different sampler orifice diameters, i.e., 1 mm (left column) and 2 mm (right column), at different sampler positions, i.e., 7 mm (first row), 10 mm (second row) and 13 mm (third row) distance from the load coil. We performed calculations for a sampling position up to 17 mm distance from the load coil, but as the pattern is the same in all cases, only the data for a sampling position of 7 mm, 10 mm and 13 mm are shown here for clarity. When comparing the two columns in Figure 6.1, it is seen that the outgoing pattern of the auxiliary gas (see black path lines) is quite different when changing the sampler orifice diameter. At 1 mm diameter, all the auxiliary gas is leaving through the open sides of the torch, while at 2 mm diameter, the auxiliary gas exits through the sampler orifice and goes to the MS, together with the injector gas.

As demonstrated in section 5.2, the flow pattern of the auxiliary gas can also be controlled by varying the ratio of auxiliary and injector gas flow rates. The results presented in Chapter 5 were obtained for an injector diameter of 1.5 mm and a sampler orifice diameter of 1 mm, like in the left column of Figure 6.1, but it is seen that changes in the geometrical parameters affect this behavior. Indeed, in the present Chapter, the injector gas flow rate is higher than the auxiliary gas flow rate (i.e., 1.0 vs 0.4 L/min; cf above), so according to section 5.2 we would expect to have only the injector gas flowing through the sampler orifice and the auxiliary gas exiting through the open sides of the torch. However, this appears not to be the case for the orifice diameter of 2 mm (see Figure 6.1, right column). Indeed, also the ratio between the central inlet and the sampler orifice diameter plays a role. In the left column, the central inlet diameter (kept fixed at 1.5 mm) is larger than the sampler orifice diameter, and in this case, the same results are obtained as in section 5.2. However, in the right column, the diameter of the central inlet is smaller than the diameter of the sampler orifice, and in this case, the auxiliary gas can pass through the sampler orifice. Hence, it can be concluded that the outgoing flow pattern of the auxiliary gas can be controlled by a combination of the ratios in gas flow rates and the sampler orifice and injector diameters. This can be used to optimize the sampling performance, depending on whether we want only the injector gas to enter the MS, or the injector gas accompanied by some auxiliary gas. The latter can be desired when the auxiliary gas also contains part of the sample ions (or ionic cloud). This is clearly explained by Houk and

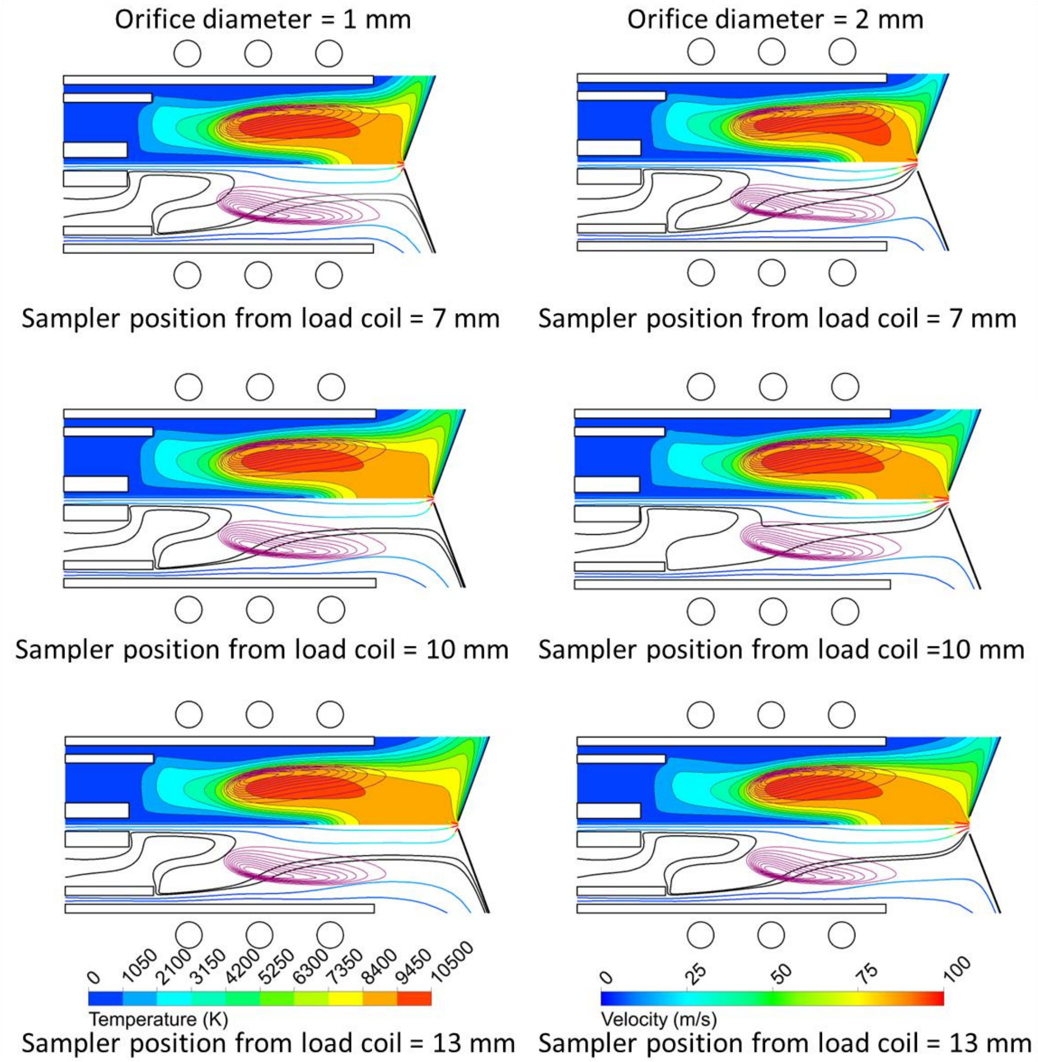

Figure 6.1: Effect of sampler position and orifice diameter: 2D plasma temperature profiles (upper frames) and velocity path lines (lower frames) for 1 mm (left column) and 2 mm (right column) orifice diameter, at a sampler position of 7 mm (first row), 10 mm (second row) and 13 mm (third row) distance from the load coil. Path lines originating from the injector and outer inlets are colored by velocity in m/s, whereas the path lines from the auxiliary gas are colored in black, to clearly distinguish between the different inlet gases. The red contours demonstrate the area of external power coupling. The injector gas, auxiliary gas and coolant gas flow rates are 1.0, 0.4 and 1.2 L/min, respectively, and the power is 1000W.

coworkers in [204]. They used a differential mobility analyzer electrostatic classifier to select particles in a specific size range from the laser ablation aerosol to be transported to the plasma. Specifically in Figure 3 in [204], they compared the size, position and trajectory of both small and large particles in the ICP torch. If an aerosol particle is sufficiently small (typically up to 150 nm in diameter), it will be efficiently vaporized and atomized along the central line. Larger particles are less extensively vaporized and atomized in the ICP torch. Also, their ion cloud position in the torch can be on or off axis. Therefore, depending on the size and the position of the ion cloud of large particles reaching the sampler cone, it is important whether the auxiliary flow can be extracted or not. In [205] Niemax also reported that the ion cloud diameter at the sampler orifice will be different, depending on the spatial position of the atomization. Larger droplets of analyte solution can penetrate deeper into the ICP than smaller droplets before they are desolvated and atomization of the analyte can start [205]. It means that the size of the analyte ion cloud from larger droplets is smaller at the position of the sampler, and probably it is sufficient when only the injector gas passes through the sampler orifice. On the other hand, for smaller droplets, the ion cloud becomes larger at the sampler position, and in this case it will be beneficial when (part of) the auxiliary gas can also be transported into the MS [205].

Furthermore, it is also seen from Figure 6.1 (especially at 13 mm distance from the load coil) that changes in the auxiliary gas flow path line profile also affect the plasma temperature profiles close to the sampler (see upper frames). Indeed, the auxiliary gas passes through the region of highest power coupling in the plasma (see purple contours in the lower frames), and will therefore be at higher plasma temperature than the injector gas. For an orifice diameter of 2 mm (right column), the auxiliary gas passes through the sampler orifice, and therefore the plasma temperature will be higher near the sampler orifice than in the case of 1 mm orifice diameter (left column), as is shown in Figure 6.1. Hence, the gas will pass through the sampler orifice with a higher plasma temperature, which helps to sustain the ions on their way to the detectors. Moreover, with a larger orifice, the cooling effect of the sampler is somewhat lower at the central axis (see also below). This might also have important consequences for the ICP sampling performance, because the gas flow which contains most of the sample ions is less affected by the interface cone.

Figure 6.2 shows the plasma temperature as a function of radial position for sample orifice diameters of 1 mm (black lines) and 2 mm (red lines), at a sampler position of 7 mm (solid lines), 10 mm (dashed lines), 13 mm (dotted lines) and 17 mm

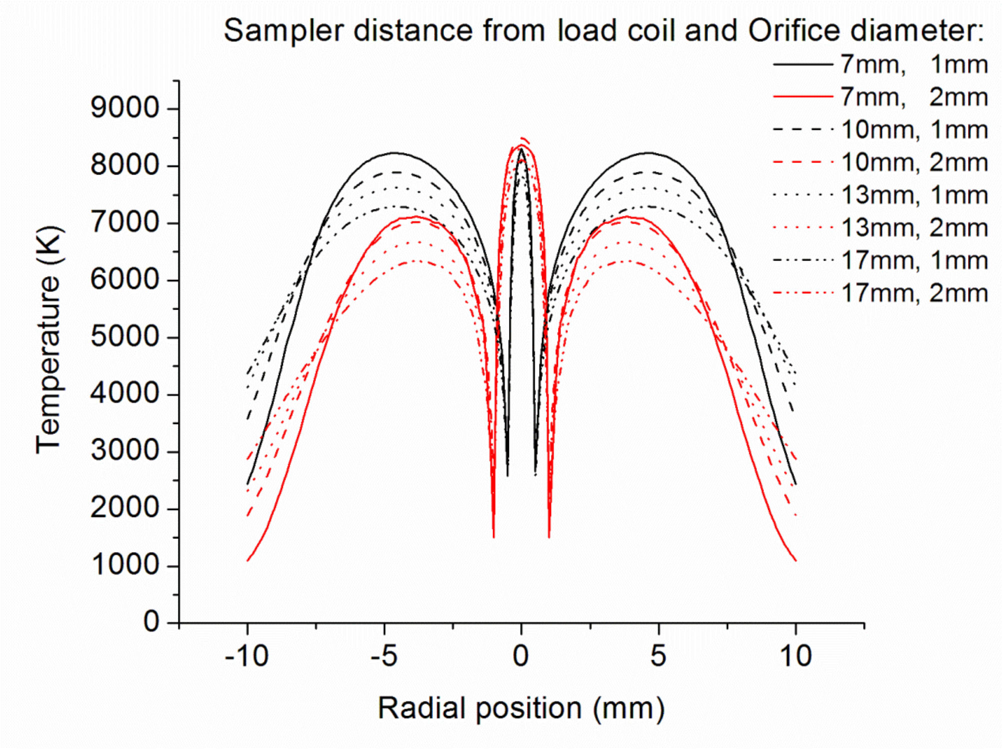

Figure 6.2: Effect of sampler position and orifice diameter: Radial distributions of plasma temperature (K) at the place of the sampler for sampler orifice diameters of 1 mm (black lines) and 2 mm (red lines), at a sampler position of 7 mm (solid lines), 10 mm (dashed lines), 13 mm (dotted lines) and 17 mm (dotted-dashed lines) distance from the load coil.

(dotted-dashed lines) from the load coil. It is shown that an increase in orifice diameter causes a slightly higher plasma temperature at the center and a clearly lower plasma temperature at the sides, which is explained by the change in the auxiliary gas flow path lines, illustrated in Figure 6.1 above. Indeed, the hotter auxiliary gas will exit through the sampler cone at 2 mm sampler orifice diameter, yielding a higher plasma temperature in the center, whereas at 1 mm sampler orifice diameter, it will flow out through the sides, resulting in a higher plasma temperature at the sides. Furthermore, an

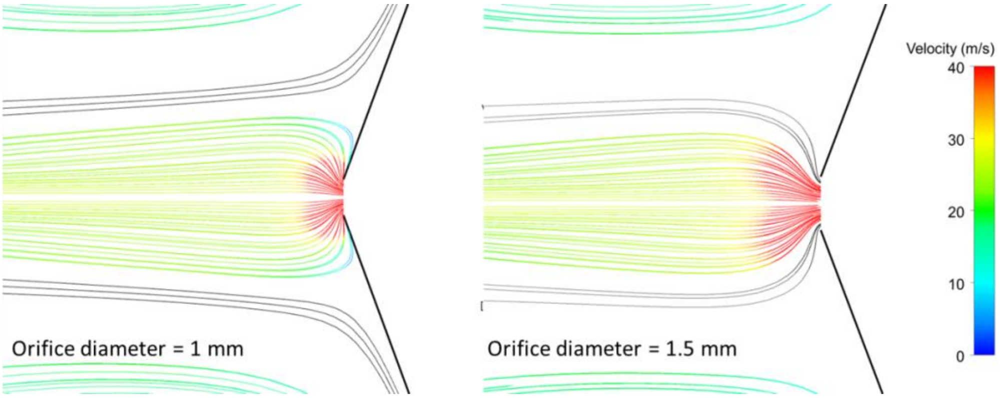

Figure 6.3: Effect of orifice diameter: 2D gas flow velocity path lines originating from the central and outer inlets, colored by velocity in m/s, and from the intermediate inlet, colored in black, close to the sampler, which is placed at 10 mm distance from the load coil with an orifice diameter of 1 mm (a) and 1.5 mm (b). The injector gas flow rate is taken as 1 (a) and 2.25 (b) L/min, to maintain the same ratio of injector gas flow rate to the surface area of the sampler orifice.

increase in sampler distance from the load coil leads to a lower plasma temperature at the sampler position, because the gas has more time to cool down by emitting radiation after leaving the torch. This drop in plasma temperature at increasing distance from the load coil was also reported by Hieftje and coworkers [109].

Figure 6.3 illustrates in detail the flow velocity path lines close to the sampler, with an orifice diameter of 1 mm (a) and 1.5 mm (b). Note that the injector gas flow rate is not the same in both Figures, i.e., it is equal to 1 L/min for the 1 mm orifice diameter (a), and 2.25 L/min for the 1.5 mm orifice diameter, so that the ratio of injector gas flow rate to the surface area of the sampler orifice is constant in both cases. It is seen in Figure 6.3 that in both cases the injector gas (colored) can exit through the orifice, as desired, but the interaction between the flow and the metal sampling cone is much more prominent in the case of the smaller orifice diameter (see Figure 6.3.a), leading to a somewhat lower flow velocity as well as more pronounced cooling of the gas. The latter will result in changes in the composition of the plasma gases that come in contact with the metal surface, i.e., a boundary layer of cooler gases will be formed along the surface of the metal. This effect was also described in literature. Indeed, Hayhurst et al. [206] stated that a larger orifice diameter results in a larger total flow rate into the sampler, which causes a reduction in boundary layer thickness. This would result in lower oxide levels for larger sampler orifice diameters, which was indeed observed [115]. Moreover, a large sampling orifice was not so easily clogged by concentrated solutions, and because the sampling orifice diameter was significantly larger than the thickness of the boundary layer formed on its edges, the bulk of the plasma flowing into the first vacuum stage had essentially the same composition as in the upstream plasma [118].

Finally, similar to Figure 6.1, we can again conclude from Figure 6.3.b that also in this case, i.e., diameter of central inlet equal to sampler orifice diameter, the auxiliary gas can exit through the sampler, even when the injector gas flow rate is higher than the auxiliary gas flow rate.

6.3. Electron number density and gas density

Figure 6.4 presents the radial electron number density profile at 8 mm from the load coil, for different places of the sampler, i.e. 10 mm (solid line), 13 mm (dashed line) and 17 mm (dotted line) distance from the load coil. The electron density in the central region drops slightly when the sampling position is reduced. Experimentally, Gamez et al. [109] and Macedone et al. [110] reported the same behavior for electron temperature and ion density, respectively. The explanation is of course logical, because in the case of the shorter sampling position (10 mm distance from the load coil) the distance between sampler and “measurement position” of electron density, i.e., 8mm, is only 2 mm, and the cooling of the plasma by the metal sampling cone will be more pronounced, resulting in a lower plasma temperature and hence lower electron density,

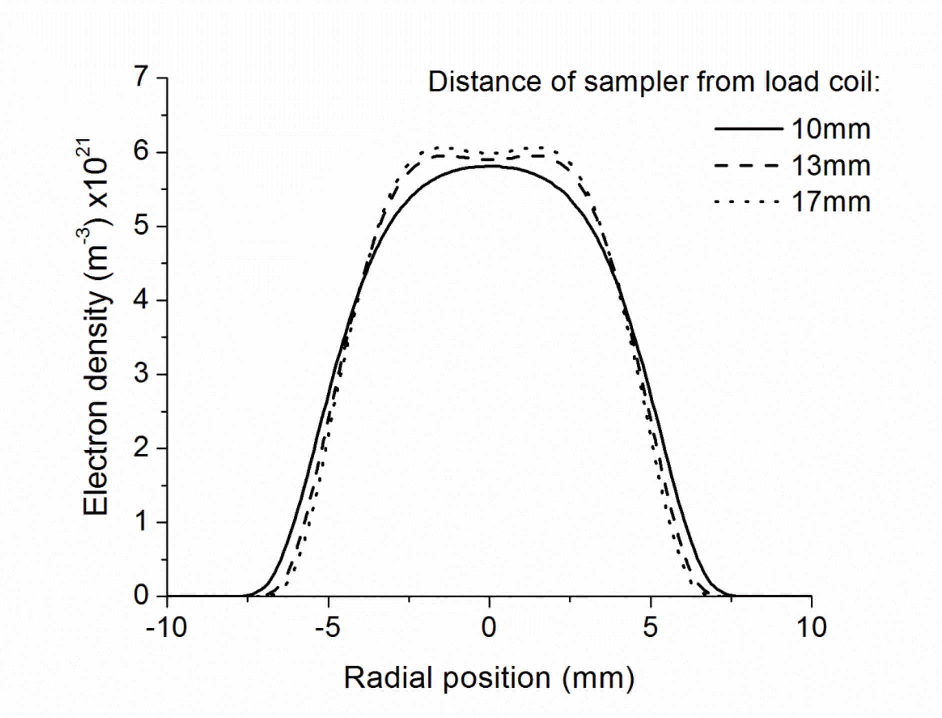

Figure 6.4: Effect of sampler position: Radial distributions of electron number density (m^{-3}) at 8 mm distance from the load coil, for different positions of the sampler, i.e. 10 mm (solid line), 13 mm (dashed line) and 17 mm (dotted line) distance from the load coil and a sampler orifice diameter of 1 mm.

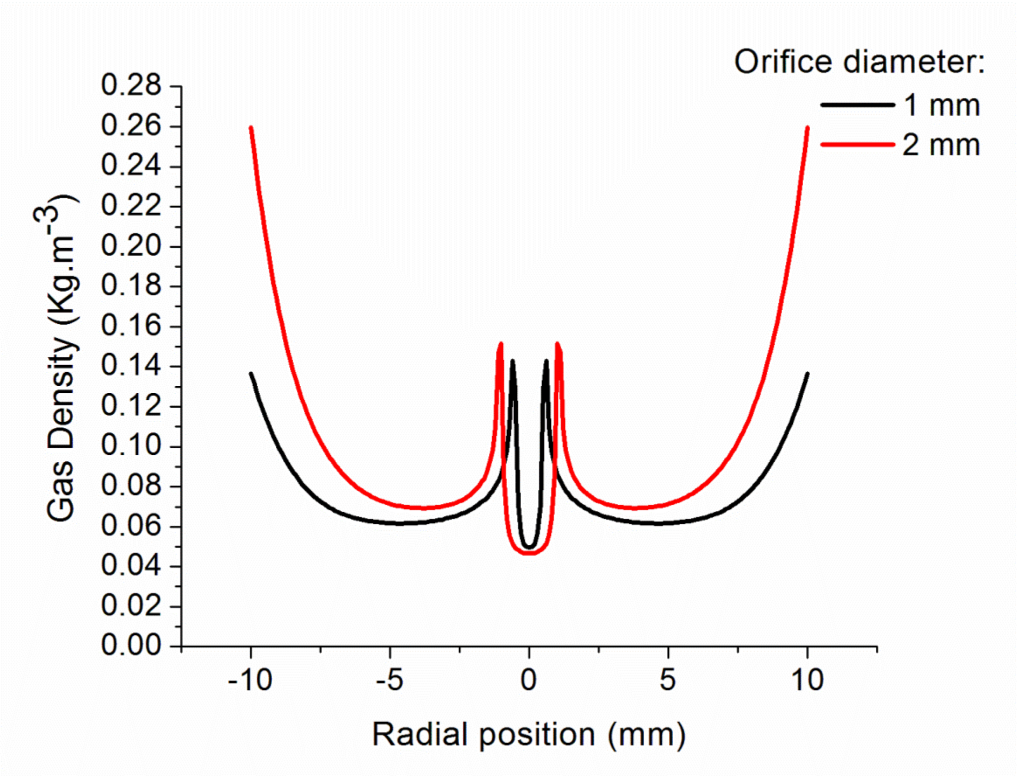

Figure 6.5: Effect of orifice diameter: Radial distributions of gas density (kg m^{-3}) for a sampler orifice diameter of 1 mm (black line) and 2 mm (red line), at a sampler position of 10 mm distance from the load coil.

than in the case of the larger sampling position, where the distance between sampling cone and "measurement position" is 9 mm, and hence the (cooling) effect of the sampling cone is less pronounced.

In Figure 6.5 the radial gas density profile is plotted at the position of the sampler, for the case of 10 mm distance from the load coil, with an orifice diameter of 1 mm (black line) and 2 mm (red line). R = 0 shows the center of the sampler orifice, or the central axis of the torch. In both cases, two maxima are observed close to the center, which indicate the edges of the sampler orifice, i.e. at R = 0.5 mm and R = 1 mm from the center in the black and red plots, respectively. To explain these density profiles, we refer to the plasma temperature profiles presented in Figure 6.2. At the center of the orifice, the plasma temperature has its maximum value and two pronounced drops are seen at both sides of it, indicating the edges of the sampler orifice. Indeed, the sampling cone temperature close to the orifice is around 550 K, so it cools down the gas (Figure

6.2), and following the ideal gas law, the density rises (Figure 6.5). The inverse relationship between plasma temperature and gas density profiles is indeed indicated by Figure 6.2 and Figure 6.5. At larger sampler orifice diameter, the cooling effect of the sampling cone in the center will be more moderate, resulting in a somewhat higher plasma temperature and somewhat lower gas density. Hence, the gas will pass the orifice with a somewhat higher plasma temperature and lower density.

6.4. Gas velocity

Figure 6.6 presents the 2D gas velocity distributions when the sampler cone is placed at 10 mm from the load coil and the orifice diameter is 1 mm (a) and 2 mm (b). A larger sampler orifice results in a larger gas flow velocity in the region close to the sampler. The acceleration of the gas is very prominent close to the sampler and the gas velocity changes strongly with position in this region. According to our calculation, at the place of the sampler, the plasma ions enter the MS with almost the same velocity in both cases. It means that the maximum value of the gas velocity exiting from the sampler is independent from the sampler orifice size. The value of the Mach number at the center of the orifice, where the flow has its maximum velocity, is around 0.6, and is found to be the same for both orifice sizes. It is mentioned also in [207] that the Mach number and velocity are independent from the size of the orifice. Moreover, the position of the sampler, also, does not exhibit any considerable effect on the gas velocity.

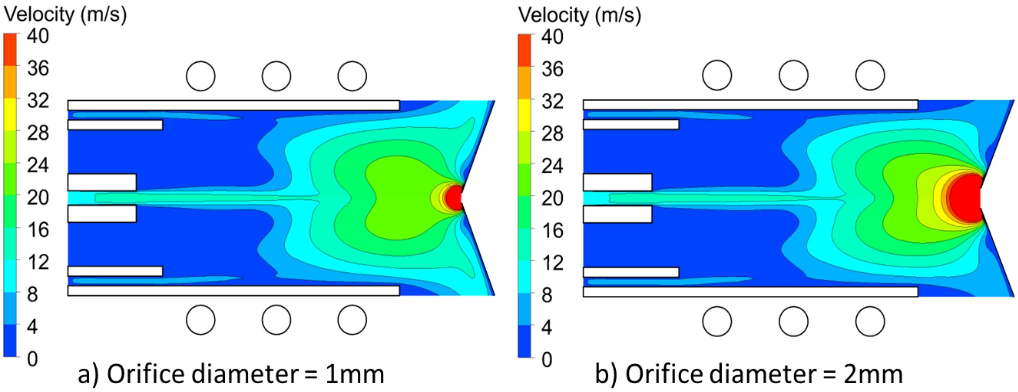

a) Orifice diameter = 1mm

b) Orifice diameter = 2mm

Figure 6.6: Effect of orifice diameter: 2D velocity profiles (m/s) for 1 mm (a) and 2 mm (b) orifice diameter, at the sampler position of 10 mm distance from the load coil.

6.5. Conclusion

We have computationally investigated the effect of distance of the sampler cone from the load coil and its orifice diameter on the plasma characteristics in an ICP connected to a MS, in order to obtain a better insight in the effect of these geometrical parameters on the analytical performance of ICP-MS. The fundamental plasma characteristics in the ICP upstream the sampler, calculated in this work, include the plasma temperature, electron number density, gas density and gas flow velocity.

Our calculations show that by increasing the sampler orifice diameter, the central plasma temperature at the place of the sampler rises slightly and consequently, the gas density reduces a bit, while the maximum of gas density occurs at the edges of the sampler. Furthermore, the gas passes through the sampler orifice with a velocity which is independent from the sampler orifice diameter.

From a zoomed picture of the velocity path lines close to the sampler, it is seen that the interaction of gas with the interface cone reduces by increasing the sampler orifice diameter, which causes a lower plasma temperature reduction at the place of the sampler cone and leads to more efficient gas transfer to the mass spectrometer.

Furthermore, our calculation results have demonstrated that the sampler orifice diameter should be equal to or larger than the central inlet diameter, to make sure that the auxiliary gas can also pass through the sampler orifice, which is desired when the ion cloud is large at the place of the sampler. On the other hand, to ensure that only the injector gas can enter the mass spectrometer, which is necessary to optimize the detection efficiency of the sample in the case when the ion cloud diameter is small, i.e., when the analyte ions are transported only by the injector gas, the sampler orifice diameter should be smaller than the central inlet diameter.

Finally, the plasma temperature at the place of the sampler decreases slightly at increasing distance of the sampler from the load coil, and at a fixed measurement position upstream the sampler, the electron density drops when the sampling position is reduced.

Chapter 7:

Recirculation in the ICP torch

The occurrence of recirculation of the auxiliary and injector gas flows is studied. The effects of operating parameters, i.e., applied power and gas flow rates, as well as geometrical parameters, i.e., sampler orifice diameter and central inlet diameter, are investigated. Our calculations predict that at higher applied power the auxiliary and injector gas flow inside the torch move more forward to the sampling cone, which is validated experimentally for the auxiliary gas flow. Furthermore, an increase of the gas flow rates can also modify the occurrence of recirculation. This is especially true for the injector gas flow rate, which has a more pronounced effect to reduce the backward motion than the flow rates of the auxiliary and coolant gas. Moreover, a larger sampler orifice (e.g., 2 mm instead of 1 mm) reduces the backward flow of the auxiliary gas path lines. Finally, a central inlet of 2 mm diameter causes more recirculation in the injector flow than a central inlet diameter of 1.5 mm, which can be avoided again by changing the operating parameters.

This chapter is based on the following publication: M. Aghaei, L. Flamigni, H. Lindner, D. Gunther, A. Bogaerts, Occurrence of gas flow rotational motion inside the ICP torch: A computational and experimental study, J. Anal. At. Spectrom. 29 (2014) 249-261.

7.1. Introduction

It was already demonstrated in the previous chapters that the auxiliary gas flow and even the injector gas flow do not always move in the forward direction inside the torch. This can be explained by the difference in velocities between the injector gas, auxiliary gas and coolant gas flows. According to the different initial flow rates, each flow moves with a different velocity. Note that each inlet has a specific area and especially the intermediate inlet is much wider than the central and outer inlets. This means that the auxiliary gas can enter more freely than the injector and coolant gas. As can be seen in Figure 7.1, the injector gas flow accelerates faster than the auxiliary gas flow. Therefore, a shear force [208,209] takes place between the faster injector gas flow and the slower auxiliary gas flow: $F = \eta A \frac{\partial v_x}{\partial r}$. Here η is the dynamic fluid viscosity, A is the area of contact, v_x is the axial velocity and r is the radial distance. A similar force exists between the faster coolant gas flow and the slower auxiliary gas flow. Indeed, as we can consider the flow as laminar, this force can be assumed to act between all laminar layers of the flow entering from the three different inlets with different flow rates. However, it should be noted that the auxiliary gas flow comes in contact earlier with the injector gas flow than with the coolant gas flow because of a difference in the length of the inlets. Therefore, the auxiliary gas flow is first affected by a shear force from the injector gas flow before it comes into contact with the coolant gas flow. When the coolant gas reaches the end of the auxiliary inlet, it also applies a shear force on the auxiliary gas flow and the overall result will be a backward turn and again a forward motion of the auxiliary gas flow. A similar behavior is sometimes observed for the injector gas flow (see below).

In this Chapter, we aim to obtain a better insight in the occurrence of the backward gas flows in the torch (i.e. recirculation) and to find parameters or operating conditions under which the recirculation of the flow can be controlled. It is a crucial issue especially for the injector gas flow. Indeed, the injector gas carries the sample through the torch and any deviation from the central axis leads to a longer transit time and a loss of intensity which should be avoided. Note that this is especially important after the particle evaporation has taken place [210]. Also, a deviation from the central axis would bring the sample particles to the outer region of the torch, thereby lowering the chance that the sample exits through the sampler. Hence, the detection efficiency becomes lower as some part of the sample is lost in the torch and not effectively sampled through the plasma-vacuum interface. It is therefore of crucial importance to know which parameters affect the recirculation inside the torch, and to what extent, as this knowledge will allow us to optimize the conditions needed to avoid recirculation inside the ICP torch. Note that in this chapter we only focus on the recirculation and not on ionization of the analyte. However, the ionization efficiency is also affected by the plasma conditions and this has a large influence on the analytical performance of ICP-MS as well, but this is beyond the scope of the present study.

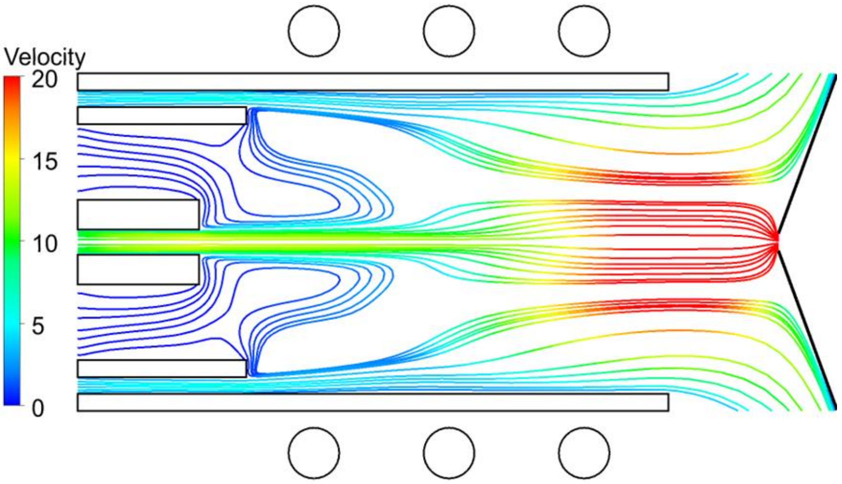

Figure 7.1: 2D gas flow velocity path lines originating from the central, intermediate and outer inlets, colored by velocity in m/s. The applied power is 1000 W. The injector gas, auxiliary gas and coolant gas flow rates are 1.0, 0.4 and 12 L/min, respectively. The central inlet diameter and sampler orifice diameter are 1.5 mm and 1.0 mm, respectively.

7.2. Recirculation in the auxiliary gas flow

When the auxiliary gas enters the torch, it typically does not go directly to the coil area. Indeed, in all the path line profiles we presented up to now, a similar behavior could be seen, characterized by a forward, then backward and again forward movement of the auxiliary gas. Experimental observations also suggest that such recirculation pattern inside the torch might occur (see below). However, by changing some operating parameters, which will be presented in this section, we found that it is possible to reduce or even remove the recirculation and to obtain a condition where the auxiliary gas only moves forward along the torch. It should, however, be noted that if the auxiliary gas goes very straight along the torch and does not pass through the area where the maximum power coupling occurs (see violet contours in Figure 7.2), the efficiency of heating in the ICP decreases substantially. This means that we should find the optimum condition at which no recirculation occurs and at the same time the auxiliary gas still follows a curved path along the torch, still passing through the efficient power coupling area. In other words, “forward curved” path lines along the torch are favorable. In this section, we try to reach this optimum condition by studying the effect of the different flow rates, power and sampler orifice diameter on the recirculation of the auxiliary gas flow. The central inlet diameter is kept fixed at 1.5 mm in this section.

7.2.1. Effect of injector gas flow rate

Figure 7.2 presents the 2D velocity path lines for fixed values of coolant gas and auxiliary gas flow rates, i.e., 12 and 0.4 L/min, respectively, while varying the injector gas flow rate as 1.0 (a), 1.4 (b) and 1.8 (c) L/min. Note that the conditions of Figure 7.2.a are the same as for Figure 7.1, but a lower number of path flow lines are depicted for the sake of clarity. Furthermore, only the auxiliary gas is shown with colored lines, and also the area of external power coupling is indicated. It can be seen from Figure 7.2.a that a strong recirculation occurs in the auxiliary gas flow when the injector gas flow rate is 1.0 L/min (see the colored lines). When increasing the injector gas flow rate to 1.4 L/min (Figure 7.2.b), a part of the auxiliary gas still shows backward flow but another part goes forward in the torch and does not turn backward.

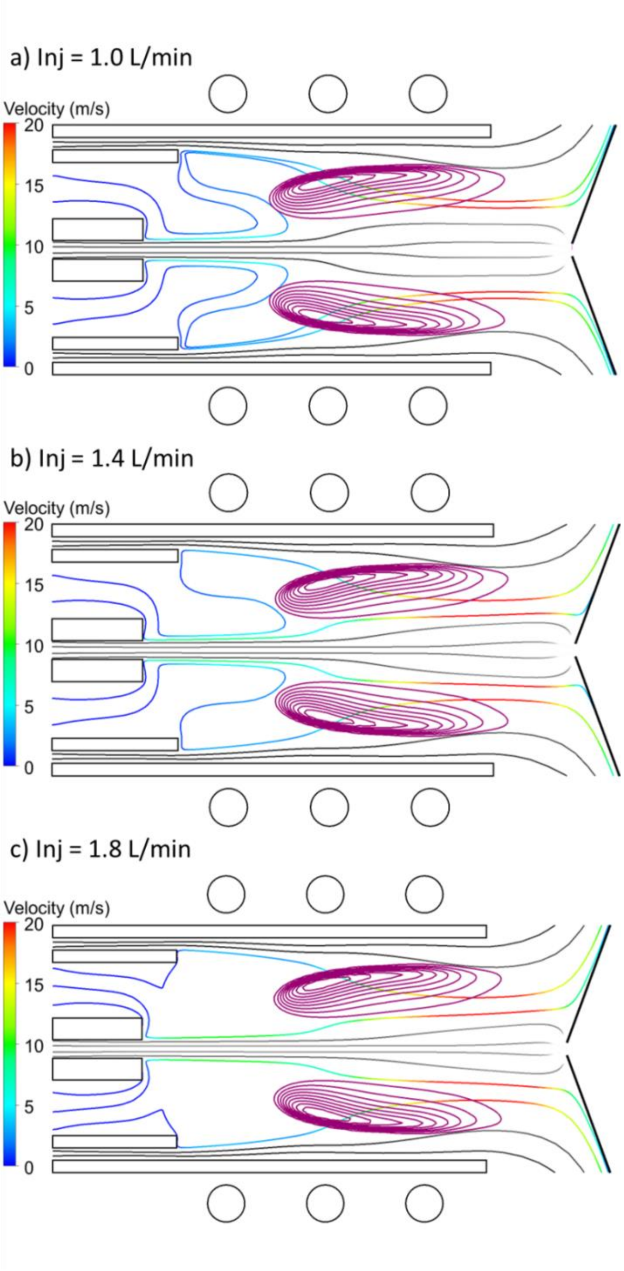

Figure 7.2: Effect of injector gas flow rate: 2D gas flow velocity path lines originating from the intermediate inlet, colored by velocity in m/s, as well as from the central and outer inlets, colored in black. The injector gas flow rate is 1 (a), 1.4 (b) and 1.8 (c) L/min, whereas the coolant and auxiliary gas flow rates are kept fixed at 12 and 0.4 L/min, respectively. The central inlet diameter and the sampler orifice diameter are 1.5 mm and 1.0 mm, respectively. The violet contours demonstrate the area of external power coupling.

When further increasing the injector gas flow rate to 1.8 L/min, no recirculation occurs in the torch (see Figure 7.2.c), i.e., the auxiliary gas only flows in the forward direction while it still passes through the area of maximum power coupling (violet contours). Hence, by applying high enough injector gas flow rates (i.e., 1.8 L/min when the auxiliary and coolant gas flow rates are 0.4 and 12 L/min) we can prevent the formation of recirculation inside the torch. Indeed, when comparing Figures 7.2.a-c, it can be seen that that by increasing the flow rate of the injector gas, which is accelerated toward the sampler due to the high pressure drop behind the sampler cone, the expansion of the injector gas flow is less pronounced and also starts further along the torch. This allows more auxiliary gas to reach the center and therefore the auxiliary gas flow can go more in the forward direction.

7.2.2. Effect of auxiliary gas flow rate

Figure 7.3 illustrates the flow path lines for a fixed coolant gas flow rate of 12 L/min, but varying the auxiliary gas flow rate and at the same time the injector gas flow rate, to avoid recirculation in the auxiliary gas. Our calculations predict that for the same coolant gas flow rate (12 L/min), there exists for each auxiliary gas flow rate a transition point for the injector gas flow rate to avoid recirculation in the auxiliary gas. This transition point rises with the value of the auxiliary gas flow rate. Indeed, at 0.4 L/min auxiliary gas flow rate, this transition point was observed at 1.8 L/min injector gas flow rate (cf. Figure 7.2 above), whereas it is found to be 2.0 L/min and 2.2 L/min for auxiliary gas flow rates of 0.6 and 0.8 L/min, respectively (see Figure 7.3).

It should be mentioned that an increase of the injector gas flow rate to higher values, while keeping the central inlet diameter fixed, causes the Reynolds number to exceed the critical value of 2300, which is considered to be the upper limit for assuming the flow as laminar in a pipe flow. The Reynolds number for the flows can be calculated from the following equation [208]:

$$\mathrm{Re} = \frac{\rho v d}{\eta}$$

where ρ is the flow mass density, v is the flow velocity, d is the diameter of the tube and η is the flow viscosity. The Reynolds number varies inside the ICP torch. For example, the Reynolds numbers for the conditions presented in Figure 7.2.a, 7.2.b and 7.2.c are 900, 1300 and 1600, at the central inlet while at the sampler they are 230, 270 and 360, respectively. The values for the conditions of Figure 7.3.a and 7.3.b at the injector inlet are 1900 and 2100, and at the sampler they are 460 and 580, respectively.

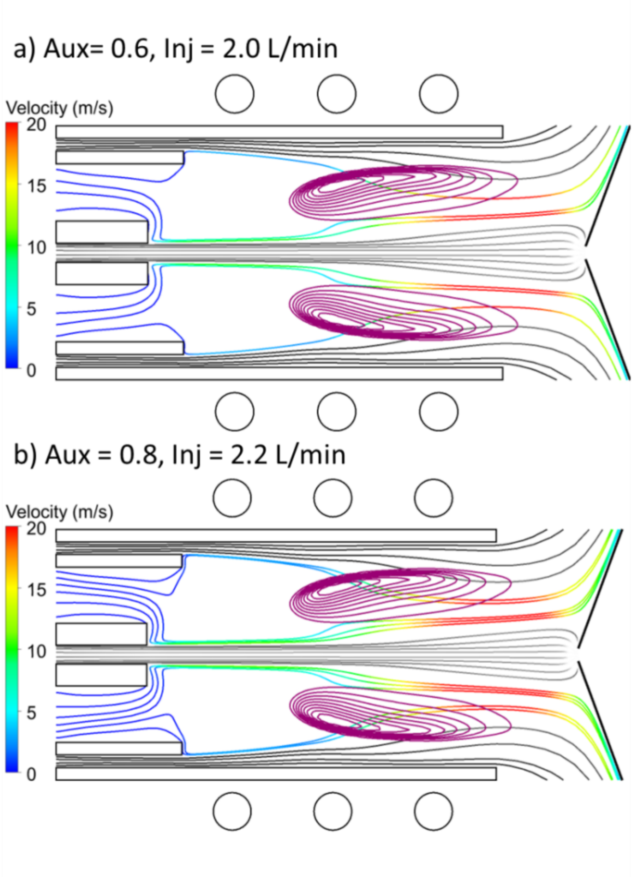

Figure 7.3: Effect of auxiliary and injector gas flow rates: 2D gas flow velocity path lines originating from the intermediate inlet, colored by velocity in m/s, as well as from the central and outer inlets, colored in black. The auxiliary and injector gas flow rates are taken as 0.6, 2.0 (a) and 0.8, 2.2 (b) L/min, respectively, whereas the coolant gas flow rate is kept fixed at 12 L/min. The central inlet diameter and the sampler orifice diameter are 1.5 mm and 1.0 mm, respectively. The violet contours demonstrate the area of external power coupling.

We performed the same calculation with an auxiliary gas flow rate of 1.0 L/min, in which the transient flow rate for the injector gas was 2.5 L/min. We did not show this result in Figure 7.3 as the Reynolds number exceeds the critical value of 2300, and hence the results are less precise as the assumption of the laminar regime is not valid anymore, although it should be mentioned that up to a Reynolds number of 4000, the flow is still in the transient regime and not in the turbulent regime.

7.2.3. Effect of coolant gas flow rate

For practical use of ICP-MS, commercial instruments sometimes do not allow to vary the injector gas and auxiliary gas flow rates in a wide range. If for instance 1.4 L/min and 0.4 L/min are acceptable and favorable values for the injector gas and auxiliary gas flow rates, this gives rise to recirculation in the auxiliary gas, when the coolant gas flow rate is 12 L/min, as is illustrated in Figure 7.2.b above. However, when increasing the coolant gas flow rate to 14 and 16 L/min, keeping the injector gas and auxiliary gas flow rates fixed, the recirculation in the auxiliary gas flow can also be reduced and even avoided, as can be seen from Figure 7.4. In Figure 7.4.a, some recirculation is still observed, but when the coolant gas flow rate is 16 L/min, as illustrated in Figure 7.4.b, the backward motion is avoided. Therefore, if experimentally we cannot increase the injector gas and auxiliary gas flow rates, we can still control the occurrence of recirculation of the auxiliary gas by varying the coolant gas flow rate. However, this gives rise to higher gas consumption. Furthermore, it is indicated that the effect of the coolant gas flow rate is minor compared to the effect of the injector gas flow rate. Indeed, the injector gas is much faster inside the torch due to the entrainment forces acting upon it, while the coolant gas exits more slowly from the open sides of the torch. Therefore, only 0.8 L/min increase in the injector gas flow rate (cf. Figure 7.2.a and c) can change the behavior of the auxiliary gas, while the coolant gas should increase by 4 L/min to have the same effect.

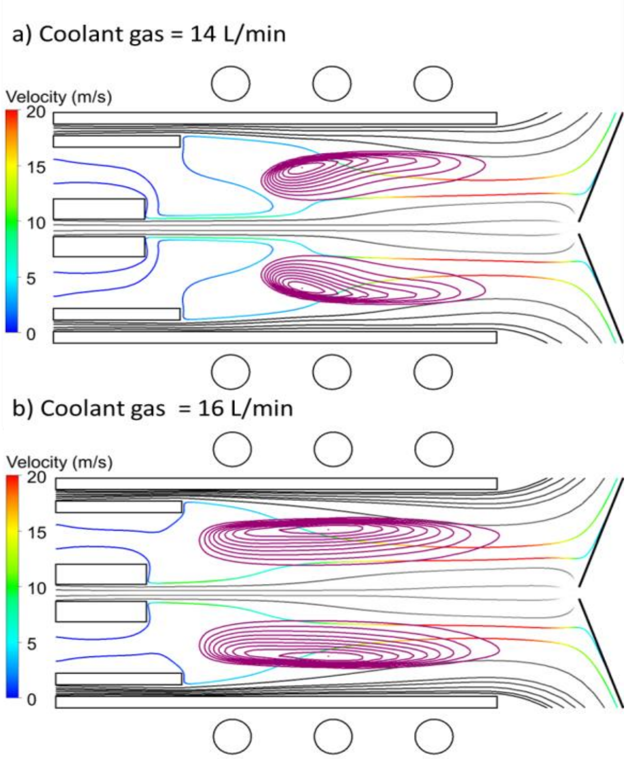

Figure 7.4: Effect of coolant gas flow rate: 2D gas flow velocity path lines originating from the intermediate inlet, colored by velocity in m/s, as well as from the central and outer inlets, colored in black. The coolant gas flow rate is taken as 14 (a) and 16 (b) L/min, whereas the injector gas and auxiliary gas flow rates are kept fixed at 1.4 and 0.4 L/min, respectively. The central inlet diameter and the sampler orifice diameter are 1.5 mm and 1.0 mm, respectively. The violet contours demonstrate the area of external power coupling.

7.2.4. Effect of applied power

Besides the gas flow rates, we found that the external power also has an effect on the recirculation of the auxiliary gas. Figure 7.5 shows the 2D velocity path lines with 12 L/min coolant gas, 0.4 L/min auxiliary gas and 1.0 L/min injector gas flow rates, at 750 W (a), 1000 W (b), 1250 W (c), and 1500 W (d) external power. Note that Figure 7.5.b corresponds to the condition of Figure 7.2.a. The effect of power on the fundamental plasma characteristics was discussed in detail in Chapter 5 (section 5.3).

Here we only focus on the presence of backward motion inside the torch. The external power seems to have a significant effect on the auxiliary gas flow pattern. In Figure 7.5.a (750 W), the auxiliary gas goes in the forward direction over a longer distance, before it turns backward, while in Figure 7.5.b (1000 W) and 7.5.c (1250 W), this “turn” occurs earlier, and finally at 1500 W (Figure 7.5.d) no backward flow is observed. Although the effect of external power is shown here to control the auxiliary gas movement inside the ICP torch, we do not recommend this condition of high power. Indeed, it is shown in Figure 7.5.d that the auxiliary gas, which is supposed to heat up the injector gas, does not pass through the area of efficient power coupling, whereas the coolant gas, which is meant for supporting the plasma and for cooling, now mostly receives the external energy and is heated up, which should be avoided due to a higher

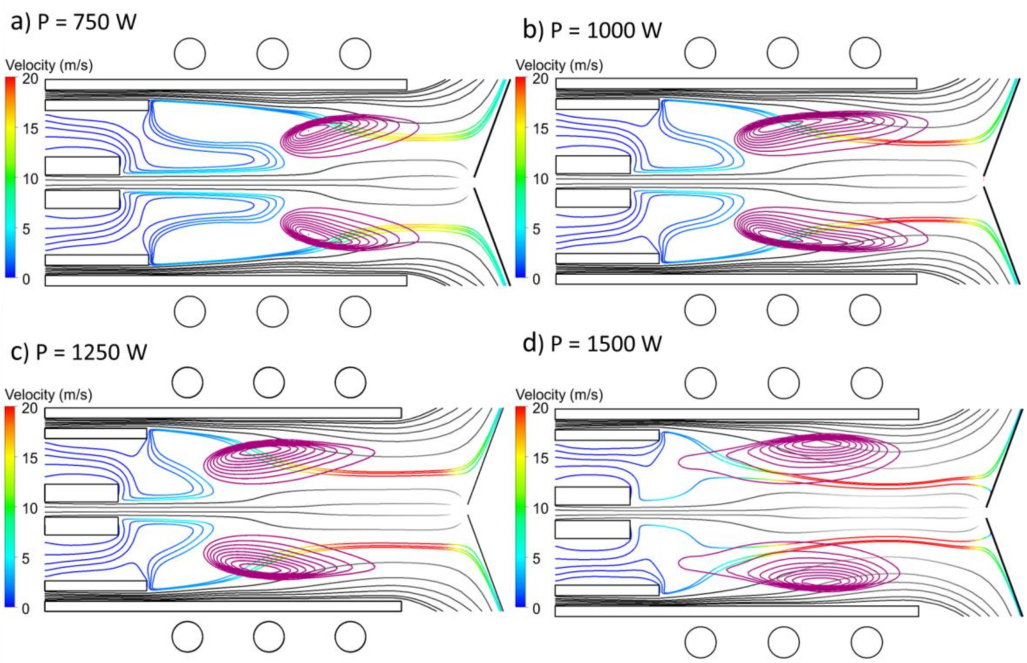

Figure 7.5: **Effect of applied power: 2D gas flow velocity path lines originating from the intermediate inlet, colored by velocity in m/s, as well as from the central and outer inlets, colored in black. The applied power is taken as 750 (a), 1000 (b), 1250 (c) and 1500 (d) W. The injector gas, auxiliary gas and coolant gas flow rates are 1.0, 0.4 and 12 L/min, respectively. The central inlet diameter and sampler orifice diameter are 1.5 mm and 1.0 mm, respectively. The violet contours demonstrate the area of external power coupling.**

risk of melting the torch and because of reducing the cooling efficiency. A more thorough discussion about applying 1500 W external power was provided in Chapter 5.

To validate our model predictions, we compared them with experimental data obtained at ETH-Zürich, by Günther and coworkers. For this purpose, an Elan 6000 ICP-MS (Perkin Elmer, Waltham, MA, USA) was used, and sodium chloride aerosols generated by laser ablation (LSX 500, Cetac Technologies, Omaha, NB, USA) were introduced to the ICP torch from the intermediate inlet instead of the central inlet. Figure 7.6 shows 2D images of the ICP torch with applied power of 800 W (first row) and 1400 W (second row). The injector gas only contains Ar, with a flow rate of 0.5 L/min (first column), 1.0 L/min (second column) and 1.5 L/min (third column) through an opening of 2 mm diameter. The auxiliary gas and coolant gas flow rates are kept fixed at 1.3 and 16 L/min, respectively. The sodium atomic emission line at 589 nm (shown in yellow) is captured using an ICCD camera [211] through an optical interference filter. Image processing is performed using Fiji [212] and ImageJ [213] which are software tools for microscopy. For each pixel composing the image, the maximum value is searched among 50 pictures of 5 ms exposure each, providing in this way information about all images at once. The plasma emission background is subtracted before evaluation. In this way, only the emission produced by the laser aerosol particles and introduced from the intermediate inlet is visible. In blue, the torch configuration before the experiment, i.e., without plasma and without interference filter, is shown.

Figure 7.6 illustrates a non-homogeneous distribution of the intensity (yellow) in the first row (800 W), between the first and second winding of the coil, which hints at whirls in this region. By increasing the applied power we can observe an improvement, i.e., less pronounced recirculation. Indeed, in the second row (1400 W), the region between the first and second winding of the coil is much smoother and there is no real evidence for a curved gas flow pattern. It is important to mention that experimentally we cannot be very sure about the exact values of the power that is actually applied, so Figure 7.6 can only reveal the qualitative effect of (low and high) power. Furthermore, the gas flow rates in the torch are also subject to uncertainties, since the mass flow controllers are not 100% accurate and the coolant gas flow rate cannot be controlled through the Elan 6000 ICP-MS software. For these reasons, we are not able to compare all the calculated conditions one-to-one with the experiments, but we rather discuss common trends. As mentioned above, each column in Figure 7.6 represents a different injector gas flow rate, but in all three cases, the recirculation can

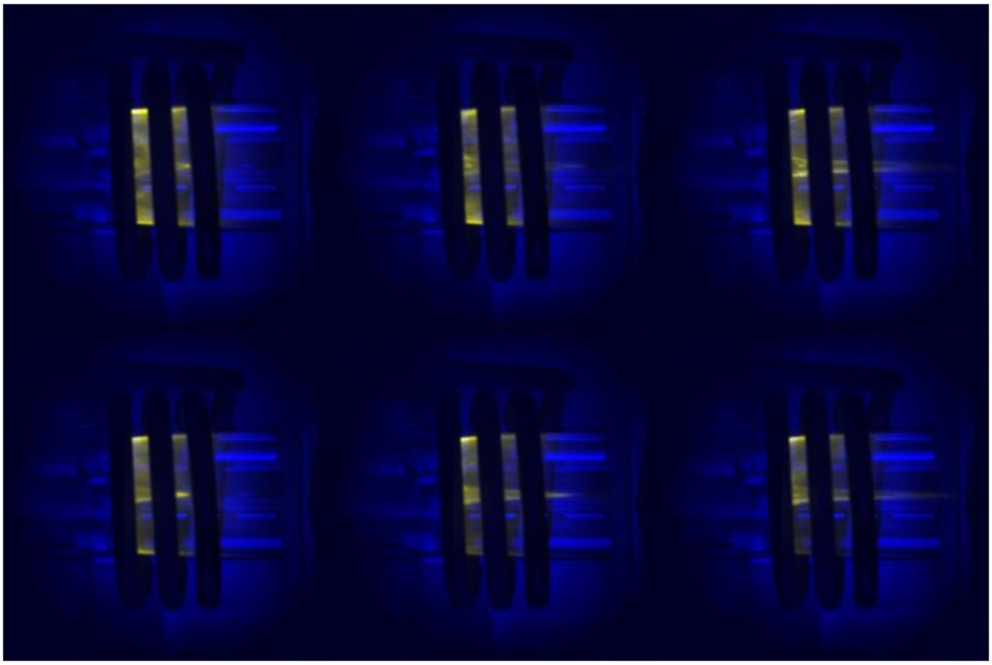

Figure 7.6: False-color images of background-corrected emission produced by sodium atom clouds (yellow) captured at low time resolution, overlaid on the image of the torch without plasma (blue). From left to right, the settings for the injector gas flow rate are: 0.5, 1, 1.5 L/min Ar. The first row was measured while applying 800 W, and the second row with 1400 W RF power.

be deduced from the intensity distribution. Indeed, it was mentioned in section 7.2.2 above that for each auxiliary gas flow rate there is a transition value of the injector gas flow rate beyond which no recirculation occurs anymore. As the auxiliary gas flow rate in this setup is fixed to 1.3 L/min, we expect this transition point to occur at much higher injector gas flow rates than the system allows, i.e., at least 2.5 L/min (cf. Figure 7.3.c above). This explains why we observe the recirculation for all injector gas flow rates used (i.e., 0.5, 1.0 and 1.5 L/min), as they are below 2.5 L/min. This is, at least, in qualitative agreement with our model predictions.

Figure 7.7 provides evidence that we are actually tracking particle clouds, which are distinctly visible at short integration times (compared to the particle travel time inside the plasma, which is in the order of a few milliseconds), but they will appear as soft lines at longer integration times due to motion and diffusion (Figure 7.6).

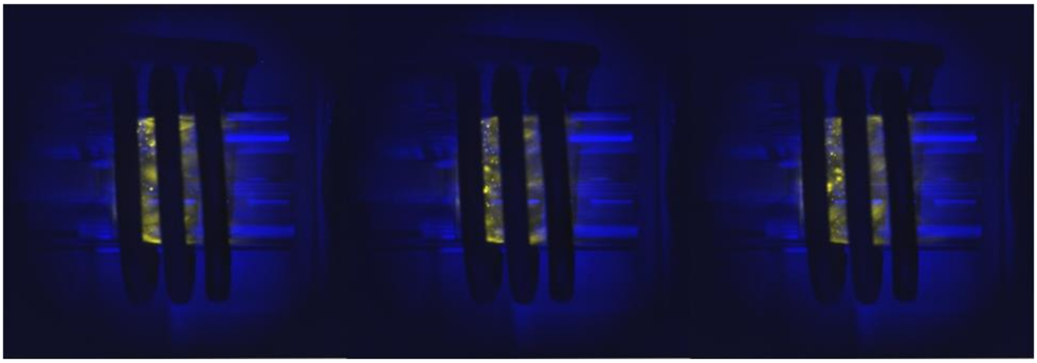

Figure 7.7: False-color images of background-corrected emission produced by sodium atom clouds (yellow) captured at high time resolution, overlaid on the image of the torch without plasma (blue). From left to right, the settings for the injector gas flow rate are: 0.5, 1, 1.5 L/min Ar. The applied RF power was 800 W.

The applied power in this case is 800 W and the injector gas flow rate is again 0.5 (left), 1.0 (middle) and 1.5 (right) L/min. The other measurement conditions are exactly the same as for Figure 7.6, except that 50 μs exposure time was used instead of 5 ms, so that no plasma emission background subtraction was necessary. The emission pattern in Figure 7.7 is indeed the same as in the upper row of Figure 7, but at long integration times (5 ms) the flight patterns are more visible due to the absence of strong localized emission clouds and due to the superposition of many movement tracks. In summary, it can be deduced from Figure 7.6 and 7.7 that (i) some recirculation may indeed occur in the auxiliary gas flow and (ii) this recirculation can be reduced, or even avoided, by increasing the applied rf power.

7.2.5. Effect of sampler orifice diameter

Besides the operating parameters, i.e., gas flow rates and applied power, our calculations predict that a change in the geometrical parameters can also affect the recirculation inside the ICP torch. Figure 7 .8 presents 2D velocity path lines for fixed values of coolant gas, auxiliary gas and injector gas flow rates, i.e., 12, 0.4 and 1.0 L/min, respectively, at an applied power of 1000 W, with sampler orifice diameters of 1 mm (a) and 2 mm (b). Note that Figure 7.8.a corresponds to Figure 7.2.a. It appears that the occurrence of strong recirculation (as in Figure 7.8.a) becomes less pronounced when the sampler cone has a larger orifice (Figure 7.8.b). This can be explained because with a larger sampler orifice, the auxiliary gas flow has the chance to enter the mass spectrometer, accompanying the injector gas flow, as was demonstrated in Chapter 6 (section 6.1). Consequently, the auxiliary gas flow is "sucked" toward the sampler orifice, thereby reducing the backward motion

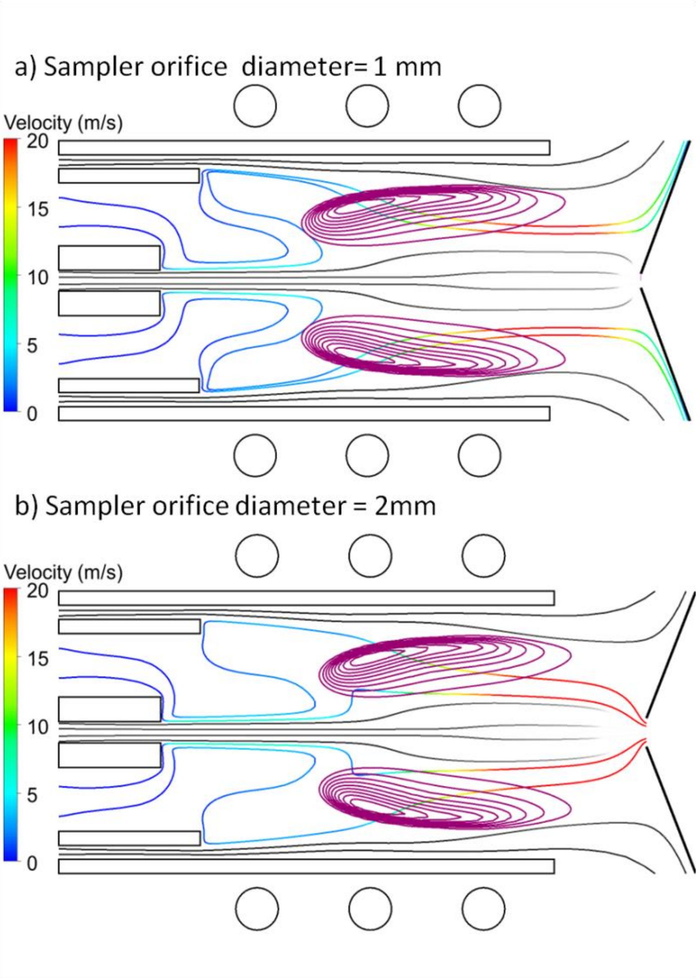

Figure 7.8: Effect of sampler orifice diameter: 2D gas flow velocity path lines originating from the intermediate inlet, colored by velocity in m/s, as well as from the central and outer inlets, colored in black. The sampler orifice diameter is taken as 1 (a) and 2 (b) mm. The injector gas, auxiliary gas and coolant gas flow rates are 1.0, 0.4 and 12 L/min, respectively. The central inlet diameter is 1.5 mm. The violet contours demonstrate the area of external power coupling.

7.3. Recirculation in the injector gas flow

Besides the auxiliary gas flow, the injector gas flow path lines might also exhibit some backward curved motion, depending on the central inlet diameter, which affects the early speed up of the injector gas flow compared to the other gas flows. This is even more crucial for the analytical performance of the ICP, as the sample particles are introduced from the central inlet, and they should be able to reach the sampler orifice, after atomization. Therefore, the current section is devoted to how the recirculation of the injector gas flow can be removed.

In this section, the effect of central inlet diameter, as well as of the different flow rates, on the recirculation of the injector gas flow pattern will be investigated. For this purpose, the central inlet diameter is increased from 1.5 mm to 2 mm, whereas the sampler orifice diameter is kept fixed at 1 mm. The new geometry is made by GAMBIT and read into FLUENT as described in Chapter 3.

Since the sample particles (or aerosols) are introduced from the central inlet, optimizing the injector gas flow path lines is crucial to guarantee that the introduced sample can reach the sampler orifice. As mentioned above, this implies that the ion cloud of the sample is led forward in the torch and along the central channel. Otherwise, when the ion cloud spreads out from the central channel due to diffusion, it may be possible to lose part of the sample, as it may follow the path lines which exit from the open sides of the torch instead of through the sampler orifice.

7.3.1. Effect of central inlet diameter

In section 7.2 the central inlet diameter was kept fixed at 1.5 mm, and in this case, the injector gas never exhibits a recirculation, at least for the wide range of conditions investigated by our model. However, when increasing the central inlet diameter to 2 mm, a drastic change in the injector gas flow path lines can be observed. Figure 7.9 shows 2D velocity path lines for the same operating parameters, i.e., 12, 0.4 and 1.0 L/min for the coolant gas, auxiliary gas and injector gas flow rates, respectively, and applied power of 1000 W, with the injector diameter of 1.5 mm (a) and 2 mm (b). Again Figure 7.9.a corresponds to Figure 7.2.a, but now the colored lines

a) Central inlet diameter = 1.5 mm

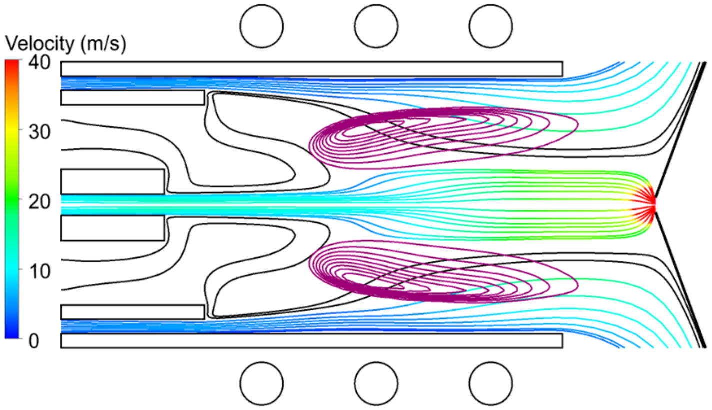

b) Central inlet diameter = 2 mm

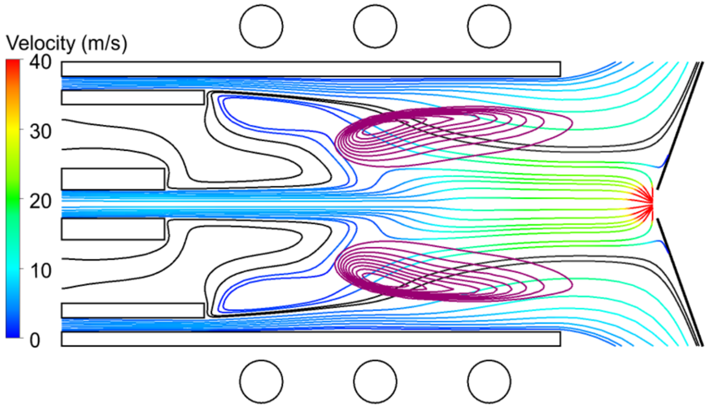

Figure 7.9: Effect of central inlet diameter: 2D gas flow velocity path lines originating from the central and outer inlets, colored by velocity in m/s, and from the intermediate inlet, colored in black. The central inlet diameter is taken as 1.5 (a) and 2.0 (b) mm, and the sampler orifice diameter is 1.0 mm. The injector gas, auxiliary gas and coolant gas flow rates are 1.0, 0.4 and 12 L/min, respectively. The violet contours demonstrate the area of external power coupling.

represent the injector gas and coolant gas flows, whereas the black lines show the auxiliary gas flow path lines. By comparing the velocity difference of the injector gas and coolant gas flow in Figure 7.9.a and b, it can be seen that by enlarging the central inlet diameter to 2 mm, the injector gas flow is no longer much faster than the coolant gas. As a result, the shear force from the coolant gas flow, which affects the auxiliary gas, could now also partly affect the injector gas flow. Hence, a larger central inlet diameter causes a change in the injector gas flow path lines, and a backward motion of the injector gas flow becomes apparent for an injector diameter of 2 mm. This is not favorable because if the introduced sample particles follow the backward lines, they may be lost in the torch and they cannot be effectively transferred to the mass spectrometer. Figure 7.9.b indeed shows that not all injector gas path lines are directed to the sampler orifice. Nevertheless, a central inlet diameter of 2 mm is quite common in ICP setups [214]. Therefore, in order to avoid this recirculation in the injector gas path lines, we performed several calculations for different operational parameters, as will be discussed in the following sections. It should be mentioned that Lindner et al. [181] discussed that for every central inlet diameter, there is a transition flow rate for the injector gas to achieve a central channel in the ICP torch. For example, for the central inlet diameter of 2 mm, the injector gas flow rate should exceed 0.4 L/min to make a central channel. In the current study, we meet that condition and hence there is a central channel at all conditions investigated, but still not all of the injector gas flow goes forward to the sampler orifice. Hence, in the present paper, after meeting the minimum criterion for obtaining a central channel, as discussed in [181], we define an additional minimum gas flow rate (i.e., higher than the minimum flow rate in [181]) to optimize the sample transfer by avoiding any backward motion in the injector flow.

7.3.2. Effect of injector gas flow rate

Figure 7.10 presents 2D velocity path lines for fixed values of coolant gas and auxiliary gas flow rates, i.e., 12 and 0.4 L/min, respectively, while varying the injector gas flow rate as 1.0 (a), 1.1 (b), 1.2 (c), 1.3 (d), and 1.6 (e) L/min. The injector gas flow is represented by colored lines, whereas the auxiliary gas is shown with black lines. The coolant gas flow path lines are omitted here, for the sake of clarity. As mentioned above, the central inlet diameter and sampler orifice diameter are kept fixed at 2 mm and 1 mm, respectively. It is shown in Figure 7.10 that a higher injector gas flow rate results in a gradual drop in the backward flows of the injector gas. The effect is most pronounced when the injector gas flow rate increases from 1.1 to 1.2 L/min (cf. Figure 7.10.b-c). When reaching 1.3 and especially 1.6 L/min injector gas flow rate, the recirculation has completely disappeared (see Figure 7.10.d-e).

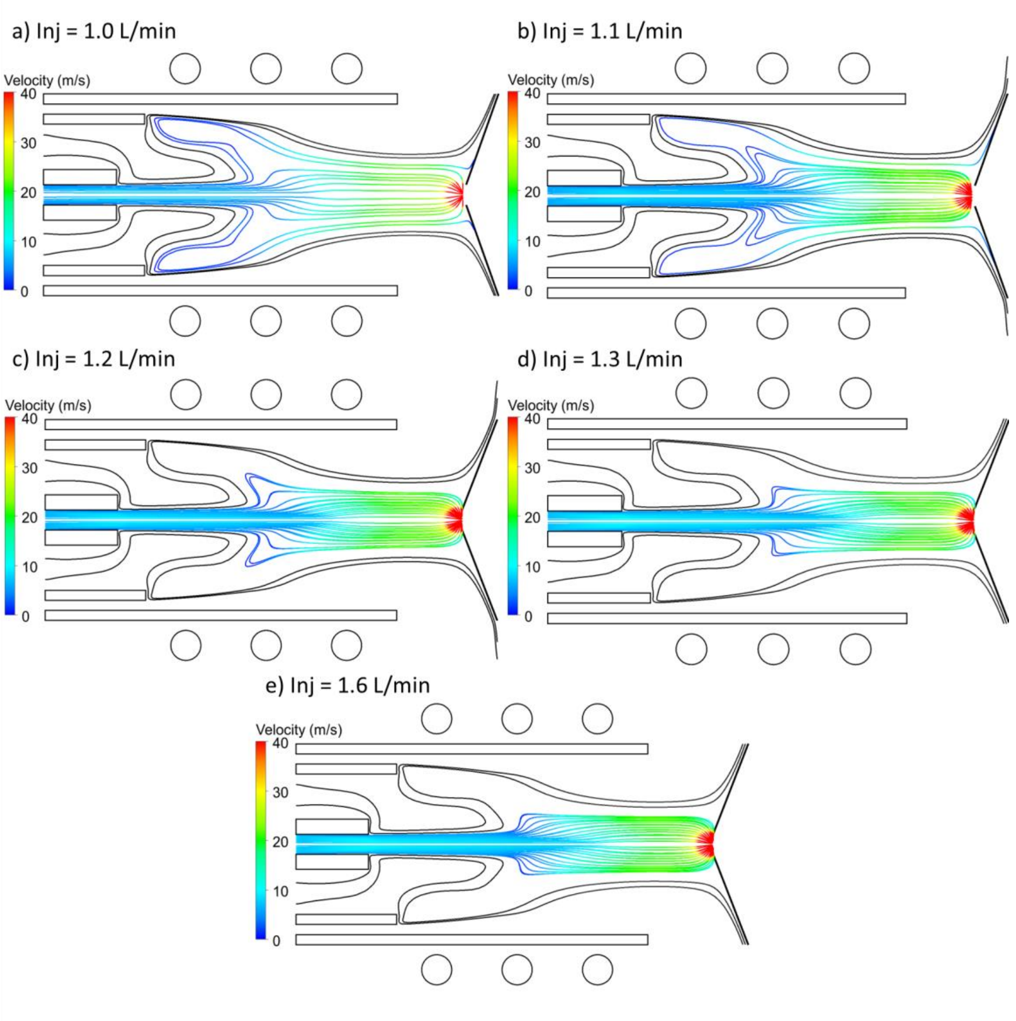

Figure 7.10: Effect of injector gas flow rate: 2D gas flow velocity path lines originating from the central inlet, colored by velocity in m/s, and from the intermediate inlet, colored in black. The coolant gas path lines are omitted for the sake of clarity. The injector gas flow rate is taken as 1 (a), 1.1 (b), 1.2 (c), 1.3 (d) and 1.6 (e) L/min. The coolant gas and auxiliary gas flow rates are 12 and 0.4 L/min, respectively. The central inlet diameter and sampler orifice diameter are 2.0 mm and 1.0 mm, respectively.

7.3.3. Effect of auxiliary gas flow rate

Figure 7.11 illustrates the flow path lines for fixed coolant gas and injector gas flow rates of 12 and 1.0 L/min, respectively, but varying the auxiliary gas flow rate from 0.4 (a) to 0.7 (b), 1.0 (c), 1.3 (d) and 2.0 (e) L/min. Note that Figure 7.11.a corresponds to Figure 7.10.a, but is repeated here for the sake of clarity. It is shown that by increasing the auxiliary gas flow rate from 0.4 to 0.7 L/min, the fraction of injector gas path lines which move backward has dropped (cf. Figure 7.11.a-b). For an auxiliary gas flow rate of 1.0 L/min (see Figure 7.11.c), the large backward recirculation has disappeared and only some deviation from the forward motion is observed. Our calculations predict that this deviation cannot be completely removed by increasing the auxiliary gas flow rate to 1.3 L/min (see Figure 7.11.d). We performed calculations for various auxiliary gas flow rates above 1.3 L/min, up to 2.0 L/min, but the flow pattern remained the same (cf. Figure 7.11.e). It can thus be concluded that in order to avoid recirculation in the injector gas flow, adjusting the auxiliary gas flow rate helps to some extent, but it is not as effective as changing the injector gas flow rate.

7.3.4. Effect of coolant gas flow rate

Figure 7.12 presents the 2D velocity path lines when increasing the coolant gas flow rates from 12 (a) to 14 (b), 16 (c) and 18 (d) L/min. The injector gas and auxiliary gas flow rates are kept fixed at 1.0 and 0.4 L/min, respectively. Note that Figure 7.12.a is the same as Figure 7.10.a and 7.11.a, for the sake of clarity. It is shown in Figure 7.12 that even the highest values of coolant gas flow rates investigated cannot make a significant change in the backward motion of the injector gas. Indeed, only a tiny improvement is observed in Figure 7.12.d. Therefore, in order to avoid the recirculation of the injector gas flow, we do not recommend changing the coolant gas flow rate. However, as discussed in section 7.2.3 above, the coolant gas flow rate does affect the recirculation of the auxiliary gas.

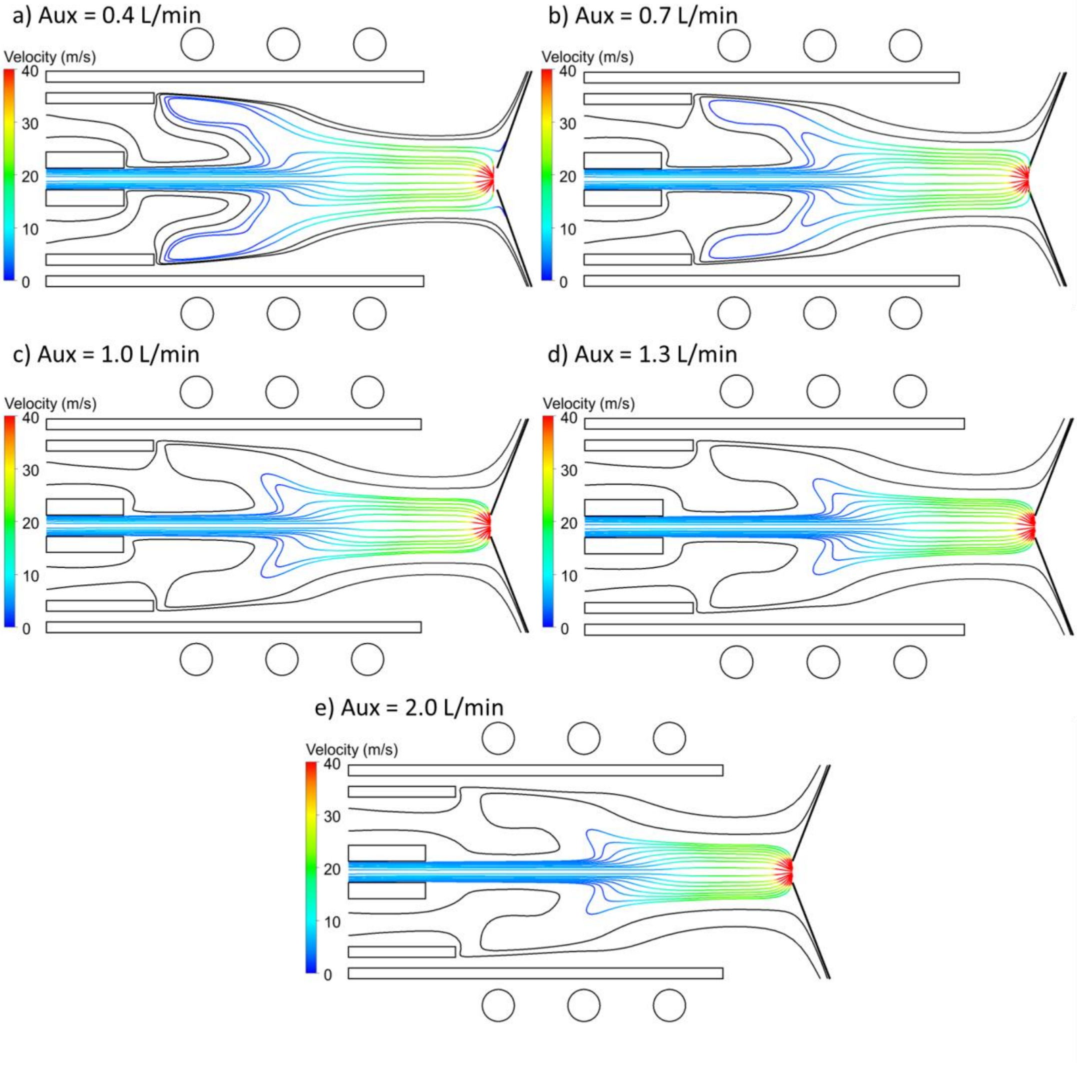

Figure 7.11: **Effect of auxiliary gas flow rate: 2D gas flow velocity path lines originating from the central inlet, colored by velocity in m/s, and from the intermediate inlet, colored in black. The coolant gas path lines are omitted for the sake of clarity. The auxiliary gas flow rate is taken as 0.4 (a), 0.7 (b), 1.0 (c), 1.3 (d) and 2.0 (e) L/min. The coolant gas and injector gas flow rates are 12 and 1.0 L/min, respectively. The central inlet diameter and sampler orifice diameter are 2.0 mm and 1.0 mm, respectively.**

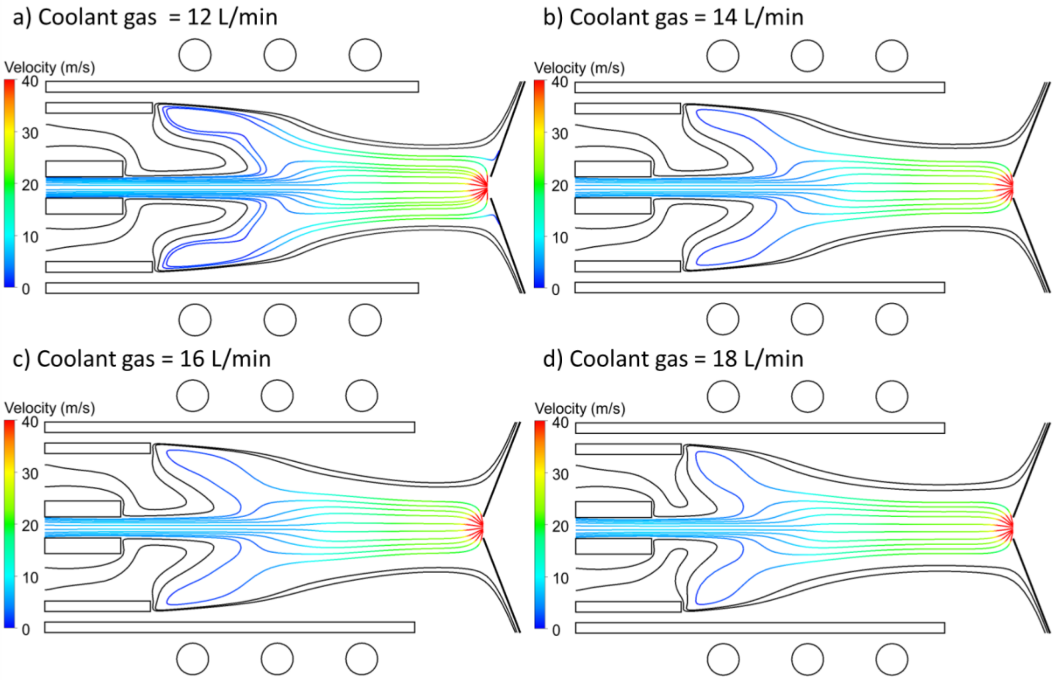

Figure 7.12: Effect of coolant gas flow rate: 2D gas flow velocity path lines originating from the central inlet, colored by velocity in m/s, and from the intermediate inlet, colored in black. The coolant gas path lines are omitted for the sake of clarity. The coolant gas flow rate is taken as 12 (a), 14 (b), 16 (c) and 18 (d) L/min. The injector gas and auxiliary gas flow rates are 1.0 and 0.4 L/min, respectively. The central inlet diameter and sampler orifice diameter are 2.0 mm and 1.0 mm, respectively.

7.3.5. Effect of applied power

Finally, we study the effect of applied power on the backward motion of the injector gas flow. Figure 7.13 shows 2D velocity path lines at 1000 (a) and 1200 (b) W. The coolant gas, auxiliary gas and injector gas flow rates are 12, 0.4 and 1.0 L/min, respectively. Hence, Figure 7.13.a is again the same as Figures 7.10.a, 7.11.a and 7.12.a, for the sake of clarity, except that now the area of external power coupling is added again (see violet contours). Figure 7.13.b illustrates that an increase of 200 W can improve the recirculation of the injector gas flow to some extent. Indeed, the

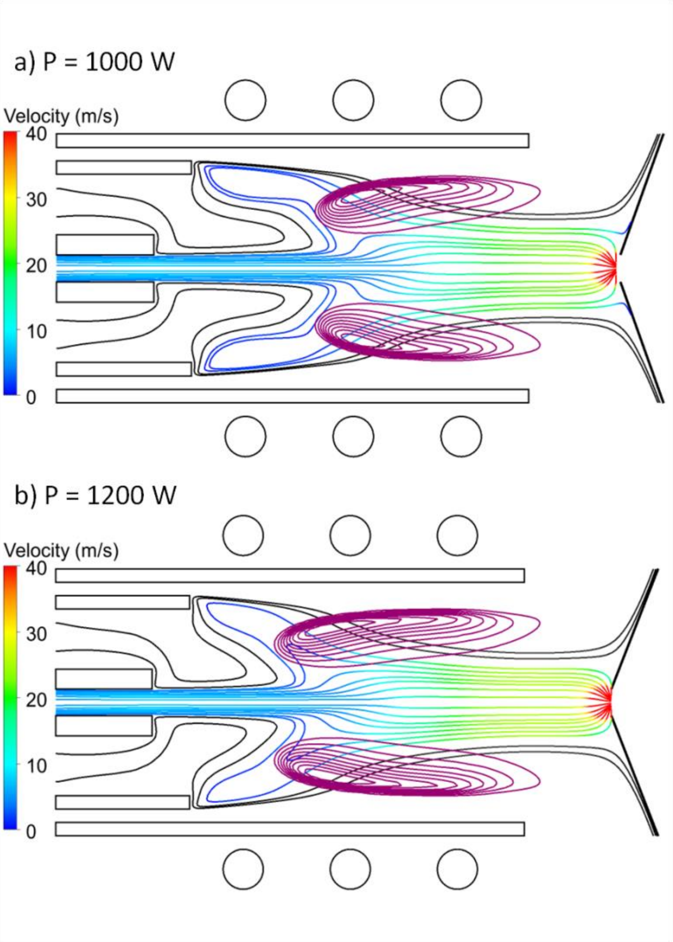

Figure 7.13: Effect of applied power: 2D gas flow velocity path lines originating from the central inlet, colored by velocity in m/s, and from the intermediate inlet, colored in black. The coolant gas path lines are omitted for the sake of clarity. The applied power is taken as 1000 (a) and 1200 (b) W. The injector gas, auxiliary gas and coolant gas flow rates are 1.0, 0.4 and 12 L/min, respectively. The central inlet diameter and sampler orifice diameter are 2.0 mm and 1.0 mm, respectively. The violet contours demonstrate the area of external power coupling.

recirculation is less pronounced, but it has not completely disappeared. Further increasing the applied power to e.g., 1400 W did not give rise to stable calculation results, at least for the gas flow rates and central inlet diameter under consideration here. Note that for 1.5 mm central inlet diameter, no problem occurred when assuming the same gas flow rates and a power as high as 1500 W (cf. Figure 7.5.d above).

To work with a higher applied power for an ICP torch fitted with a 2 mm injector diameter, we need to apply higher gas flow rates. This is illustrated in Figure 7.14, for 16, 1.2 and 1.2 L/min of coolant gas, auxiliary gas and injector gas flow rates, respectively. Note that the coolant gas flow path lines are now added again. The applied power is 1400 W and the central inlet diameter is 2 mm. These are typical conditions applied with the Elan 6000 ICP-MS. It is indeed visible that under this condition the injector gas flow does not move backward at all, and it can entirely transfer the introduced sample particles directly to the mass spectrometer.

It should be noted that in Figure 7.14, the absence of recirculation of the injector gas flow is due to an increase of both the applied power and the gas flow rates. We can thus consider Figure 7.14 as a result of all parameter effects that we discussed in this section, and which should be applied to avoid the occurrence of recirculation in the injector gas flow path lines.

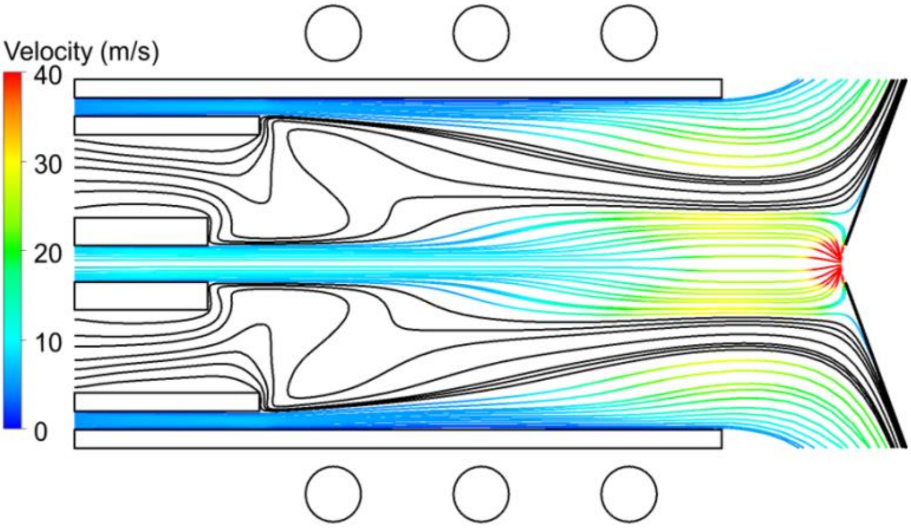

Figure 7.14: 2D gas flow velocity path lines originating from the central and outer inlets, colored by velocity in m/s, and from the intermediate inlet, colored in black. The applied power is taken as 1400 W. The injector gas, auxiliary gas and coolant gas flow rates are 1.2, 1.2 and 16 L/min, respectively. The central inlet diameter and sampler orifice diameter are 2.0 mm and 1.0 mm, respectively.

7.4. Conclusion

We have computationally investigated the occurrence of recirculation in the auxiliary and injector gas flow path lines, in order to obtain a better insight in the flow behavior inside the ICP torch and to optimize the transfer from the central inlets to the sampler orifice. The parameters which play a role to avoid these backward motions were investigated in detail.

Using 1.5 mm central inlet diameter typically results only in the occurrence of recirculation in the auxiliary gas flow path lines and not in the injector gas flow path lines. Our calculations predict that by increasing either the injector gas, auxiliary gas or coolant gas flow rates, or by raising the external power, we can control and avoid the backward motion of the auxiliary gas. Moreover, using a sampler with a larger orifice diameter also results in a drop in the recirculation of the auxiliary gas flow. This can all be explained by a lower shear force between the different gas flows. Our computational results were validated with experiments performed by Günther and coworkers on the Elan 6000 ICP-MS setup, and qualitative agreement was obtained for the effect of applied power. It has to be mentioned that it was not possible to validate the model predictions for the effect of gas flow rates and geometry due to experimental limitations.

Furthermore, our calculation results have demonstrated that by using a larger central inlet diameter, also the injector gas flow will exhibit some backward motion inside the torch, which is undesirable for sample transfer to the mass spectrometer. Similar as for the auxiliary gas, the backward motion in the injector gas flow could be reduced by applying higher injector gas, auxiliary gas or coolant gas flow rates and a higher applied power.

For both the auxiliary and the injector gas, it was found that a rise in the injector gas flow rate has a dominant effect on the occurrence of recirculation, and can thus be used as the most effective parameter to remove the backward flows inside the torch.

It needs to be mentioned that the importance of optimizing the auxiliary and injector gas path lines will become more clear when we can trace with our model the introduced sample material inside the torch. Indeed, due to different boiling and ionization temperatures of different materials, the position at which the sample or ion cloud may move in the radial direction to the outer region and become further away from the central channel is different [204,205]. Hence, it will be important to know exactly which path lines they follow. Moreover, in the future, the optimization of the gas flow motion, which is focused on in the current Chapter, will have to be combined with signal intensity optimization, which is currently not considered. Indeed, note that an increase in the injector gas flow rate can lead to low signal intensities because a lower amount of analyte will get ionized due to the high gas flow rate and the low temperature in the plasma. This effect can be studied when the particle tracing will be added to the current model. Nevertheless, the study carried out in the present Chapter can already explain where the sample might get lost and it can predict the parameters which might help to reduce these losses.

Chapter 8:

Outlook for future work

In this chapter, the next plans after (and based on) this PhD work are briefly presented.

During this PhD work, a model for an ICP torch connected to a MS interface is developed in which the plasma flow dynamics as well as ionization are taken into account. The model describes all the plasma characteristics inside an ICP torch, but there is no sample introduction included yet. To improve ICP-MS as an analytical method, a more fundamental insight in the behavior of the introduced sample material in the plasma is needed. Therefore, the introduction of sample particles/droplets in the ICP torch and a detailed investigation of the interaction of the sample material with the plasma should be the next step to improve our understanding of ICP-MS. The model presented in this PhD work forms the ideal starting point for such a model development.

The analyte is typically introduced into the ICP via a spray of dilute aqueous solution. Indeed, the particle in liquid phase will undergo heating, vaporization and boiling and finally ionization. Any droplet that has not undergone these processes will result in signal loss. Moreover, chemical reactions will take place between the dissolved element and species originating from the water, which also need to be described in the future model. Therefore, the equations used in this model need to be extended. Moreover, for any injected material, several material parameters are needed, both in liquid phase (i.e., as droplets) and in gas phase (i.e., after vaporization). Some parameters, i.e., the viscosity, thermal conductivity and diffusion coefficients, are a function of the local gas composition and plasma temperature, and need to be inserted in the model as UDFs. It might not be easy to find all parameters in literature. It will therefore be important to validate my results with experiments, by working in close collaboration with experimental groups. There are several groups working on fundamental aspects of the ICP, such as the group of Prof. Colombo (Bologna, Italy), Prof. Hieftje (Bloomington, Indiana, US), Prof. Günther (Zürich, Switzerland), Prof. Olesik (Columbus, Ohio, US), Prof. Farnsworth (Provo, Utah, US) and Prof. Sharp (Loughborough, UK) and there is mutual interest to start up/continue such a collaboration. When the model includes sample introduction, it should be ready to be applied for every operating and geometrical condition used in different laboratories. Moreover, extension of the model to three dimensions will also be a future step, to increase the accuracy of our modeling study.

Summary

Inductively Coupled Plasma Mass Spectrometry (ICP-MS) is one of the most important modern atomic spectrometry techniques. It is a being applied for the determination of trace, minor and major elements in almost every analytical field. Strengths of the technique include a wide elemental coverage (including alkali and alkaline earth elements, transition and other metals, metalloids, rare earth elements, most of the halogens and some of the non-metals), a high sensitivity and low background signals, which yields very low detection limits (sub-ng/L – parts-per-trillion (ppt) in most cases), fast analysis times and isotopic information. These capabilities explain the widespread interest and acceptance of ICP-MS across all industry types, and confirm the status of ICP-MS as the premier technique for the measurement of trace metals.

To improve the analytical applications, fundamental studies of the ICP-MS are indispensable. Therefore, the goal of this work is to obtain a better understanding of the underlying physics of an ICP torch connected to a MS interface, by means of computer simulations and to provide insight into how the operating conditions and geometry can be optimized.

The ICP model developed and applied for this investigation is explained in **Chapter 2** and **Chapter 3**. The model is based on solving partial differential equations for the gas flow dynamics coupled with the energy conservation and Maxwell equations. The power coupling into the ICP is a source term in the energy conservation equation, whereas the emitted radiation is treated as a loss term. This model is built within the commercial computational fluid dynamics (CFD) program FLUENT (ANSYS). Some self-written codes were added as user defined functions (UDFs), in order to calculate the electromagnetic fields, the amount of ionization, as well as the material parameters, i.e., viscosity, heat capacity, thermal conductivity and diffusion coefficients as a function of the actual gas composition and plasma temperature. Typical calculation results from the model include the gas flow behavior, as well as the plasma temperature and electron density profiles. The general hypotheses used to build up the model are: (a) the gas flow is laminar, (b) the plasma has a 2D axisymmetric geometry and (c) the model assumes local thermodynamic equilibrium (LTE).

In **Chapter 4**, the effect of the presence of a mass spectrometer sampling interface on the fundamental plasma characteristics in ICP-MS is illustrated. To investigate the effects of the sampler, two sets of calculations with exactly the same conditions, with and without the sampler, are performed. Typical plasma characteristics, such as gas flow velocity, plasma temperature and electron density, are calculated in two dimensions (cylindrical symmetry) and compared with and without the sampler. The results indicate a dramatic increase in the plasma velocity in the region close to the interface. Furthermore, a cooled metal interface lowers the plasma temperature and electron density on the axial channel very close to the sampling cone but the corresponding values in the off axial regions are increased. Therefore, the effect of the interface strongly depends on the measurement position. It is shown that even a small shift from the actual position of the sampler leads to a considerable change of the results. The calculation results are compared with measured data from literature and reasonable agreement is reached. The results provide a better insight in the underlying physics responsible for the effect of the sampling interface.

In **Chapter 5**, the effects of typical operating conditions on the upstream plasma characteristics of the ICP in contact with a MS interface are investigated. Thus, different injector gas and auxiliary gas flow rates are applied in a wide range. Moreover, the effect of the forward power is studied in detail. There seems to be an optimum range of injector gas flow rates for each setup which guarantees the presence and also a proper length of the central channel in the torch. Moreover, our modeling results show that for any specific purpose, it is possible to control that either only the injector gas flow passes through the sampling orifice or that it is accompanied by the auxiliary gas flow. Depending on the size of the sample ion cloud, the one or the other condition is favored. It was also found that depending on the geometry, the variation of outgoing gas flow rate is much less than the variation of the injector gas flow rate and this causes a slightly higher pressure inside the torch. The general effect of increasing the applied power is a rise in the plasma temperature, which results in a higher ionization in the coil region. However, the negative effect is reducing the length of the cool central channel which is important to transfer the sample substances to the sampler. Using a proper applied power can enhance the efficiency of the system. Indeed, by changing the gas flow path lines, the power can control which flow (i.e., only from the injector gas or also from the auxiliary gas) goes through the sampler orifice. The calculation results are compared with measured data from literature, and good qualitative agreement is obtained.

Subsequently, in **Chapter 6**, the effects of sampler orifice diameter (ranging from 1 to 2 mm) and distance of sampler cone from the load coil (ranging from 7 to 17 mm) are studied. An increase in sampler orifice diameter leads to a higher central plasma temperature at the place of the sampler, as well as a more efficient gas transfer through the sampler, by reducing the interaction of the plasma gas with the sampling cone. However, the flow velocity at the sampler position is found to be independent from the sampler orifice diameter. Moreover, by changing the sampler orifice diameter, we can control whether only the injector gas or also the auxiliary gas can exit through the sampler. Finally, at increasing distance of the sampler from the load coil, the plasma temperature at the place of the sampler decreases slightly, which might also have consequences for the ion generation and transport through the sampling cone. The calculation results are again in reasonable agreement with measured data from literature.

Finally, in **Chapter 7**, the occurrence of recirculation of the auxiliary and injector gas flows is studied. The effects of operating parameters, i.e., applied power and gas flow rates, as well as geometrical parameters, i.e., sampler orifice diameter and injector inlet diameter, are investigated. Our calculations predict that at higher applied power the auxiliary and injector gas flow inside the torch move more forward to the sampling cone, which is validated for the auxiliary gas flow by experiments performed by Günther and coworkers at ETH-Zürich. Furthermore, an increase of the various gas flow rates can also modify the occurrence of recirculation. This is especially true for the injector gas flow rate, which has a more pronounced effect to reduce the backward motion than the flow rates of the auxiliary and coolant gas. Moreover, a larger sampler orifice (e.g., 2 mm instead of 1 mm) reduces the backward flow of the auxiliary gas path lines. Finally, a central inlet of 2 mm diameter causes more recirculation in the injector gas flow than a central inlet diameter of 1.5 mm, which can be avoided again by changing the operating parameters.

In conclusion, the studies performed during this PhD work contribute to a better understanding of the fundamental mechanisms of the ICP, and we hope that this will improve the analytical performance of ICP-MS. In future work, we plan to include the introduction of sample particles/droplets in the ICP torch, as is briefly outlined in **Chapter 8**. The model presented in this PhD work forms the ideal starting point for such a model development.

Samenvatting

Inductief gekoppelde plasma massaspectrometrie (Eng: Inductively Coupled Plasma Mass Spectrometry; ICP-MS) is één van de belangrijkste technieken in de moderne atoomspectrometrie. Het wordt gebruikt voor de bepaling van (sporen)elementen in bijna elk analytisch domein. De sterke punten van deze techniek omvatten een brede toepasbaarheid in de te meten elementen (inclusief alkali en aardalkali elementen, transitiemetalen en andere metalen, metalloïden, zelfdzame aarden, de meeste halogenen en ook sommige niet-metalen), een hoge gevoeligheid en een lage achtergrond, die zeer lage detectielimieten geven (sub-ng/L – parts-per-trillion (ppt) in de meeste gevallen), snelle analysetijden en isotoop-informatie. Deze eigenschappen verklaren de grote interesse en acceptatiegraad van ICP-MS in alle types van industrie, en ze bevestigen de status van ICP-MS als dé techniek bij uitstek voor het meten van sporen-metalen.

Om de analytische toepassingen te verbeteren zijn fundamentele studies van ICP-MS onontbeerlijk. Het doel van dit werk is dus om een beter begrip te krijgen van de onderliggende fysica van een ICP toorts in contact met een MS interface, door middel van computersimulaties, en om inzicht te verschaffen in hoe de werkomstandigheden en de geometrie kunnen geoptimaliseerd worden.

Het ICP model dat ontwikkeld en toegepast werd voor deze studie, wordt uitgelegd in **Hoofdstuk 2** en **Hoofdstuk 3**. Het model is gebaseerd op het oplossen van partiële differentiaalvergelijkingen voor de gasstromingsdynamica, gekoppeld aan de vergelijking voor energiebehoud en de Maxwell vergelijkingen. De vermogenstoevoer in het ICP is een bronterm in de energiebehoudsvergelijking, terwijl de uitgezonden straling als een verliesterm in rekening wordt gebracht. Het model is opgebouwd met het commerciële computationele fluid dynamica (CFD) programma FLUENT (ANSYS). Een aantal zelfgeschreven codes werden hieraan toegevoegd als “user defined functions” (UDFs), om de elektromagnetische velden en de hoeveelheid ionizatie te berekenen, alsook de materiaalparameters, d.w.z, viscositeit, warmtecapaciteit, thermische geleidbaarheid en diffusiecoëfficiënten in functie van de actuele gassamenstelling en plasmatemperatuur. Typische berekeningsresultaten van het model omvatten de gasstroming, alsook de profielen van plasmatemperatuur en elektronendichtheid. De algemene hypotheses gebruikt om het model op te bouwen, zijn: (a) de gasstroming is laminair, (b) het plasma heeft een 2D axisymmetrische geometrie en (c) het model veronderstelt lokaal thermodynamisch evenwicht (LTE).

In **Hoofdstuk 4** worden de effecten van de aanwezigheid van een interface naar de massaspectrometer (de zgn. “sampler”) op de fundamentele plasmakarakteristieken in ICP-MS geïllustreerd. Om de effecten van de sampler te onderzoeken worden twee sets van berekeningen uitgevoerd met exact dezelfde voorwaarden, met en zonder sampler. Typische plasmakarakteristieken, zoals de gasstromingssnelheid, de plasmatemperatuur en de elektronendichtheid, worden berekend in twee dimensies (cylindrische symmetrie) en vergeleken met en zonder sampler. De resultaten tonen een opvallende stijging in de plasmasnelheid in de zone vlakbij de interface. De koude metalen interface verlaagt bovendien de plasmatemperatuur en de elektronendichtheid op de centrale as vlakbij de sampler, maar de overeenkomstige waarden verder verwijderd van de centrale as worden hoger. Het effect van de interface is dus sterk afhankelijk van de meetpositie. Zelfs een kleine verschuiving van de actuele positie van de sampler leidt tot een aanzienlijke verandering in de resultaten. De berekeningsresultaten werden vergeleken met meetgegevens uit de literatuur en er werd een redelijke overeenstemming bereikt. De resultaten geven een beter inzicht in de onderliggende fysica verantwoordelijk voor het effect van de sampler.

In **Hoofdstuk 5** worden de effecten van typische plasmacondities op de plasmakarakteristieken van het ICP in contact met een MS interface bestudeerd. Hiertoe werden verschillende stromingssnelheden van het injectorgas en het hulpgas aangelegd, in een brede range. Ook werd het effect van de vermogenstoevoer in detail bestudeerd.

Er lijkt een optimum te bestaan voor de stromingssnelheid van het injectorgas voor elke opstelling, die garandeert dat er een centraal kanaal in de toorts gevormd wordt met een geschikte lengte. Bovendien tonen de resultaten van ons model dat het voor elk specifiek geval mogelijk is om te controleren of ofwel enkel het injectorgas door de sampleropening kan passeren, of dat het injectorgas vergezeld wordt van het hulpgas. Afhankelijk van de groote van de ionenwolk van het monster zal de ene of andere voorwaarde de voorkeur genieten. We hebben ook gevonden dat, afhankelijk van de geometrie, de variatie van de uitgaande gasstromingssnelheid veel kleiner is dan de variatie van de stromingssnelheid van het injectorgas, en dit veroorzaakt een lichtjes hogere druk in de toorts. Het algemene effect van een hoger vermogen is een toename in de plasmatemperatuur, wat resulteert in een hogere ionizatie in de zone binnen de spoel. Het negatieve effect is echter dat het koele centrale kanaal, dat belangrijk is om het monster naar de sampler te vervoeren, korter wordt. Met een geschikt vermogen kan de efficiëntie van het systeem geoptimaliseerd worden. Het vermogen bepaalt immers de gasstromingsprofielen, en zo kan ook op die manier gecontroleerd worden welke flow (d.w.z. enkel van het injectorgas of ook van het hulpgas) door de sampleropening geraakt. De berekeningsresultaten werden vergeleken met experimentele gegevens uit de literatuur, en er werd een goede kwalitatieve overeenstemming bereikt.

Vervolgens worden in **Hoofdstuk 6** de effecten van de diameter van de sampleropening (tussen 1 en 2 mm) en van de afstand van de sampler tot de spoel (tussen 7 en 17 mm) bestudeerd. Een grotere diameter van de sampleropening geeft een hogere plasmatemperatuur in het centrum, op de plaats van de sampler, alsook een meer efficiënte doorstroming van het gas doorheen de sampler, doordat de interactie tussen het plasmagas en de sampler vermindert. De flow snelheid ter hoogte van de sampler is echter onafhankelijk van de diameter van de sampleropening. Door aanpassen van de diameter van de sampleropening kunnen we bepalen of enkel het injectorgas of ook het hulpgas doorheen de sampler geraakt. Tenslotte vonden we dat de plasmatemperatuur ter hoogte van de sampler lichtjes daalt bij toenemende afstand tussen sampler en spoel, wat gevolgen kan hebben voor de ionenvorming en het transport doorheen de sampler. De berekende resultaten zijn opnieuw in redelijke overeenstemming met meetgegevens uit de literatuur.

Tenslotte wordt in **Hoofdstuk 7** het voorkomen van recirculatie in de stromingsprofielen van het hulpgas en het injectorgas bestudeerd. De effecten van de werkparameters, zoals aangelegd vermogen en gasstromingssnelheden, alsook van de geometrie, nl. diameter van de sampleropening en van de injector inlaat, worden bestudeerd. Onze berekeningen voorspellen dat bij hoger aangelegd vermogen het hulpgas en injectorgas in de toorts meer in de voorwaartste richting bewegen naar de sampler toe, wat ook gevalideerd is voor de stroming van het hulpgas, door experimenten uitgevoerd door Günther en medewerkers aan ETH-Zürich. Bovendien kan een stijging van de verschillende gasstromingssnelheden ook het voorkomen van recirculatie verminderen. Dit is vooral zo voor de stromingssnelheid van het injectorgas, die een meer uitgesproken effect heeft op het verminderen van de terugwaartse beweging van de stromingsprofielen dan de stromingssnelheden van het hulpgas en het koelgas. Bovendien leidt een grotere sampleropening (bv. 2 mm in plaats van 1 mm) tot een vermindering van de terugwaartse gasstroming van de stromingsprofielen van het hulpgas. Tenslotte veroorzaakt een centrale gasinlaat van 2 mm diameter meer recirculatie in de stroming van het injectorgas dan een centrale inlaat met diameter van 1.5 mm, wat opnieuw vermeden kan worden door aanpassen van de werkparameters.

We kunnen besluiten dat de studies uitgevoerd tijdens dit doctoraatswerk bijdragen tot een beter begrip van de fundamentele mechanismen van het ICP, en we hopen dat dit de analytische capaciteiten van ICP-MS zal verbeteren. In de toekomst plannen we om de invoer van deeltjes/druppeltjes van het te analyseren materiaal in de ICP toorts in rekening te brengen, zoals kort beschreven staat in **Hoofdstuk 8**. Het model gepresenteerd in dit doctoraatswerk vormt het ideale startpunt voor zulk een verdere modelontwikkeling.

List of Publications

[1] M. Aghaei, S. Mehrabian, and S. H. Tavassoli, Simulation of nanosecond pulsed laser ablation of copper samples: A focus on laser induced plasma radiation, Journal of Applied Physics 104 (2008) 053303-9.

[2] S. Mehrabian, M. Aghaei, S. H. Tavassoli, Effect of background gas pressure and laser pulse intensity on laser induced plasma radiation of copper samples, Physics Of Plasmas 17 (2010) 043301-9.

[3] A. Bogaerts, M. Aghaei, D. Autrique, et.al Computer Simulations of Laser Ablation, Plume Expansion and Plasma Formation, Advanced materials research, Trans Tech Publications 227 (2011) 1-10.

[4] M. Aghaei, H. Lindner, A. Bogaerts, Effect of a mass spectrometer interface on inductively coupled plasma characteristics: a computational study, Journal of Analytical Atomic Spectrometry 27 (2012) 604-610.

[5] M. Aghaei, H. Lindner, A. Bogaerts, Optimization of operating parameters for inductively coupled plasma mass spectrometry: A computational study, Spectrochimica Acta Part B: Atomic Spectroscopy 76 (2012) 56-64.

[6] M. Aghaei, H. Lindner, A. Bogaerts, Effect of sampling cone position and diameter on the gas flow dynamics in an ICP, Journal of Analytical Atomic Spectrometry 28 (2013) 1485-1492.

[7] M. Aghaei, L. Flamigni, H. Lindner, D. Gunther, A. Bogaerts, Occurrence of gas flow rotational motion inside the ICP torch: a computational and experimental study, Journal of Analytical Atomic Spectrometry 29 (2014) 249-261 (Selected as inner front-**Cover picture**).

[8] O. Borovinskaya, M. Aghaei, L. Flamigni, B. Hattendorf, M. Tanner, A. Bogaerts, D. Günther, Diffusion- and velocity-driven spatial separation of analytes from single droplets entering an ICP off-axis, Journal of Analytical Atomic Spectrometry 29, 262-271 (2014) (Selected as **Cover picture**).

Note: The first two papers were obtained, while I was performing my M.Sc. research at Laser and Plasma Research Institute, Shahid Beheshti University, in Tehran, Iran, i.e., before my PhD work at the University of Antwerp started.

List of invited talks and other conference contributions

[1] Invited talk: M. Aghaei, H. Lindner, A. Bogaerts, “Inductively coupled plasma connected to a mass spectrometer: optimization through computations”, Symposium of the Atomic Spectroscopy working group of the section Analytical Chemistry, Dutch Royal Society of Chemistry, May 2013, Deventer, The Netherlands.

[2] Invited talk: M. Aghaei, A. Bogaerts, “Gas flow dynamics in ICPMS: Description, explanation and optimization”, SCIX (presented by the Federation of Analytical Chemistry and Spectroscopy Societies FACSS), September-October 2013, Milwaukee, WI, USA.

[3] Joint invited talk: A. Bogaerts, M. Aghaei, “Understanding the Underlying Mechanisms of ICP-OES and ICP-MS”, A web seminar hosted by “SPECTROSCOPY: solution for material analysis”, January 2014 (485 people worldwide were registered for this web seminar)

[4] Oral presentation: M. Aghaei, H. Lindner, A. Bogaerts, “Modeling of nanoparticles synthesis in laser ablation plasmas by focusing on ionization effect”, Second international conference on Laser and Plasma Application in Material Science (LAPAMS), November 2010, Algiers, Algeria.

[5] Oral presentation: M. Aghaei, H. Lindner, A. Bogaerts, “Computational optimization of operating parameters of ICPMS”, SCIX (presented by the Federation of Analytical Chemistry and Spectroscopy Societies FACSS), October 2012, Kansas city, Missouri, USA.

[6] Oral presentation: M. Aghaei, H. Lindner, A. Bogaerts, “Optimization of geometrical and operating parameters of an inductively coupled plasma mass spectrometer”, European Winter Plasma Conference on Plasma Spectrochemistry, February 2013, Kraków, Poland.

[7] Oral presentation: M. Aghaei, A. Bogaerts, “Introduction of sample particles through an ICP torch: A computational study”, Winter Conference on Plasma Spectrochemistry (WCPS), January 2014, Amelia Island, Florida, USA.

[8] Poster presentation: M. Aghaei, A. Bogaerts, “Formation of Nanoparticles in Laser Ablation Plasmas”, International school on laser-surface interactions for new materials production: tailoring materials and properties, July 2010, Venice, Italy.

[9] Poster presentation: M. Aghaei, H. Lindner, A. Bogaerts, “Numerical study of an ICP in the presence of MS sampling interface”, Winter Conference on Plasma Spectrochemistry (WCPS), January 2012,Tucson, Arizona, USA.

Bibliography

[1] H. Conrads, M. Schmidt, Plasma generation and plasma sources, Plasma Sources Sci. Technol. 9 (2000) 441-454.

[2] N.S.J. Braithwaite, Introduction to gas discharges, Plasma Sources Sci. Technol. 9 (2000) 517-527.

[3] C. Tendero, C. Tixier, P. Tristant, J. Desmaison, P. Leprince, Atmospheric pressure plasmas: A review, Spectrochimica Acta Part B 61 (2006) 2-30.

[4] M. Boulos, 1991 Thermal Plasma Processing. IEEE Transactions on Plasma Science, 196 (1991), 1078-1089.

[5] M. Moisan, M. D. Calzada, A. Gamero, A. Sola, Experimental investigation and characterization of the departure from local thermodynamic equilibrium along a surface-wave-sustained discharge at atmospheric pressure, J. Appl. Phys. 80 (1996) 46-55.

[6] M. I. Boulos, P. Fauchais, E. Pfender, Thermal plasmas: Fundamental and applications. Vol. I, Plenum Press, New York, 1994.

[7] H. R. Griem, Validity of local thermal equilibrium in plasma spectroscopy, Phys. Rev. 131 (1963) 1170-1176.

[8] R. H. Huddlestone, S. L. Leonard, Plasma Diagnostic Techniques, Academic Press, New York, 1965.

[9] H. R. Griem, Plasma Spectroscopy, McGraw-Hill, New York, 1964.

[10] W. Lochte-Holtgreven, Plasma Diagnostics, North-Holland, Amsterdam, 1968.

[11] M. Mitchner, C.H. Kruger Jr., Partially Ionized Gases, Wiley, New York, 1973.

[12] J. Hopwood, Review of inductively coupled plasmas for plasma processing, Plasma Sources Sci. Technol. 1 (1992) 109-116.

[13] B. Chapman, Glow Discharge Processes, Wiley, New York, 1980.

[14] A. Bogaerts, E. Neyts , R. Gijbels , J. Van Der Mullen, Gas discharge plasmas and their applications, Spectrochimica Acta Part B 57 (2002) 609-658

[15] M. A. Lieberman, A.J. Lichtenberg, Principles of Plasma Discharges and Materials Processing, Wiley, New York, 1994.

[16] J. Jonkers, Excitation and transport in small scale plasmas, Ph. D. Thesis, Eindhoven University of Technology, 1998.

[17] G. G. Lister, Electrodeless gas discharges for lighting, in: H. Schluter, A. Shivarova (Eds.), Advanced echnologies based on wave and beam generated plasmas, NATO Science Series, Kluwer, Dordrecht, (1999), 65-96.

[18] M. Shinomiya, K. Kobayashi, M. Higashikawa, S. Ukegawa, J. Matsuura, K. Tanigawa, Development of the electrodeless fluorescent lamp, J. Illum. Eng. Soc. 20 (1991)44-49.

[19] J. Bethenod, Electromagnetic Apparatus, US Patent #2,030,957, 1936.

[20] J. W. Waggoner, M. Belkin, K.L. Sutton, J.A. Caruso, H.B. Fannin, Novel low power / reduced pressure inductively coupled plasma ionization source for mass spectrometric detection of organotin species, J. Anal. At. Spectrom. 13 (1998) 879-883.

[21] A. Montaser, Inductively coupled plasma mass spectrometry, Wiley, New York, 1998.
[22] X. Hou and B. T. Jones, Inductively coupled plasma/optical emission spectrometry, in Encyclopedia of Analytical chemistry, R.A. Meyers (Ed.), John Wiley & Sons Ltd, Chichester, 2000.
[23] W. J. M. Boumans and F. J. De Boer, Studies of flame and plasma torch emission for simultaneous multi-element analysis I, Preliminary investigations, Spectrochim. Acta. Part B 27 (1972) 391-414.
[24] V. Colombo, E. Ghedini, G. Masini, D. Russo, F. Andreola, L. Barbieri, D. Belviso, I. Lancellotti, P. Pozzi, rf thermal plasma treatment of waste glass and its reutilization in composite materials , HighTemp. Mat. Proc. 10 (2006) 207-218.
[25] V. Colombo, E. Ghedini, and P. Sanibondi, A three-dimensional investigation of the effects of excitation frequency and sheath gas mixing in n an atmospheric-pressure inductively coupled plasma system, J. Phys. D, Appl. Phys. 43 (2010) 105202-105-215.
[26] B. M. Goortani, P. Proulx, S. Xue, and N. Y. Mendoza-Gonzales, Controlling nanostructure in thermal plasma processing: Moving from highly aggregated porous structure to spherical silica nanoparticles, Powder Technol. 175 (2007) 22-32.
[27] G. Cocito, L. Cognolato, V. Colombo, G. Dellapiana, and C. Panciatichi, Modeling, project and numerical simulation of an inductively coupled plasma torch for the deposition of SiO2, presented at the 48th Annual Gaseous Electronic Conference, Berkeley, CA, Oct. 1995.
[28] G. Cocito, L. Cognolato, V. Colombo, C. Panciatichi, and A. Zazo, AES temperature diagnostics in an inductively coupled plasma torch for the deposition of high purity fused silica for optical waveguides, presented at the 49th Annual Gaseous Electronic Conference, Argonne, IL, Oct. 1996.
[29] Technical note, ICP-MS A Primer, Agilent Technologies, Inc. www.agilent.com/chem/icpms (2005).
[30] Technical note, The 30-minute guide to ICP-MS, PerkinElmer, Inc www.perkinelmer.com.
[31] A. Montaser, Inductively coupled plasma mass spectrometry, Wiley, New York, 1992.
[32] W.R. Lane, Shatter of drops in stream of air, Ind. Eng. Chem. 43 (1951) 1312-1317.
[33] W. R. Marshal, Jr., Atomization and spray drying, Chem. Eng. Prog. Monogr. Ser. 2 (1954) 1-122.
[34] S. Greenfield and P.B. Smith, The determination of trace metals in microliter samples by plasma torch excitation, Anal. Chim. Acta 59 (1972) 341-348.
[35] A. Aziz, J. A. C. Broekaert, and F. Leis, Analysis of Micro-Amounts of biological samples by evaporation in a graphite furnace and ICP AES, Spectrochim. Acta Part B 37 (1982) 369-379.
[36] H. Matusiewicz, Thermal vaporization for ICPOES, J. Anal. At. Spectrom. 1 (1986) 171-184.
[37] E. D. Salin and G. Horlick, Direct sample insertion device for the ICP emission spectrometry, Anal. Chem. 51(1979) 2248-2286.

[38] J. Ruzicka, Flow injection analysis, Wiley-Interscience. New York, 1988.

[39] R. E. Majors, H.G. Barth, and C. H. Lochmuller, Column liquid chromatography, Anal. Chem. 56 (1984) 300-349.

[40] P. B. Farnsworth and G. M. Hieftje, Sample introduction into the ICP by a radiofrequency arc, Anal. Chem. 55 (1983) 1414-1417.

[41] A. Aziz, J. A. C. Broekaert, K. Laqua and F. Leis, A study of direct analysis of solid samples using spark ablation combined with excitation in an ICP. Spectrochim. Acta Part B 39 (1983) 1091-1103.

[42] A. Lemarchand, G. Labarraque, P. Massin and J. A. C. Broekaert, Analysis of ferrous alloys by spark ablation coupled to ICPAES, J. Anal. At. Spectrom. 2 (1987) 481-484.

[43] B. Hattendorf, D. Günther, Characteristics and capabilities of an ICP-MS with a dynamic reaction cell for dry aerosols and laser ablation, J. Anal. At. Spectrom. 15 (2000) 1125-1131.

[44] D. Günther, I. Horn, B. Hattendorf, Recent trends and developments in LA-ICP-MS
Fresenius J. Anal. Chem. 368 (2000) 4-14.

[45] D. Günther, J. M. Mermet, Laser ablation for inductively coupled plasma-mass spectrometry in Discrete sample introduction techniques for ICP-MS, Wilson&Wilson's, Comprehensive Analytical Chemistry, Ed. D. Barcelo, Elsevier, 2000.

[46] D. Bleiner, and D. Günther, Theoretical description and experimental observation of aerosol transport processes in laser ablation inductively coupled plasma mass spectrometry, J. Anal. At. Spectrom. 16 (2001) 449-456.

[47] D. Günther, Laser ablation-inductively coupled plasma mass spectrometry trends, Journal of Analytical and Bioanalytical Chemistry 372 (2002) 31-32.

[48] D. Günther, B. Hattendorf, Sample introduction in ICP-MS: Laser ablation in: The encyclopedia of mass spectrometry, Vol. 5, Elemental and Isotope Ratio Mass Spectrometry, D. Beauchemin, D. E. Matthews, (Eds.) Elsevier, Oxford, 2010.

[49] J. J. Gonzalez, D. Oropeza, X. Mao, and R. E. Russo, Assessment of the precision and accuracy of thorium (232 Th) and uranium (238 U) measured by quadrupole based-inductively coupled plasma-mass spectrometry: Comparison of liquid nebulization, nanosecond and femtosecond laser ablation, J. Anal. At. Spectrom. 23 (2008) 229-234.

[50] B. Matthieu, Y. Y. Boueri, X. Mao, S. S. Mao, X. Mao, and R. E. Russo, Correlation between early-stage expansion and spectral emission of nanosecond laser-induced plasma from organic material, SPIE 7005 (2008) 1-8.

[51] J. J. Gonzalez, A. J. Fernandez, D. Oropeza, X. Mao, and R. E. Russo, Femtosecond laser ablation: experimental study of the repetition rate influence on qualitative and quantitative ICP-MS performance, Spectrochim. Acta Part B 63 (2008) 277-286.

[52] R. E. Russo, X. Mao, J. H. Yoo, J. J. Gonzalez, S. P. Jagdish, and T. S. Narayan, Laser ablation, in Laser induced breakdown spectroscopy, Elsevier Science, 2008.

[53] B. E. Naes, S. Umpierrez, S. Ryland, C. Barnett, J. R. Almirall, A comparison of laser ablation inductively coupled plasma mass spectrometry, micro X-ray fluorescence

spectroscopy, and laser induced breakdown spectroscopy for the discrimination of automotive glass, Spectrochim. Acta Part B 63 (2008) 1145-1150.
[54] S. Gschwind, L. Flamigni, J. Koch, O. Borovinskaya, S. Groh, K. Niemax, D. Günther, Capabilities of inductively coupled plasma mass spectrometry for the detection of nanoparticles carried by monodisperse micro-droplets, J. Anal. At. Spectrom. 26 (2011) 1166 - 1174.
[55] S. Gschwind, H. Hagendorfer, D. A Frick, D. Günther, Mass Quantification of nanoparticles by single droplet calibration using inductively coupled plasma mass spectrometry, Anal. Chem. 85 (2013) 5875-5883.
[56] J. A. C. Broekaert, Analytical Atomic Spectrometry with Flames and Plasmas, Wiley, Weinheim, 2005.
[57] B. Gercken and R. M. Barnes, Determination of lead and other trace elements species in blood by size exclusion chromatography and ICPMS, Anal. Chem. 63 (1991) 283-287.
[58] C. M. Schumacher, I. K. Herrmann, S. B. Bubenhofer, S. Gschwind, A. M. Hirt, B. Beck-Schimmer, D. Günther, W. J. Stark, Quantitative recovery of magnetic nanoparticles from flowing blood: Trace analysis and the role of magnetization Advanced Functional Materials 23 (2013) 4888-4896
[59] Ch. Latkoczy, W.P. Strasse, S. Thorrold, P. K. Swart, D. Günther, Fish ear bones hold clues to migration - Implications for fisheries models and design of marine protected areas, Forensic Science International 136 (2003) 384-3851.
[60] RP. Vasconcelos, P. Reis-Santos, S. Tanner, V. Fonseca, C. Latkoczy, D. Günther, MJ. Costa, H. Cabral, Discriminating estuarine nurseries for five fish species through otolith elemental fingerprints, Marine Ecology Progress Series 350 (2007) 117-126.
[61] A. W. Boorn, J. E. Fulford, and W. Wegscheider, Determination of trace elements in organic material by inductively coupled plasma mass spectrometry, Microchim. Acta. 2 (1985) 171-178.
[62] E. M. Thurman and R. L. Malcolm, Preparative isolation of aquatic humic substances, Environ. Sci. Technol. 15 (1981) 463-466.
[63] S. Munro, L. Ebdon, and D. J. Mc Weeny, Application of ICPMS for trace metal determination in foods, J. Anal. At. Spectrom. 1 (1986) 211-219.
[64] J. R. Dean, L. Ebdon, and R. C. Massey, Isotope ratio and isotope dilution analysis of lead in wine by inductively coupled plasma mass spectrometry, Doof Addit. Contam. 7 (1990) 109-116.
[65] A. R Date and K. E. Javris, Application of ICP-MS in the earth sciences, in Application of inductively coupled plasma mass spectrometry, A.R. Date and A. L. Gray, Eds., Blackie, London, 1989.
[66] W. Doherty and A. Van Der Voet, The application of inductively coupled plasma mass spectrometry to the determination of rare earth elements in geological materials, Can. J. Spectrosc. 30 (1985) 135-141.
[67] A. Audétat, D. Günther, C. A. Heinrich, Causes for large scale metal zonation around mineralized plutons: fluid inclusion LA-ICP-MS evidence from the mole granite, Australia, Economic Geology 95 (2000) 1563-1581.

[68] C. Prince, J. Kosler, D. Vance, D. Günther, Comparison of LA-ICP-MS and isotope dilution REE-analysis - implications for Sm-Nd garnet, Chemical Geology 168 (2000) 255-274.
[69] A. Audétat, D. Günther, C. A. Heinrich, Magmatic-hydrothermal evolution in a fractionating granite: A microchemical study of the Sn-W-F mineralized mole granite, Geochimica & Cosmochimica Acta. 64 (2000) 3373-3393.
[70] P. Garofalo, A. Audétat, D. Günther, C. A. Heinrich, J. Ridley, Estimation and testing of standard molar thermodynamic properties of tourmaline end-members using data of natural samples American Mineralogist 85 (2000) 78-88.
[71] A. M. Piotrowski, D. C. Lee, J. N. Christensen, K. W. Burton, A. N. Halliday, J. R. Hein, D. Günther, Changes in erosion and ocean circulation recorded in the Hf isotopic compositions of North Atlantic and Indian Ocean ferromanganese crusts, Earth and Plenatary Science 181 (2000) 315-325.
[72] M. Frank, T. van de Flierdt, A. N. Halliday, P. W. Kubik, B. Hattendorf, D. Günther, The Evolution of deep water mixing and weathering inputs in the central Atlantic Ocean over the Past 33 Myr, Paleoceanography 18 (2003) 1091.
[73] R.V.D. Roberts, E. Van Wyk, and R. Palmer, Concentration of noble metals by a fire assay technique using nickel sulfide as a collector, National institute of Metallurgy, South Africa Report 1705 (1971).
[74] N. I. Ward, Environmental analysis using ICPMS in Application of inductively coupled plasma mass spectrometry. A.R. Date and A. L. Gray, Eds., Blackie, London, 1989.
[75] H. E. Taylor, Water resources, in Application of inductively coupled plasma mass spectrometry. A.R. Date and A. L. Gray, Eds., Blackie, London, 1989.
[76] J. Toole, K. McKay, and M. Baxter, Determination of uranium in marine sediment pore waters by isotope dilution inductively coupled plasma mass spectrometry, Anal. Chim. Acta. 245 (1991) 83-88.
[77] K. Takeda, T. Yamaguchi, H. Akiyama, and, T. Masuda, Determination of ultra-amount of uranium and thorium on high-purity aluminum by inductively coupled plasma mass spectrometry, Analyst 116 (1991) 501-504
[78] J. Marshall, J. Franks, I. abell, and C. Tye, Determination of trace elements in solid plastic materials by laser ablation inductively coupled plasma mass spectrometry, J. Anal. At. Spectrom. 6 (1991) 145-150.
[79] H. P. Longerich, B. J. Fryer, and D. F. Strong, Trace analysis of natural alloys by inductively coupled plasma mass spectrometry: Application to archeological native silver artifacts, Spectchim. Acta Part B 42 (1987) 101-109.
[80] http://www.speciation.net/Database/Instruments/PerkinElmer-SCIEX/ELAN-250-;i2673
[81] R. S. Houk, V. A. Fassel, G. D. Flesch, H. J. Svec, A. L. Gray and C. E. Taylor, Inductively coupled argon plasma as an ion source for mass spectrometric determination of trace elements, Anal. Chem. 52 (1980) 2283-2289.
[82] R. S. Houk, V. A. Fassel and H. J. Svec, Inductively coupled plasma - mass spectrometry: Sample introduction, ionization, ion extraction, and analytical results in

dynamic mass spectrometry, D. Price and J. F. J. Todd, Eds., Heyden, London, Vol.6, 1981.

[83] B.S. Duersch, P.B. Farnsworth, Characterization of the ion beam inside the skimmer cone of an inductively coupled plasma mass spectrometer by laser excited atomic and ionic fluorescence, Spectrochim. Acta Part B 54 (1999) 545-555.

[84] D.M. Chambers, G.M. Hieftje, Fundamental studies of the sampling process in an inductively coupled plasma mass spectrometer. II. Ion kinetic energy measurements, Spectrochim. Acta Part B 46 (1991) 761-784.

[85] A.L. Gray, R.S. Houk, J.G. Williams, Langmuir probe potential measurements in the plasma and their correlation with mass spectral characteristics in inductively coupled plasma mass spectrometry, J. Anal. At. Spectrom. 2 (1987) 13-20.

[86] R.S. Houk, J.K. Schoer, J.S. Crain, Plasma potential measurements for inductively coupled plasma mass spectrometry with a center-tapped load coil, J. Anal. At. Spectrom. 2 (1987) 283-286.

[87] I.I. Stewart, C.E. Hensman, J.W. Olesik, Influence of gas sampling on analyte transport within the ICP and ion sampling for ICP-MS studied using individual, isolated sample droplets, Appl. Spectrosc. 54 (2000) 164-174.

[88] G. Meyer, R. Foster, A. Van der Hoeff, T. Albert, S. Luan, K. Hu, S. Karpova-Nadel, J. Schmeizel, Increasing laboratory productivity by combining ICP optical emission with ICP mass spectrometry, Am. Lab. 28 (1996) 21-24.

[89] H.P. Longerich, Mass spectrometric determination of the temperature of an argon inductively coupled plasma from the formation of the singly charged monoxide rare earths and their known dissociation energies, J. Anal. At. Spectrom. 4 (1989) 491-497.

[90] K. Lepla, M.A. Vaughan, G. Horlick, Simultaneous atomic emission and mass spectrometric measurements on an inductively coupled plasma, Spectrochim. Acta Part B 46 (1991) 967-973.

[91] R.S. Houk, Y. Zhai, Comparison of mass spectrometric and optical measurements of temperature and electron density in the inductively coupled plasma during mass spectrometric sampling, Spectrochim. Acta Part B 56 (2001) 1055-1067.

[92] R.S. Houk, J.K. Schoer, J.S. Crain, Deduction of excitation temperatures for various analyte species in inductively coupled plasmas from vertically-resolved emission profiles, Spectrochim. Acta Part B 42 (1987) 841-852.

[93] L. Pei-Qi, G. Pei-Zhing, L. Tei-Zheng, R.S. Houk, Langmuir probe measurements of electron temperature in an ICP, Spectrochim. Acta Part B 43 (1988) 273-285.

[94] H. Niu, R.S. Houk, Fundamental aspects of ion extraction in inductively coupled plasma mass spectrometry, Spectrochim. Acta Part B 51 (1996) 779-815.

[95] J.S. Crain, F.G. Smith, R.S. Houk, Mass spectrometric measurement of ionization temperature in an inductively coupled plasma, Spectrochim. Acta Part B 45 (1990) 249-259.

[96] R. S. Houk, B. R. LaFreniere, H. B. Lim and V. A. Fassel, Extraction Discharge Source for Enhancing Analyte Line Intensities in Inductively Coupled Plasma Atomic Emission Spectrometry, Appl. Spectrosc. 41 (1987) 391-395.

[97] R. K. Winge, J. S. Crain, and R. S. Houk, A High Speed Photographic Study of Plasma Fluctuations and Undissociated Particles in ICP-MS, J. Anal. Atomic Spectrom. 6 (1991) 601-604.
[98] H. Ma, N. Taylor, P.B. Farnsworth, The effect of the sampling interface on spatial distributions of barium ions and atoms in an inductively coupled plasma ion source, Spectrochimica Acta Part B 64 (2009) 384-391.
[99] S.A. Lehn, K.A.Warner, M. Huang, G.M. Hieftje, Effect of an inductively coupled plasma mass spectrometry sampler interface on electron temperature, electron number density, gas-kinetic temperature and analyte emission intensity upstream in the plasma, Spectrochim. Acta Part B 57 (2002) 1739-1751.
[100] J.H. Macedone, D.J. Gammon, P.B. Farnsworth, Factors affecting analyte transport through the sampling orifice of an inductively coupled plasma mass spectrometer, Spectrochim. Acta Part B 56 (2001) 1687-1695.
[101] B.S. Duersch, Y. Chen, A. Ciocan, P.B. Farnsworth, Optical measurements of ion density in the second vacuum stage of an inductively coupled plasma mass spectrometer, Spectrochim. Acta Part B 53 (1998) 569-579.
[102] S. Kaneco, T. Nomizo, T. Tanaka, N. Mizutani, H. Kawaguchi, Optimization of operating conditions in individual airborne particle analysis by inductively coupled plasma mass spectrometry, Anal. Sci. 11 (1995) 835-840.
[103] W.G. Diegor, H.P. Longerich, Parameter interaction in signal optimization of an ICP mass spectrometer, At. Spectr. 21 (2000) 111-117.
[104] H.P. Longerich, B.J. Fryer, D.F. Strong, C.J. Kantipuly, Effects of operating conditions on the determination of the rare earth elements by inductively coupled plasma-mass spectrometry (ICP-MS), Spectrochim. Acta Part B 42 (1987) 75-92.
[105] S.E. Long, R.M. Brown, Optimization in inductively coupled plasma mass spectrometry, Analyst (Cambridge, United Kingdom) 111 (1986) 901-906.
[106] Q. Xie, R. Kerrich, Optimization of operating conditions for improved precision of zirconium and hafnium isotope ratio measurement by inductively coupled plasma mass spectrometry (ICP-MS), J. Anal. At. Spectrom. 10 (1995) 99-103.
[107] B.T.G. Ting, M. Janghorbani, Optimization of instrumental parameters for the precise measurement of isotope ratios with inductively coupled plasma mass spectrometry, J. Anal. At. Spectrom. 3 (1988) 325-336.
[108] G. Gamez, S.A. Lehn, M. Huang, G.M. Hieftje, Effect of Mass Spectrometric sampling interface on the fundamental parameters of an inductively coupled plasma as a function of its operating conditions. Part I. Applied RF power and vacuum, Spectrochim. Acta Part B 62 (2007) 357-369.
[109] G. Gamez, S.A. Lehn, M. Huang, G.M. Hieftje, Effect of Mass Spectrometric sampling interface on the fundamental parameters of an inductively coupled plasma as a function of its operating conditions. Part II. Central-gas flow rate and sampling depth, Spectrochim. Acta Part B 62 (2007) 370-377
[110] J.H. Macedone, A.A. Mills, P.B. Farnsworth, Optical measurements of ion trajectories through the vacuum interface of an inductively coupled plasma mass spectrometer, Appl. Spectrosc. 58 (2004) 463-467.

[111]A. L. Gray and A. R. Date, Inductively coupled plasma source mass spectrometry using continuum flow ion extraction, Analyst 108 (1983) 1033-1050.

[112] G. M. Hieftje and G. H. Vickers, Developments in plasma source/mass spectrometry, Anal. Chim. Acta. 216 (1989) 1-24.

[113] F. E. Lichte, A. L. Meier and J. G. Crock, Determination of the rare-earth elements in geological materials by inductively coupled plasma mass spectrometry, Anal. Chem. 59 (1987) 1150-1157.

[114] J. S. Crain, R. S. Houk and F. G. Smith, Matrix interferences in inductively coupled plasma-mass spectrometry: some effects of skimmer orifice diameter and ion lens voltages, Spectrochim. Acta, Part B 43 (1988) 1355-1364.

[115] M. A. Vaughan and G. Horlick, Effect of sampler and skimmer orifice size on analyte and analyte oxide signals in inductively coupled plasma mass spectrometry, Spectrochim. Acta, Part B 45 (1990) 1289-1299.

[116] H. P. Longerich, B. J. Fryer, D. F. Strong and C. J. Kanttpuly, Effects of operating conditions on the determination of the rare earth elements by inductively coupled plasma-mass spectrometry (ICP-MS),Spectrochim. Acta, Part B 42 (1987) 75-92.

[117] D. Günther, H. P. Longerich, S. E. Jackson and L. Forsythe, Effect of sampler orifice diameter on dry plasma inductively coupled plasma mass spectrometry (ICP-MS) backgrounds, sensitivities, and limits of detection using laser ablation sample introduction, Fresenius' J. Anal. Chem. 355 (1996) 771-773.

[118] N. Taylor and P. B. Farnsworth, Experimental characterization of the effect of skimmer cone design on shock formation and ion transmission efficiency in the vacuum interface of an inductively coupled plasma mass spectrometer,Spectrochim. Acta, Part B 69 (2012) 2-8.

[119] R. K. Winge, J. S. Crain, and R. S. Houk, A high speed photographic study of plasma fluctuations and un-dissociated particles in ICP-MS, J. Anal. Atomic Spectrom. 6 (1991) 601-604.

[120] C. T. Crowe, M.P. Sharma, and D.E. Stock, The Particle-Source-In-Cell (PSI-Cell) model for gas-droplet flows, J. Fluids Engng. 99 (1977) 325-332.

[121] M.I. Boulos, Heating of powders in the fire ball of an induction plasma, IEEE Trans. Plasma Sci. 6 (1978) 91-106.

[122] J. Mostaghimi, E. Pfender, Effects of metallic vapor on the properties of an argon arc plasma, Plasma Chem.Plasma Process. 4 (1984) 199-217.

[123] P. Proulx, J. Mostaghimi, and M. I. Boulos, Plasma-particle interaction effects in induction plasma modeling under dense loading conditions, Int. J. Heat Mass Transfer. 28 (1985)1327-1336.

[124] P. Proulx, J. Mostaghimi, and, M. I. Boulos, Heating of powders in an r.f. inductively coupled plasma under dense loading conditions, Plasma Chemistry and Plasma Processing 7 (1987) 29-52.

[125] J. Mostaghimi, P. Proulx and, M. I. Boulos, An analysis of the computer modeling of the flow and temperature fields in an inductively coupled plasma, Numerical Heat Transfer 8 (1985) 187-201.

[126] J. Mostaghimi, P. Proulx, M. I. Boulos and R. M. Barnes, Computer modeling of the emission patterns for a spectrochemical ICP, Spectrochemica Acta part B 40 (1985) 153-166.

[127] J. Mostaghimi, P.Proulx, and M. Boulos, A two temperature model of the inductively coupled rf plasma, Journal of Applied Physics 61 (1987) 1753-1760.

[128] J. Mostaghimi and M. l. Boulos, Effect of frequency on local thermodynamic equilibrium conditions in an inductively coupled argon plasma at atmospheric pressure, J. AppL Phys. 68 (1990) 2643-2648.

[129] M. EI-Hage, J. Mostaghimi, and M. I. Boulos, A turbulent flow model for the rf inductively coupled plasma, Journal of Applied Physics 65 (1989) 4178.

[130] J. Mostaghimi, M. I. Boulos, Two-dimensional electromagnetic field effects in induction plasma modelling, Plasma Chemistry and Plasma Processing 9 (1989) 25-44.

[131] P. Yang and R. M. Barnes, J. Mostaghimi and M. I. Boulos, Application of a two-dimensional model in the simulation of an analytical inductively coupled plasma discharge, Spectrochimica Acta B 44 (1989) 657-666.

[132] Z. Njah, J. Mostaghimi, and M. Boulos, Mathematical modelling of the 3-d mixing in an induction plasma reactor, lnt. J. Heat Mass Transfer 36 (1993) 3909-3919.

[133] G. Y. Zhao, J. Mostaghimi, and M. I. Boulos, The induction plasma chemical reactor: part I. equilibrium model, Plasma Chemistry and Plasma Processing 10 (1990) 133-150.

[134] G.Y. Zhao, J. Mostaghimi, and M.I. Boulos, The induction plasma chemical reactor: part II. kinetic model, Plasma Chemistry and Plasma Processing 10 (1990) 151-166.

[135] P. Proulx, J. Mostaghimi and M. I. Boulos, radiative energy transfer in induction plasma modelling, Int. J. Heat Mass Transfer. 34 (1991) 2571-2579.

[136] M. Cai, A. Montaser, J. Mostaghimi, Two-temperature model for the simulation of atmospheric-pressure helium ICPs, Applied Spectroscopy 49 (1995) 1390-1402.

[137] M. Cai, A. Montaser, J. Mostaghimi, computer simulation of atmospheric-pressure helium inductively coupled plasma discharges, Spectrochim. Acta Part B 48 (1993) 789-807.

[138] M. Cai, D. A. Haydar, A. Montaser, J. Mostaghimi, Computer simulation of argon-nitrogen and argon-oxygen inductively coupled plasmas, Spectrochim. Acta Part B 52 (1997) 369-386.

[139] S. Xue, P. Proulx, M. I. Boulos, extended-feld electromagnetic model for inductively coupled plasma, J. Phys. D Appl. Phys. 34 (2001) 1897-1906.

[140] P. Yang, J. A. Horner, N. N. Sesi, G. M. Hieftje, Comparison of simulated and experimental fundamental ICP parameters, Spectrochim. Acta Part B 55 (2000) 1833-1845.

[141] C. M. Benson, S. F. Gimelshein, D. A. Levin, A. Montaser, Simulation of droplet heating and desolvation in an inductively coupled plasma- Part I, Spectrochimica Acta Part B 56 (2001) 1097-1112.

[142] C. M. Benson, S. F. Gimelshein, D. A. Levin, and A. Montaser, modeling of droplet evaporation from a nebulizer in an inductively coupled plasma, Rarefied Gas

Dynamics: 22nd International Symposium, American Institute of Physics (2001) 246-253.

[143] C. M. Benson, J. Zhong, S. F. Gimelshein, D. A. Levin, A. Montaser, Simulation of droplet heating and desolvation in inductively coupled plasma-Part II: Coalescence in the Plasma, Spectrochimica Acta Part B 58 (2003) 1453-1471.

[144] V. Colombo, C. Panciatichi, A. Zazo, G. Cocito, and L. Cognolato, Modeling, Project, Numerical Simulation, and AES Temperature Diagnostics of an Inductively Coupled Plasma Torch for the Deposition of High-Purity Fused Silica for Optical Waveguide Production, IEEE Transactions On Plasma Science 25, 1073-1080 (1997).

[145] D. Bernardi, V.Colombo, G. G. M. Coppa, and A. D'Angola, Simulation of the ignition transient in rf inductively coupled plasma torches, Eur. Phys. J. D 14 (2001) 337-348.

[146] D. Bernardi, V. Colombo, G. G. M. Coppa, E. Ghedini, and A. Mentrelli, Investigation on bistability in inductively coupled plasma torches with non-convetional coil, Proceedings of the 7th European conference on thermal plasma processes, Strasburg, France (2002).

[147] D. Bernardi, V. Colomboa, E. Ghedini, and A. Mentrelli, Three-dimensional modeling of inductively coupled plasma torches, Eur. Phys. J. D 22 (2003) 119-125.

[148] D. Bernardi, V. Colombo, E. Ghedini, and A. Mentrelli, Three-dimensional modeling of inductively coupled plasma torches, Pure Appl. Chem. 77 (2005) 359-372.

[149] D. Bernardi, V. Colomboa, E. Ghedini, and A. Mentrelli, Three-dimensional effects in the modeling of ICPTs -Part I: Fluid Dynamics and Electromagnetic, Eur. Phys. J. D 25 (2003) 271-277.

[150] D. Bernardi, V. Colomboa, E. Ghedini, and A. Mentrelli, Three-dimensional effects in the modeling of ICPTs -Part II: Induction Coil and Torch Geometry, Eur. Phys. J. D 25 (2003) 279-285.

[151] V. Colombo, E. Ghedini, and J. Mostaghimi, Three-dimensional modeling of an inductively coupled plasma torch for spectroscopic analysis, IEEE Transactions On Plasma Science 36 (2008) 1040-1041.

[152] D. Bernardi, V. Colombo, E. Ghedini, A. Mentrelli, and T. Trombetti, 3-D numerical simulation of fully-coupled particle heating in ICPTs, Eur. Phys. J. D 28 (2004) 423-433.

[153] D. Bernardi, V. Colombo, E. Ghedini, A. Mentrelli, and T. Trombetti, 3-D numerical analysis of powder injection in inductively coupled plasma torches, IEEE Transactions On Plasma Science 33 (2005) 424-425.

[154] V Colombo, E Ghedini, and P Sanibondi, Three-dimensional investigation of particle treatment in an rf thermal plasma with reaction chamber, Plasma Sources Sci. Technol. 19 (2010) 065024-065036.

[155] D. Bernardi, V. Colombo, E. Ghedini, and A. Mentrelli, 3-D turbulent modeling of an ICPT with detailed gas injection section, IEEE Transactions On Plasma Science 33 (2005) 426-427.

[156] V. Colombo, A. Concetti, E. Ghedini, M. Gherardi, and P. Sanibondi, Three-dimensional time-dependent large eddy simulation of turbulent flows in an inductively

coupled thermal plasma torch with a reaction chamber, IEEE Transactions On Plasma Science 39 (2011) 2894-2895.

[157] V. Colombo, E. Ghedini and P. Sanibondi, Two-temperature thermodynamic and transport properties of argon-hydrogen and nitrogen-hydrogen plasmas, J. Phys. D: Appl. Phys. 42 (2009) 055213-055224.

[158] V. Colombo, E. Ghedini and P. Sanibondi, Two-temperature thermodynamic and transport properties of carbon-oxygen plasmas, Plasma Sources Sci. Technol. 20 (2011) 035003-035010.

[159] V. Colombo, E. Ghedini, M. Gherardi, P. Sanibondi, Modelling for the optimization of the reaction chamber in silicon nanoparticle synthesis by a radio-frequency induction thermal plasma, Plasma Sources Sci. Technol. 21 (2012) 055007-055016.

[160] V. Colombo, E. Ghedini, M. Gherardi , P. Sanibondi, M. Shigeta, A two-dimensional nodal model with turbulent effects for the synthesis of si nano-particles by inductively coupled thermal plasmas, Plasma Sources Sci. Technol. 21 (2012) 025001-025012.

[161] M. Shigeta, T. Sato, H. Nishiyama, Computational simulation of a particle-laden rf inductively coupled plasma with seeded potassium, International Journal of Heat and Mass Transfer, 47 (2004) 707-716.

[162] M. Shigeta, T. Sato, H. Nishiyama, Numerical simulation of a potassium-seeded turbulent rf inductively coupled plasma with particles, Thin Solid Films 435 (2003) 5-12.

[163] H. Nishiyama, and M. Shigeta, Numerical simulation of an rf inductively coupled plasma for functional enhancement by seeding vaporized alkali metal, The European Physical Journal Applied Physics , 18 (2002) 125-133.

[164] M. Shigeta and H. Nishiyama H, Numerical analysis of metallic nanoparticle synthesis using rf inductively coupled plasma flows, Trans. ASME, J. Heat Transfer, 127 (2005) 1222-1230.

[165] M. Shigeta and T. Watanabe, Numerical analysis for co-condensation processes in silicide nanoparticle synthesis using induction thermal plasmas at atmospheric pressure conditions, Journal of Materials Research 20 (2005) 2801-2811

[166] M. Shigeta, Three-dimensional flow dynamics of an argon rf plasma with dc jet assistance: a numerical study, J. Phys. D: Appl. Phys. 46 (2013) 015401-015413.

[167] M. Shigeta, Time-dependent 3D simulation of an argon rf inductively coupled thermal plasma, Plasma Sources Sci. Technol. 21 (2012) 055029-055043.

[168] M. Shigeta, T. Watanabe, H. Nishiyama, Numerical investigation for nano-particle synthesis in an rf inductively coupled plasma, Thin Solid Films 457 (2004) 192-200.

[169] M. Shigeta, and T. Watanabe, Numerical investigation of cooling effect on platinum nanoparticle formation in inductively coupled thermal plasmas, J. Appl. Phys. 103, (2008) 074903-074918.

[170] T. Watanabe, M. Shigeta, N. Atsuchi, Two-temperature chemically-non-equilibrium modeling of argon induction plasmas with diatomic gas, International Journal of Heat and Mass Transfer 49 (2006) 4867-4876.

[171] N. Atsuchi, M. Shigeta, T. Watanabe, Modeling of non-equilibrium argon–oxygen induction plasmas under atmospheric pressure, International Journal of Heat and Mass Transfer 49 (2006) 1073-1082.

[172] D. Benoy, Modeling of thermal argon plasmas, PhD dissertation, Eindhoven University of Technology, 1993.

[173] B. Bottin, D. Vanden Abeele, M. Carbonaro, G. Degrez, and G. S. R Sarma, Thermodynamic and transport properties for inductive plasma modeling, Journal of Thermophysics and Heat Transfer 13 (1999) 343-350.

[174] D. Vanden Abeele, G. Degrez, efficient computational model for inductive plasma flows, AIAA Journal 38 (2000) 234-242.

[175] G. Degrez, D. Vanden Abeele, P. Barbante, B. Bottin, numerical simulation of inductively coupled plasma flows under chemical non-equilibrium, International Journal of Numerical Methods for Heat & Fluid Flow 14 (2004) 538-558.

[176] J. R. Diebel, T. E. Magin, M. Panesi, P. Rini, D. Vanden Abeele, G. Degrez, Simulation of supersonic flows in inductively coupled plasma tunnels, Proceeding of the Third International Conference on Computational Fluid Dynamics, ICCFD3, Toronto (2004) 489-494.

[177] D. J. Douglas, J. B. French, Gas Dynamics of the inductively coupled plasma mass spectrometry interface, J. Anal. At. Spectrom. 3 (1988) 743-747.

[178] R. L. Spencer, J. Krogel, J. Palmer, A. Payne, Modeling the gas flow upstream and in the sampling nozzle of the inductively coupled plasma mass spectrometer via the direct simulation monte carlo algorithm, A. Sampson, W. Somers, C. N. Woods, Spectrochim. Acta Part B 64 (2009) 215-221.

[179] R. L. Spencer, N. Taylor, P. B. Farnsworth, Comparison of calculated and experimental flow velocities from the sampling cone of an inductively coupled plasma mass spectrometer, Spectrochim. Acta Part B 64 (2009) 921-924.

[180] H. Lindner, A. Bogaerts, Multi-element model for the simulation of inductively coupled plasmas: Effects of helium addition to the central gas stream, Spectrochim. Acta Part B 66 (2011) 421-431.

[181] H. Lindner, A. Murtazin. S. Groh, K. Niemax, A. Bogaerts, Simulation and experimental studies on plasma temperature, flow velocity and injector diameter effects for an inductively coupled plasma, Anal. Chem. 83 (2011) 9260-9266.

[182] ANSYS FLUENT 14 Documentation, 2011. ANSYS, Inc. http://www.ansys.com.

[183] A. T. M. Wilbers, J. J. Beulens, D. C. Schram, Radiative energy loss in a two temperature argon plasma, J. Quant. Spectrosc. Radiat. Transfer 46 (1991) 385-392.

[184] G. J. Bastiaans, R. A. Mangold, The calculation of electron density and temperature in Ar spectroscopic plasmas from continuum and line spectra, Spectrochim. Acta Part B 40 (1985) 885-892.

[185] A. W. Irwin, Polynomial partition function approximations of 344 atomic and molecular species, Astrophys. J. Suppl. Series 45 (1981) 621-633.

[186] J. C. Stewart, K. D. Pyatt, Lowering of ionization potentials in plasmas, American Astronomical Society, provided by the NASA Astophysics Data system, 1965.

[187] C. Trayner, M.H. Glowacki, A new technique for the solution of the Saha equation, J. Sci. Comp. 10 (1995) 139-149.
[188] M. R. Zaghloul, M. A. Bourham, J. M. Doster, A simple formulation and solution strategy of the Saha equation for ideal and non-ideal plasmas, J. Phys. D Appl. Phys 33 (2000) 977-984.
[189] M. R. Zaghloul, Reduced formulation and efficient algorithm for the determination of equilibrium composition and partition functions of ideal and non-ideal complex plasma mixtures, Phys. Rev. E 69 (2004) 026702.
[190] D'Ans, Lax, Taschenbuch für Chemiker und Physiker, Band 1; Physikalischchemische Daten, 4th edition, Springer-Verlag, 1992.
[191] A. B. Murphy, C. J. Arundell, Transport coefficients of argon, nitrogen, oxygen, argon-nitrogen, and argon-oxygen plasmas, Plasma chem. plasma proc. 14 (1994) 451-490.
[192] A. B. Murphy, Transport coefficients of helium and argon-helium plasmas, IEEE Transact. Plasma Sci. 25 (1997) 809-814.
[193] Bergmann, Schaefer, Band 5: Vielteilchenphysik, Walter de Gruyter Berlin, New York, 1992.
[194] Introduction to plasma physics / Robert J. Goldston and Paul H. Rutherford. Taylor and Francis, New York, 2000.
[195] J. O. Hirschfelder, C. F. Curtis, R. B. Bird, Molecular Theory of Gases And Liquids, 4th edition, John Wiley & Sons, 1967.
[196] D. Ramshaw, C. H. Chang, Ambipolar diffusion in multicomponent plasmas, Plasma Chem. Plasma Proc. 11 (1991) 395.
[197] I. I. Stewart, C. E. Hensman, J. W. Olesik, Influence of gas sampling on analyte transport within the ICP and ion sampling for ICP-MS studied using individual, isolated sample droplets, Appl. Spectrosc. 54 (2000) 164-174.
[198] J. A. Horner, G. M. Hieftje, Computerized simulation of mixed-soluteparticle vaporization in an inductively coupled plasma, Spectrochim. Acta Part B 53 (1998) 1235-1259.
[199] Y. Nojiri, K. Tanabe, H. Uchida, H. Haraguchi, K. Fuwa, J.D. Winefordner, comparison of spatial distribution of Argon species number densities with calcium atom and ion in an inductively coupled argon plasma, Spectrochim. Acta Part B 38 (1983) 61-74.
[200] N. N. Sesi, D. S. Hanselman, P. Galley, J. Horner, M. Huang, G. M. Hieftje, An imaging-based instrument for fundamental plasma studies, Spectrochim. Acta Part B 52 (1997) 83-102.
[201] M. Huang, G.M. Hieftje, Simultaneous measurement of spatially resolved electron temperatures, electron number densities and gas temperatures by laser light scattering from the ICP, Spectrochim. Acta Part B 44 (1989) 739-749.
[202] G. Gillson, G. Horlick, Comparison of atomic fluorescence and atomic emission spatial distribution profiles in the inductively coupled plasma, Spectrochim. Acta Part B 41 (1986) 1323-1346.

[203] N. N. Sesi, G. M. Hieftje, Studies into the interelement matrix effect in inductively coupled plasma spectrometry, Spectrochim. Acta Part B 51 (1996) 1601-1628.

[204] D. C. Perdian, S. J. Bajic, D. P. Baldwin, and R. S. Houk, Time-resolved Studies of Particle Effects in Laser Ablation ICP-MS Part I. Investigation of Nanosecond and Femtosecond Pulse Width Lasers and Devices for Particle Size Selection, J. Anal. Atomic Spectrom., 23 (2008) 325-335.

[205] K. Niemax, Considerations about the detection efficiency in inductively coupled plasma mass spectrometry, Spectrochim. Acta Part B 76 (2012) 65-69.

[206] A. N. Hayhurst, D. B. Kittelson, N. R. Telford, Mass spectrometric sampling of ions from atmospheric pressure flames - II: Aerodynamic disturbance of a flame by the sampling system, Combust. Flame 28 (1977) 123-135.

[207] A. N. Hayhurst, Mass spectrometric sampling of a flame, Combustion, Explosion and Shock Waves, 48 (2012) 516-525.

[208] G. K. Batchelor, Introduction to fluid dynamics, Cambridge University Press, Cambridge, 1967.

[209] L. D. Landau, E.M. Lifshitz , Fluid Mechanics (2nd Ed.), Pergamon Press, Oxford, 1987

[210] L. Flamigni, J. Koch, D. Günther, Experimental and theoretical investigations about the vaporization of laser-produced aerosols and individual particles inside inductively coupled plasmas - Implications for the extraction efficiency of ions prior to mass spectrometry. Spectrochimica Acta Part B 76 (2012) 70-76.

[211] iStar DH734, Andor, Belfast, Northern Ireland.

[212] J. Schindelin, I. Arganda-Carreras, E. Frise, V. Kaynig, M. Longair, T. Pietzsch, S. Preibisch, C. Rueden, S. Saalfeld, B. Schmid, J. Y. Tinevez, D. J. White, V. Hartenstein, K. Eliceiri, P. Tomancak, A. Cardona, Fiji: an open-source platform for biological-image analysis. Nat Meth 9 (2012) 676-682.

[213] C. A. Schneider, W. S. Rasband, K. W. Eliceiri, NIH Image to ImageJ: 25 years of image analysis. Nat Meth 9 (2012) 671-675.

[214] http://www.perkinelmer.com/Catalog/Product/ID/N8125029.